Thesis for the degree of Doctor of Philosophy

Time-domain modelling of high-frequency wheel/rail interaction

Astrid Pieringer

Department of Civil and Environmental Engineering
Division of Applied Acoustics, Vibroacoustic Group
Chalmers University of Technology
Göteborg, Sweden, 2011

Time-domain modelling of high-frequency wheel/rail interaction
Astrid Pieringer
ISBN 978-91-7385-523-5

© Astrid Pieringer, 2011

Doktorsavhandlingar vid Chalmers tekniska högskola
Ny serie nr 3204
ISSN 0346-718X

Department of Civil and Environmental Engineering
Division of Applied Acoustics, Vibroacoustic Group
Chalmers University of Technology
SE-412 96 Göteborg, Sweden
Telephone + 46 (0) 31-772 2200

Cover:
Tram in Göteborg, Sweden, during curve negotiation

Printed by
Chalmers Reproservice
Göteborg, Sweden, 2011

Time-domain modelling of high-frequency wheel/rail interaction

Astrid Pieringer
Department of Civil and Environmental Engineering
Division of Applied Acoustics, Vibroacoustic Group
Chalmers University of Technology

Abstract

The interaction between wheel and rail is the predominant source of noise emission from railway operations in a wide range of conventional speeds. On the one hand, this wheel/rail noise concerns rolling noise and impact noise caused by the vertical interaction excited by roughness and discrete irregularities of the wheel/rail running surfaces, respectively. On the other hand, it concerns squeal noise generated by the tangential interaction due to frictional instability. The aim of this thesis is to develop a model for the combined vertical and tangential wheel/rail interaction induced by roughness, discrete irregularities or frictional instability. This is the main step in the formulation of a combined prediction model for the three different types of wheel/rail noise, which can be used as a design tool for noise reduction. In order to include the non-linearities in the contact zone, the interaction model presented in this thesis is formulated in the time domain. Wheel and track models are represented by Green's functions, which leads to a computationally efficient formulation and allows the inclusion of detailed contact models. A two-dimensional (2D) vertical contact model consisting of a bedding of independent springs, and a three-dimensional (3D) vertical and tangential model based on an influence-function method for the elastic half-space, are considered. Non-Hertzian and transient effects are taken into account. In the thesis, the vertical interaction model has been applied for excitation by wheel/rail roughness and by wheel flats. In the former case, the model has been validated against existing established models. In the latter case, encouraging agreement with field measurements has been found. Results from simulations carried out with both the 2D and the 3D contact models for excitation by detailed measured roughness data indicate that significant errors may occur in the calculated contact forces, when the 3D roughness distribution is represented by the roughness on only one longitudinal line. The errors increase with a decrease in roughness correlation across the width of the contact. Frictional instabilities during curve negotiation have been investigated with the combined vertical/tangential interaction model. For both a constant friction law and a friction curve falling with the sliding velocity, stick/slip oscillations were observed. While the model is not yet considered completely reliable in the case of a falling friction curve due to the possibility of multiple solutions, the results in the case of constant friction are in good qualitative agreement with previously published findings on curve squeal.

Keywords: wheel/rail interaction, time domain, roughness, discrete irregularities, frictional instability, non-Hertzian contact, transient contact, railway noise.

List of publications

This thesis is based on an extended summary and the following appended papers, referred to by Roman numerals in the text:

Paper I
A. Pieringer, W. Kropp and J.C.O. Nielsen.
A time domain model for wheel/rail interaction aiming to include non-linear contact stiffness and tangential friction.
Proceedings of the Ninth International Workshop on Railway Noise (IWRN9), Munich, Germany, September 4-8, 2007.

Paper II
A. Pieringer and W. Kropp.
A fast time-domain model for wheel/rail interaction demonstrated for the case of impact forces caused by wheel flats.
Proceedings of Acoustics'08, Paris, France, June 29-July 4, 2008.

Paper III
A. Pieringer, W. Kropp and D.J. Thompson.
Investigation of the dynamic contact filter effect in vertical wheel/rail interaction using a 2D and a 3D non-Hertzian contact model.
Wear, 2011, doi:10.1016/j.wear.2010.10.029.

Paper IV
A. Pieringer and W. Kropp.
A time-domain model for coupled vertical and tangential wheel/rail interaction - a contribution to the modelling of curve squeal.
Proceedings of the Tenth International Workshop on Railway Noise (IWRN10), pp. 211-219, Nagahama, Japan, October 18-22, 2010.

Paper V
A. Pieringer and W. Kropp.
A numerical investigation of curve squeal in the case of constant wheel/rail friction.
To be submitted, 2011.

During the period leading to this thesis the author also has published the following papers. Due to an overlap in content with the appended papers, they are not included in the thesis.

A. Pieringer, W. Kropp and J.C.O. Nielsen.
A time domain model for wheel/rail interaction aiming to include non-linear contact stiffness and tangential friction.
In B. Schulte-Werning et al. (Eds.), *Noise and Vibration Mitigation for Rail Transportation Systems*, NNFM 99, pp. 285-291, Springer-Verlag, Berlin Heidelberg, 2008.
This paper is a short version of Paper I.

A. Pieringer, W. Kropp and D.J. Thompson. Investigation of the dynamic contact filter effect in vertical wheel/rail interaction using a 2D and a 3D non-Hertzian contact model.
Proceedings of the 8th International Conference on Contact Mechanics and Wear of Rail/Wheel Systems (CM2009), pp. 105-113, Firenze, Italy, September 15-18, 2009.
This paper is a short version of Paper III.

A. Pieringer and W. Kropp. A time-domain model for high-frequency wheel/rail interaction including tangential friction.
Proceedings of the 10th French Congress of Acoustics (CFA10), Lyon, France, April 12-16, 2010.

Acknowledgements

The work described in this thesis has been carried out during the years 2006-2011 at the Division of Applied Acoustics at Chalmers University of Technology within the project “Generation of External Noise from Trains” (VB10). The project forms part of the activities in the Centre of Excellence CHARMEC (CHAlmers Railway MEChanics). The project is partly funded by VINNOVA (the Swedish Governmental Agency for Innovation Systems) under contract no. 27465-1.

First and foremost, I would like to express my deepest gratitude to my supervisor Professor Wolfgang Kropp, who gave me both the guidance and the leeway I needed and never stopped encouraging me. Most of all, I appreciate that I could always count on you when your help was required. I would also like to thank my assistant supervisor Dr. Anders Frid from Bombardier Transportation Sweden, Västerås, for valuable advice and good discussions.

I am especially grateful to Professor Jens Nielsen for giving me access to his program DIFF and to measurement data, and for the great advice and help I received in the various areas of wheel/rail interaction. I would like to thank Peter Torstensson in the joint project TS11 for pleasant cooperation and for giving me the opportunity to take part in his measurement campaign. The contribution of the reference group members from SL Technology, Trafikverket, Bombardier Germany and Bombardier Switzerland to the project is greatly acknowledged.

During the period leading to this thesis, I spent six months within the Dynamics Group at the Institute of Sound and Vibration Research (ISVR), Southampton University. I’m very grateful to Professor David Thompson for inviting me, sharing his wide knowledge of railway noise and giving me access to measurement data. I would also like to thank Dr. Briony Croft for pleasant cooperation and good discussions and all the people at ISVR, who made my stay a very enjoyable experience.

Je tiens à remercier vivement le Dr. Virginie Delavaud et le Dr. Franck Poisson de la SNCF de m’avoir permis d’assister à leur essai en situation réelle sur la caractérisation du bruit d’impact et d’avoir partagé avec moi leurs données expérimentales.

I would like to thank all the people at Applied Acoustics contributing to the open-minded and friendly atmosphere and I am looking forward to continue working at this nice place also in future. Many thanks go to Gunilla Skog and Börje Wijk for uncomplicated and effective help in administrative and technical matters, to my colleagues for unforgettable common activities such as the annual Midsummer celebration, and to my room-mate Jonas for making daily office life during the last five years very enjoyable. Who will sing for me now?

Special thanks to Göteborgs Spårvägar for providing motivation and illustration for my work on curve squeal (almost) every day on my way from and to work.

Last but not least, tusen takk, Stig, for your invaluable support.

Contents

Chapter 1
Introduction

1.1 Background

Railways are generally considered to be a more environmentally friendly means of transportation than aircraft and road traffic. Noise is one of their few environmental drawbacks. Although exposure to noise from railways is experienced by many as less disturbing than noise from aircraft and road traffic at the same sound level [21, 58], it is still a source of considerable annoyance for residents in the vicinity of railway lines.

Railway noise is generated by diverse sources, whose relative relevance depends on the operating conditions. The importance of noise from the power unit and auxiliaries is confined to standstill, acceleration and low speeds below about $60\,\mathrm{km/h}$ [19]. For high-speed operation above approximately $300\,\mathrm{km/h}$, aerodynamic noise becomes dominant. This type of noise is generated by unsteady airflow over structural elements such as the bogies and the pantograph and by the turbulent boundary layer [24].

In the wide range of conventional speeds in between, the interaction between wheel and rail is the predominant source of noise emission. This wheel/rail noise is divided into the three categories of rolling noise, impact noise and squeal noise. While the former two are caused by the vertical wheel/rail interaction, the latter is induced by a lateral excitation mechanism [98]. Rolling noise is generated by the roughness of the wheel and rail running surfaces, which excites vibrations of track and wheel in the form of vertical relative motion. In consequence, the wheelset, the rail and the sleepers radiate noise [98]. The vehicle superstructure comprising cars and bogies does not contribute significantly to the radiation of rolling noise [24]. Impact noise is caused by discrete irregularities of the wheel and rail running surfaces such as wheel flats and rail joints. The underlying mechanism can be interpreted as an extreme form of roughness excitation [98]. Squeal noise occurring in sharp curves is generated by lateral forces due to frictional instability. While rolling noise and also impact noise are broad-band phenomena involving a large range of frequencies in the audible range, squeal noise is generally a tonal sound that dominates all other types of noise when it occurs. Summing up, it can be said

that all three types of wheel/rail noise have their origin in the contact zone between wheel and rail. The dynamic processes occurring in this area, which is generally not bigger than a one-cent coin for a steel wheel on a steel rail, are of great importance for the generation of wheel/rail noise.

Traffic operators, infrastructure administrators, train manufacturers and society in general all have an interest in the reduction of wheel/rail noise. Computer models that increase the physical understanding of the noise generation process and allow assessing possible noise reduction measures can assist in fulfilling this aim. A good example is the frequency-domain model TWINS developed for the prediction of rolling noise [97]. This model is widely used today in industry and has been applied extensively in the identification and assessment of measures to reduce rolling noise [96]. Corresponding models for the prediction of impact noise and squeal noise that would be as successful as TWINS are not yet available. One of the difficulties is that models aiming to predict these types of noise have to be formulated in the time domain and are generally computationally demanding.

1.2 Aim of the thesis

The aim of this thesis is to develop a model for the combined vertical and tangential wheel/rail interaction induced by roughness, discrete irregularities or frictional instability.

The formulation of such a wheel/rail interaction model is the main step in the development of a combined prediction model for rolling noise, impact noise and squeal noise – including the complete chain from source to receiver. The remaining step of formulating a radiation and sound propagation model is not included in the scope of this thesis.

1.3 Outline

The general structure of the thesis is as follows.

Chapter 2 provides a literature review on wheel/rail interaction models. This review serves to define the various requirements on the combined vertical and tangential wheel/rail interaction model developed in this thesis and to justify the choices made in the modelling process.

The resulting wheel/rail interaction model with all its components is elaborated in *Chapter 3*. Besides the general modelling concept, the different wheel, track and contact models used in the interaction model are introduced.

Chapter 4 covers the validation and verification of the interaction model. Partial

validation results from comparisons to existing established models and measurement data are presented.

Chapter 5 presents simulation results of the interaction model. Three specific areas of application are treated. The first two concern solely the vertical wheel/rail interaction. These are the evaluation of the contact-filter effect consisting in the suppression of short wavelength excitation by the finite size of the contact area, and the calculation of impact forces caused by wheel flats. The third application, involving both vertical and tangential wheel/rail interaction, concerns the investigation of stick/slip oscillations due to frictional instability. Simulations are carried out with a constant friction law. Additionally, the extension to a slip-velocity dependent friction law is discussed briefly.

In the appended papers, *Paper I* to *Paper V*, the wheel/rail interaction model is used with different wheel, track and contact models. The papers contain additional simulation results in the mentioned areas of application, which are not included in the summary part of the thesis. *Appendix A* provides a quick overview of the content of *Paper I* to *Paper V*.

Chapter 2

Review of the modelling of wheel/rail interaction

2.1 Modelling concepts

Wheel/rail interaction models intended for noise prediction should cover the frequency range from approximately $100\,\mathrm{Hz}$ to $5\,\mathrm{kHz}$. At frequencies below $100\,\mathrm{Hz}$ the human perception of sound is substantially reduced. Due to the contact filter effect (described in *Section 2.2*) the rolling noise spectrum decreases rapidly above $5\,\mathrm{kHz}$ [100]. As squeal is linked to the wheel being excited in one of its resonances [88], squeal may also occur at higher frequencies (see e.g. [39]). The main squeal tones are nevertheless covered by a frequency range up to $5\,\mathrm{kHz}$ [88].

Such wheel/rail interaction models are denoted high-frequency models to distinguish them from models of the classical rail-vehicle dynamics considering, for instance, running stability, curving behaviour and passenger comfort, which typically include frequencies up to $20\,\mathrm{Hz}$ [50].

The purpose of a wheel/rail interaction model is to calculate the response of the vehicle/track system to an excitation acting in the contact zone. Typical input variables are the combined roughness of wheel and rail, the shape of a discrete irregularity or, in the case of squeal, the frictional properties of the contact and parameters describing the curving behaviour of the vehicle. Typical output variables are the vibrations of vehicle and track and the contact forces acting at the interface.

In general, wheel/rail interaction models consist of three subsystems: a vehicle model, a track model and a contact model; see Figure 2.1. The vehicle and track models describe the global dynamics of the vehicle and the track. They are coupled via the contact model, which comprises the local dynamics in and close to the contact zone of wheel and rail.

The interaction of wheel and rail in the context of rolling noise and impact noise can be summarised as follows. When the wheel rolls over the rail, the roughness or the discrete irregularity (seen as a rigid indenter) causes a relative vertical displacement between wheel and rail [89]. This relative displacement is partly taken up by local deformation in the contact zone and is partly transformed into global

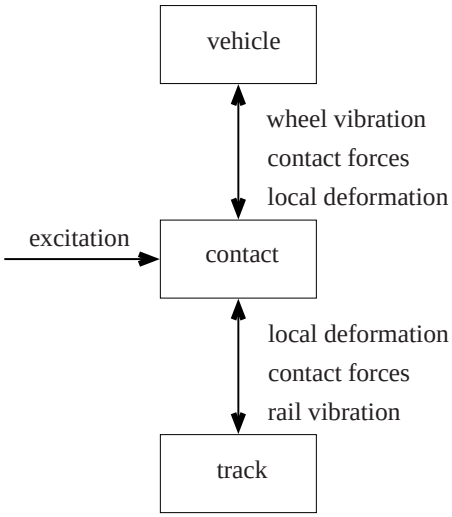

Figure 2.1: Schematic sketch of a wheel/rail interaction model.

vibrations of vehicle and track. The proportion of local deformation and global vibrations is determined by the dynamic properties of the vehicle, the track and the contact zone. The local deformation in the contact zone involves a varying contact pressure distribution, which is often represented as a point force – the vertical contact force. Tangential interaction and friction are generally neglected with regard to roughness excitation and excitation by discrete irregularities.

Curve squeal originates from friction-induced vibrations, which belong to the group of self-excited vibrations [56, 88], and thus requires the inclusion of tangential interaction in the interaction model. The phenomenon is closely linked to the curving behaviour of the railway vehicle. In tight curves, especially the leading wheelset in a bogie rolls with a high angle of attack against the rail. In consequence, a relatively large lateral sliding motion occurs between wheel and rail, which gives rise to a friction force [88]. This lateral motion can serve as energy source for self-excited vibrations involving stick/slip oscillations in the wheel/rail contact and global vibrations of the wheel in one of its resonances. Through the coupling in the wheel/rail contact, the rail is also excited to vibrations.

Wheel/rail interaction models can be formulated either in the frequency or in the time domain. By their nature, frequency-domain models are completely linear models, while time-domain models are suitable to include all kinds of non-linearities. With regard to curve squeal, frequency-domain models can only predict which wheel modes are prone to squeal, but models aiming to predict squeal amplitudes have to be formulated in the time domain. A disadvantage of time-domain models is that they are generally more computationally demanding than are frequency-domain models.

Frequency-domain models work with frequency response functions such as receptances or impedances that represent the dynamic behaviour of the vehicle, the track and the contact zone. In the context of roughness excitation, it is implicitly assumed that a roughness component of wavelength λ, which is passed by the wheel at train speed v, excites the wheel/rail system at the frequency

$$f = \frac{v}{\lambda} \tag{2.1}$$

and causes vibrations only at this frequency f.

A considerable number of frequency-domain models for wheel/rail interaction induced by roughness excitation is available in the literature, e.g. [26, 34, 67, 76–79, 86, 89–93], and a good overview of these models is given in the review article of Knothe and Grassie [50]. Frequency-domain models for curve squeal allowing for stability analysis have e.g. been developed by Maria Heckl [32] and de Beer [16].

The most well-known frequency-domain model for the calculation of rolling noise is a model going back to Remington [76–79], which has been generalised and further improved by Thompson [89–93]. His formulation is implemented in the software package TWINS [100] which is widely used in industry today. Two basic equations of Thompson's model, which are repeated here for vertical coupling between the wheel and the rail only, illustrate well the functioning of wheel/rail interaction models in the frequency domain:

$$\Xi_{\mathrm{W}} = \frac{-G_{\mathrm{W}} R}{G_{\mathrm{W}} + G_{\mathrm{R}} + G_{\mathrm{C}}} \tag{2.2}$$

$$\Xi_{\mathrm{R}} = \frac{G_{\mathrm{R}} R}{G_{\mathrm{W}} + G_{\mathrm{R}} + G_{\mathrm{C}}} \,. \tag{2.3}$$

The vibration amplitude of the wheel, Ξ_{W}, and of the rail, Ξ_{R}, at a certain frequency due to a roughness component with amplitude R, is determined by the receptances of the wheel, G_{W}, the rail, G_{R} , and the contact zone, G_{C}.

The range of validity of the assumption of linearity that is necessary in frequency-domain models has been investigated by Wu and Thompson [108] using a time-domain model for roughness excitation. They found that non-linearities in the contact model cannot be neglected in the cases of severe roughness and/or a low static contact preload, which can cause loss of contact between wheel and rail. These results have been confirmed by Nordborg, who used both a frequency-domain model and a time-domain model based on Green's functions to study non-linear effects in the vertical interaction [67]. If the response to discrete irregularities such as wheel flats and rail joints is to be calculated, time-domain models are the only option. Only they can capture the discrete nature of the phenomena and model the loss of contact that is likely to occur [109, 110]. As curve squeal is an intrinsically

non-linear and transient phenomenon, time-domain models are also here the only option, if the magnitude of squeal is to be predicted.

Time-domain models essentially solve the system of differential and algebraic equations describing vehicle, track and contact by a time-stepping procedure. Due to the required computational effort of time-domain solutions, it is usually necessary to simplify wheel, rail and contact dynamics. A common approach is to use rigid wheel models in the context of vertical wheel/rail interaction [50]. In time-domain models for curve squeal, the influence of the track is often completely disregarded. Among the few time-domain squeal models including track dynamics are the models by Fingberg [22], Périard [71] and Huang et al. [37]. In order to include detailed submodels in time-domain models, reduction techniques have to be applied. A common approach is to model the track or the wheel as a modal component derived from a finite-element model [50]. An alternative, more computationally efficient approach has been demonstrated by Wu and Thompson [109]. They modelled the dynamics of the track using a single differential equation obtained from a transfer function $H(s)$,

$$H(s) = \frac{b_1 s^3 + b_2 s^2 + b_3 s + b_4}{s^4 + a_1 s^3 + a_2 s^2 + a_3 s + a_4}\,, \tag{2.4}$$

whose constant coefficients a_i and b_i were adapted in such a way that the differences between $H(\mathrm{i}\omega)$ and the point receptance of the track were minimised. Their technique is, however, not suitable to include track models with discrete supports. A third, very promising, approach that is computationally efficient and allows including discrete supports is the representation of the track by moving Green's functions that describe the dynamic behaviour of the track in a moving contact point. This technique, going back to Manfred Heckl's proposal for a railway simulation program [31], has e.g. been used by Nordborg [67] and recently by Mazilu [57]. As a matter of course, the wheel can also be represented by Green's functions. This approach has been chosen by Maria Heckl et al. [33] who formulated a squeal model for the wheel represented as an annular disc.

2.2 Excitation by roughness

It is now generally accepted that the roughness of wheel and rail running surfaces is the predominant cause of the occurrence of rolling noise [98]. Applying Equation (2.1) for the frequency range of interest from $100\,\mathrm{Hz}$ to $5\,\mathrm{kHz}$ and train speeds ranging from 50 to $300\,\mathrm{km/h}$ leads to a relevant roughness-wavelength interval from 830 to $3\,\mathrm{mm}$. Thompson [94] estimates that the wavelength range $300 - 10\,\mathrm{mm}$ is the most important. Typical roughness amplitudes are in the range

$0.1 - 30\,\mu\mathrm{m}$. For severely corrugated rail, even higher amplitudes occur [94].

Wheel and rail make contact not only in a point, but in a small area denoted a contact patch. The roughness distribution throughout this contact patch is responsible for the excitation of vibrations. Nevertheless, most available wheel/rail interaction models – including all models mentioned in *Section 2.1* except Heckl's proposal [31] – assume that the roughness distribution effectively acts in one point. This implicitly includes the assumption that the contact-patch size and shape are not influenced by the roughness.

The finite size of the contact patch is responsible for two important effects concerning the excitation of the wheel/rail system by roughness [94]:

1. Roughness components of wavelengths that are in the order of, or shorter than, the length of the contact zone in the rolling direction do not excite the system as effectively as roughness components of longer wavelengths, an effect known as the contact-filter effect.

2. The excitation of the wheel/rail system depends also on the variations in roughness profile height across the width of the contact in lateral direction. The excitation is greatest when the roughness is strongly correlated across the contact patch, and progressively decreases as the roughness becomes uncorrelated.

Models which assume that the roughness distribution effectively acts in one point have to account for these two effects by roughness pre-processing. In frequency-domain models, this is done by adding a correction – the contact filter – to the roughness spectrum (in dB). Remington [78] proposed an analytical model of such a contact filter for circular contact patches of radius a

$$|H(k)|^2 = \frac{4}{\alpha}\frac{1}{[ka]^2}\int_0^{tan^{-1}\alpha} [J_1(ka\,\sec\chi)]^2\,\mathrm{d}\chi\,, \tag{2.5}$$

which gives the correction $|H(k)|$ as a function of the roughness wavenumber $k = 2\pi/\lambda$, λ being the wavelength. The function J_1 is the Bessel function of order 1 and the parameter α is a measure of the degree of correlation between roughness across the width of the contact, where a small value of α implies a high degree of correlation.

More recently, Remington and Webb [75] presented a contact model based on a three-dimensional bedding of independent springs, which allows considering the actual roughness distribution in the contact patch and thereby includes effects 1 and 2 above in a natural manner. They called their model a three-dimensional 'distributed point reacting spring' (3D-DPRS) model. Thompson [95] applied this model to calculate numerical frequency-domain contact filters from roughness data

measured in several parallel lines. He concluded that the analytical contact filter of Equation (2.5) gives an attenuation that is too large at short wavelengths, but gives reasonable results for wavelengths down to somewhat smaller than the contact-patch length if the right value of α is chosen. The discrepancies at short wavelengths are attributed to the fact that the 3D-DPRS model, in contrast to the analytical model, takes account of the variation of the normal load across the contact patch. As in many practical cases, only one line of roughness is measured, Ford and Thompson [23] developed a two-dimensional version of the DPRS model which they found to perform surprisingly well in comparison to the 3D-DPRS model. The 2D-DPRS model, however, cannot consider correlation effects across the contact width, which explains differences of a few dB between both models at wavelengths as short as the contact patch length or shorter.

To include the contact-filter effect in time-domain models, one possibility is to calculate an equivalent roughness as a pre-processing step, which represents the roughness distribution experienced by the system for each wheel position on the rail. The 2D-DPRS model [23] (or even the 3D-DPRS model if the required roughness data are available) can be applied for this task. A simpler but less accurate means to obtain an equivalent roughness is to calculate an average of the roughness over the nominal contact patch length (which is the length in the absence of roughness) [23]. Another possibility making unnecessary the mentioned roughness pre-processing is to directly consider the finite size of the contact patch at each time step in a wheel/rail interaction model, by using an appropriate contact model. Ford and Thompson implemented the 2D-DPRS model as a contact model in a time-domain model and presented some preliminary results [23].

2.3 Excitation by discrete irregularities

The most common discrete irregularities that are responsible for the occurrence of impact noise are wheel flats and rail joints. A wheel flat is a defect of the running surface of a railway wheel that occurs when the wheel locks and slides along the rail because of malfunction in the brakes or lack of wheel/rail adhesion. The sliding causes severe wear, leading to the wheel being flattened on one side [38]. At a rail joint, the rail running surface shows a severe discontinuity characterised by a gap and a height difference between the two sides of the gap. Moreover, the rail often dips close to a joint [110].

In wheel/rail interaction models, discrete irregularities are generally introduced as a form of extreme roughness described by simple analytic functions. Newton and Clark [60] used for instance the following shape, $f(x)$, to represent a rounded

wheel flat:

$$f(x) = \frac{d}{2}\left[1 - \cos 2\pi \frac{x}{l}\right]; \quad d = \frac{l^2}{16r}, \tag{2.6}$$

where x is the distance along the flat, d the maximum depth of the wheel flat, l its length, and r the wheel radius. Similar descriptions of wheel flats have been used, amongst others, by Nielsen and Igeland [64], Mazilu [57] and Baeza et al. [5]. Wu and Thompson [110] proposed quadratic functions to describe the dipped rail at a joint.

In a similar manner as for roughness excitation, models with one effective contact point have to take into account how the wheel/rail system effectively "sees" the discrete irregularity. Due to its finite curvature, the wheel does not follow the irregularity shape as described, for example, by Equation (2.6). Wu and Thompson included this effect by calculating equivalent irregularity shapes for wheel flats [109] and rail joints [110]. Baeza et al. used the same equivalent irregularity shape for wheel flats [5]. Additionally, they included the changes in stiffness due to the wheel flat geometry by pre-calculating stiffness functions for each angular position of the wheel flat with a three-dimensional contact model. An alternative way to account for the changes in the contact zone and the finite curvature of the wheel would again be to incorporate an appropriate contact model that is evaluated at each step in a time-domain model, though this seems not to have been done yet.

2.4 Friction-induced vibrations

The ‘pure’ rolling motion between wheel and rail is accompanied by small relative motions between the bodies. The relative velocities normalised with the rolling velocity are denoted ‘creepages’ [88]. These creepages consist of a low-frequency part determined by the vehicle dynamics and a high-frequency part caused by the global dynamics of wheel and track. Since wheel and rail are assumed to be rigid in classical vehicle dynamics, the low-frequency part of the creepage corresponds to the rigid body velocities in the nominal contact point. The high-frequency part considers in addition the global vibrations of the wheel and track modelled in the wheel and track models, but does not include the local deformation in the contact zone.

The creepages in three degrees of freedom in the contact plane are to be considered: the longitudinal creepage, the lateral creepage and the spin creepage. The longitudinal creepage ξ is defined as the relative velocity Δv_1 between wheel and rail in the rolling direction normalised with the rolling velocity v. The lateral creepage η is defined similarly as the normalised relative velocity Δv_2 in the transverse lateral direction. Lastly, the spin creepage ϕ is the normalised relative angular velocity $\Delta\omega_3$ about an axis normal to the contact plane [20]. The corresponding formulas

are given as:

$$\xi = \frac{\Delta v_1}{v} \tag{2.7}$$

$$\eta = \frac{\Delta v_2}{v} \tag{2.8}$$

$$\phi = \frac{\Delta \omega_3}{v}\,. \tag{2.9}$$

Originally, three different relative motions between wheel and rail occurring in tight curves have been discussed as relevant causes for curve squeal [81, 85, 88]: (1) longitudinal creepage due to differential slip, (2) flange rubbing between the wheel flange and the gauge face of the rail, and (3) lateral creepage of the wheel tyre on the top of the rail. All three phenomena are closely linked to the curving behaviour of the vehicle; see e.g. [88]. Longitudinal creepage occurs since the outer wheel on a wheelset has a longer running distance through the curve than the inner wheel and the conicity of the wheels can only partly compensate for this difference in running distance in tight curves. Furthermore, in tight curves, the outer wheel of the leading wheelset in a bogie (and possibly the inner trailing wheel) will run into flange contact. Finally, especially the leading wheelset in a bogie rolls with a high angle of attack against the rail in tight curves, which gives rise to a large lateral creepage. In 1976, Rudd [81] discarded longitudinal creepage and flange rubbing as relevant causes for curve squeal, mainly based on the observations that the elimination of longitudinal creepage (by independently driven wheels) and the absence of flange rubbing (the situation at the inner leading wheel) do not prevent squeal. He thus concluded – in accordance with an earlier paper by Stappenbeck [85] – that curve squeal arises from stick/slip behaviour due to lateral creepage of the wheel tyre on the top of the rail. This view is nowadays widely accepted.

Flange rubbing is nevertheless considered to be the origin of another type of noise denoted ‘flanging noise’, which generally occurs at much higher frequencies and may have a much more broad-band character than the tonal squeal noise [88]. This type of noise is not further considered here.

The actual mechanism of the instability leading to curve squeal is still a controversial topic. Rudd [81] introduced the negative slope of the friction characteristic (i.e. decreasing friction for increasing sliding velocity) as the source of the instability, and most subsequent models have adopted this approach [8, 12, 16, 22, 32, 33, 71, 111]. As friction is difficult to measure, it is inevitable to make assumptions about the exact shape of the friction characteristic. Correspondingly, many different friction curves have been used in the literature.

From a mathematical point of view, the instability can also be explained by the coupling between normal and tangential dynamics, leading to the non-symmetry of the system’s stiffness matrix [68]. This mechanism is exemplified by Hoffmann

et al. [36] with a model having two degrees of freedom. Glocker et al. [25] recently presented a curve squeal model that shows stick/slip oscillations in the case of a constant friction coefficient. They identified one axial mode with zero nodal circles and two radial modes of the wheel, which occur at similar frequencies, as essential for the squeal mechanism. Simulation results showing stick/slip in the case of constant friction have also been reported by Ben Othman [6] and Brunel et al. [8]. Some experimental evidence that squeal occurs in the case of constant friction has been presented by Koch et al. [51].

2.5 Vehicle and track models

Vehicle models in vertical high-frequency wheel/rail interaction models are generally simple. As the vehicle's primary and secondary suspensions isolate the bogie and car body from the wheelset at frequencies of more than a few Hertz, the vehicle's dynamic behaviour in the interaction model is sufficiently described by the dynamics of the wheelset [50]. Knothe and Grassie [50] state that the vehicle's unsprung mass (including wheelset, bearings and axle-mounted components) is even satisfactorily represented as a rigid body for vertical interaction. If, however, lateral wheel/rail interaction is to be considered, more advanced wheel models are required, which include the wheel's flexibility [50].

In contrast to the situation for the wheel, sophisticated models are necessary to represent the track's dynamic behaviour in the frequency range of interest up to $5\,\mathrm{kHz}$, also in vertical wheel/rail interaction. Available track models are distinguished by their representation of the rail and the supports.

Historically, the rail has often been modelled as an Euler-Bernoulli beam, neglecting shear deformation and rotational inertia. Such simple beam models can only represent the track's vertical dynamics up to about $500\,\mathrm{Hz}$ [50]. Using a Timoshenko beam model for the rail, which includes rotational inertia and shear deformation, the frequency range of validity of the track model can be extended, the upper limit frequency being a subject of discussion. Knothe and Grassie [50] estimate that the rail can be modelled as a single Timoshenko beam up to $2.5\,\mathrm{kHz}$ if only vertical vibrations are of interest. Wu and Thompson [108] state that such models are adequate up to about $5\,\mathrm{kHz}$ since the occurring cross-sectional deformations of the rail (not modelled by Timoshenko-beam models) are not important in terms of the vertical wheel/rail interaction in this frequency range (see also [100, 103]). A Timoshenko beam model of the rail is for instance implemented in the wheel/rail interaction model DIFF developed by Nielsen and Igeland [64]. In order to include the cross-sectional deformations that become significant above about $1.5\,\mathrm{kHz}$ [91], different types of rail models are required. One example is the multi-layer model

by Scholl [82], who represented rail head, web and foot by three infinitely long, homogeneous layers with different densities and Young's moduli. Vibrational shapes with cross-sectional deformation can at least in principle be modelled by this approach. A second example is the model by Thompson [91] who used a detailed finite-element mesh for a short length of the rail, which he extended to infinity using periodic structure theory. Gry [30] presented a third alternative model based on a description of waves travelling through the rail.

Concerning the supports, models with a continuous support of the rail and models with discrete supports are distinguished. Nordborg found that the inclusion of discrete supports is important for lower frequencies around the sleeper-passing frequency and for higher frequencies around the pinned-pinned resonance frequency of the rail [67]. The sleeper-passing frequency, $f_{\mathrm{S}} = v/L_{\mathrm{S}}$, is the frequency at which the wheelset passes the sleepers, v being the train speed and L_{S} the sleeper spacing. At the pinned-pinned frequency, f_{p}, which typically lies around $1\,\mathrm{kHz}$, the bending wavelength of the rail corresponds to the length of two sleeper spans, $\lambda_{\mathrm{p}} = 2L_{\mathrm{S}}$, with nodes located at the sleeper positions. Knothe and Grassie [50] give an overview of different ways to model supports comprising railpads, sleepers, ballast and substrate.

2.6 Hertzian model for normal contact

The normal[1] contact model applied in most of the available interaction models is the Hertzian contact model; see e.g. the models [12, 57, 64, 67, 71, 78, 97, 108]. This standard model goes back to Heinrich Hertz who published his theory "On the contact of elastic solids" already in 1882 [35]. A comprehensive description of the Hertzian contact theory can e.g. be found in [41] or [55]. In this section, only a short outline of the theory is given and the connection to the railway case is established, which provides a basis for the discussion of non-Hertzian models in *Section 2.7*.

The Hertzian theory of normal contact between two bodies relies on the following assumptions [41]

1. *Linear elasticity*
   The bodies are perfectly linear elastic solids.

2. *Half-space assumption*
   The surfaces of the bodies are non-conforming surfaces, i.e. they first make contact at a point (or along a line). Even under load, the dimensions of the

[1] The denotation 'normal' is here used in the sense 'in the direction normal to the surfaces of rail and wheel'. As the difference between the normal and the vertical direction is negligible in the case of tread contact, 'normal' and 'vertical' are used as synonyms throughout this thesis.

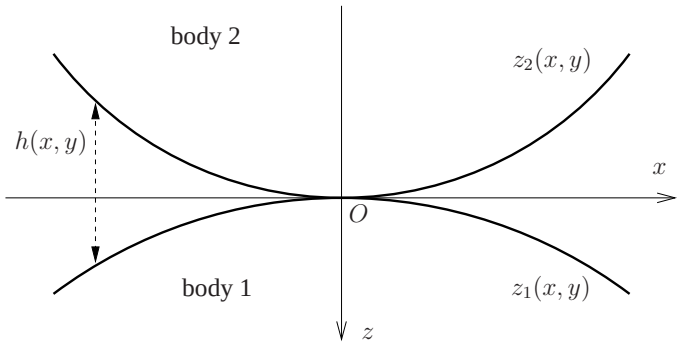

Figure 2.2: Two non-conforming surfaces touching at the point O.

contact area are small in comparison to the dimensions of the bodies and the radii of curvature of the surfaces. This implies that the bodies can be considered as a semi-infinite elastic solid with a plane surface (an elastic half-space) for the purpose of stress and deformation calculations.

3. *Smoothness*
   The surfaces are perfectly smooth.

4. *Hertzian surfaces*
   The surfaces can be described by quadratic functions in the vicinity of the contact area (see below).

5. *Absence of friction*
   No friction occurs in the contact area. Only normal pressure is transmitted.

Under these assumptions, the contact area is an ellipse and the normal pressure distribution is ellipsoidal. The case of contact over a long strip as it occurs for two cylindrical bodies with their axes lying parallel is a limit case of elliptical contact. This case has to be treated separately and is not further considered here. The following presentation of the relevant formulas for contact dimensions, loads and deformations in elliptical contact mainly follows the presentation by Lundberg and Sjövall [55].

Assume that two non-conforming surfaces as seen in Figure 2.2 are brought into contact without loading. They only touch in one point that is taken as origin O of a Cartesian coordinate system xyz. The xy-plane is the tangent plane to the surfaces at the origin, and the z-axis is the common normal to the two surfaces pointing into body 1. Under assumption 4, the surfaces of bodies 1 and 2 in the vicinity of the

contact point are then described by

$$z_1(x_1, y_1) = \frac{x_1^2}{2r_{x_1}} + \frac{y_1^2}{2r_{y_1}} \tag{2.10}$$

$$z_2(x_2, y_2) = -\left(\frac{x_2^2}{2r_{x_2}} + \frac{y_2^2}{2r_{y_2}}\right), \tag{2.11}$$

where r_{x_1} and r_{y_1} are the principal radii of curvature of surface 1 at the origin, i.e. the minimum and maximum values of the radius of curvature of all possible cross-sections of the profile, which are found in perpendicular planes denoted the x_1z- and the y_1z-planes). The variables r_{x_2} and r_{y_2} are the principal radii of curvature of surface 2 at the origin, found in the x_2z- and y_2z-planes. Each radius of curvature is positive if the curvature centre is located inside the body (convex surface) and negative if the curvature centre is located outside (concave surface). The x_1z- and x_2z-planes enclose an angle ψ.

In the railway case, the wheel rolling radius, r_{x_2}, and the rail transverse radius of

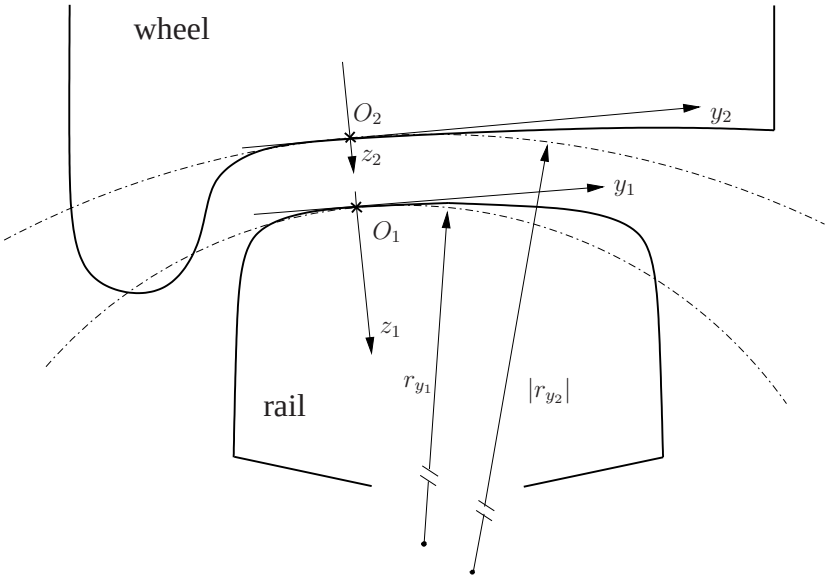

Figure 2.3: Transverse radius of curvature of the rail, r_{y_1}, and the wheel, r_{y_2}, for contact occurring at O_1-O_2.

curvature, r_{y_1}, are generally positive, while the wheel transverse radius of curvature, r_{y_2}, can be positive or negative [4]. The rail radius in the rolling direction, r_{x_1}, is assumed infinite. The wheel and rail radii of curvature are determined at the geometric point of contact, which is the point $O = O_1 = O_2$ in Figure 2.3. The geometric point of contact depends on the wheel and rail profiles and the translatory and angular position of the wheel on the rail and is calculated for wheel and rail considered as rigid.

Considering Equations (2.10) and (2.11), the distance of the undeformed surfaces can be expressed by

$$h(x,y) = \frac{x^2}{2r_x} + \frac{y^2}{2r_y}\,, \tag{2.12}$$

with suitable orientation of the x- and y-axes. The variables r_x and r_y denote the principal *relative* radii of curvature of the surfaces, which can be calculated from the principal radii of curvature of both surfaces, $r_{x_1}, r_{y_1}, r_{x_2}, r_{y_2}$, and the angle ψ [55].

When the two bodies are pressed together with a load P, they deform locally and the contact point develops into a contact ellipse with semi-axes a and b, where by definition $a > b$. Distant points in the two bodies approach by a distance δ. The ratio of the semi-axes of the contact ellipse, $A = a/b$, depends only on the relative principal radii of curvature, r_x and r_y.

The final equations for the semi-axes, a and b, and the approach of distant points, δ, read

$$a = \hat{a}\left[\frac{P}{E^*}\right]^{\frac{1}{3}} \tag{2.13}$$

$$b = \hat{b}\left[\frac{P}{E^*}\right]^{\frac{1}{3}} = \frac{a}{A} \tag{2.14}$$

$$\delta = \hat{\delta}\left[\frac{P}{E^*}\right]^{\frac{2}{3}}, \tag{2.15}$$

where $\hat{a}$, $\hat{b}$ and $\hat{\delta}$ are calculated from elliptical integrals and depend only on the relative principal radii of curvature, r_x and r_y; see [55]. The variable E^* denotes an equivalent Young's modulus calculated from the Young's modulus, E_i, and Poisson's ratio, ν_i, $i = 1, 2$, of both bodies

$$\frac{1}{E^*} = \frac{1}{2}\left[\frac{1-\nu_1^2}{E_1} + \frac{1-\nu_2^2}{E_2}\right]. \tag{2.16}$$

The maximum contact pressure,

$$p_0 = \frac{3P}{2\pi ab}\,, \tag{2.17}$$

occurs at the origin, and the pressure distribution in the contact area is ellipsoidal

$$p = p_0\sqrt{1 - \left[\frac{x}{a}\right]^2 - \left[\frac{y}{b}\right]^2}\,. \tag{2.18}$$

To get an impression of the magnitudes of the variables involved, consider the case of a steel wheel and a steel rail both modelled as cylinders with radius $r_{y_1} = 0.3\,\mathrm{m}$

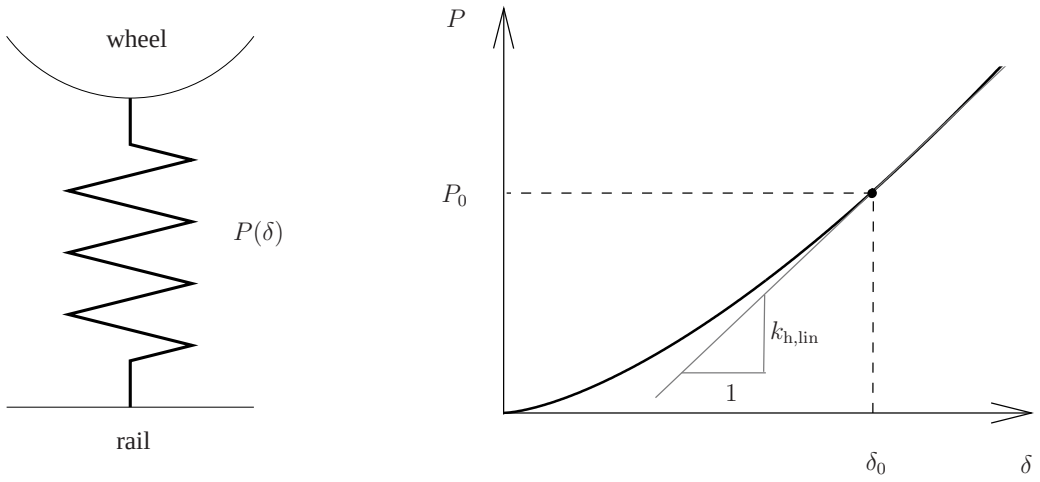

(a) Hertzian spring.

(b) Linearisation of the non-linear spring characteristic.

Figure 2.4: Implementation of the Hertzian contact model into a wheel/rail interaction model.

for the rail and $r_{x_2} = 0.46\,\mathrm{m}$ for the wheel. Under a preload $P = 65\,\mathrm{kN}$, the contact ellipse has the semi-axes $a = 6.2\,\mathrm{mm}$ and $b = 4.7\,\mathrm{mm}$, distant points in wheel and rail approach by $\delta = 78\,\mu\mathrm{m}$ and the maximum contact pressure reaches $p_0 = 1.1\,\mathrm{GN/m^2}$.

In many interaction models operating in the time domain, a single non-linear spring is introduced as contact model between wheel and rail (see Figure 2.4(a)). The characteristic, $P(\delta)$, of this spring is obtained from Equation (2.15)

$$P = \left[E^* \hat{\delta}^{\frac{2}{3}}\right] \delta^{\frac{3}{2}} = C_h \, \delta^{\frac{3}{2}} \,. \tag{2.19}$$

The factor C_h is a function only of the principal relative radii of curvature and the material parameters.

Frequently, Equation (2.19) is further simplified. The characteristic is linearised around the approach of distant points, δ_0, corresponding to static preload, P_0, as demonstrated in Figure 2.4(b). The stiffness of the linear Hertzian spring, $k_{\mathrm{h,lin}}$, is obtained from the tangential gradient in the point (δ_0, P_0)

$$k_{\mathrm{h,lin}} = \left.\frac{\mathrm{d}P}{\mathrm{d}\delta}\right|_{\delta_0} = \frac{3}{2} C_h \delta_0^{\frac{1}{2}} = \frac{3}{2}\frac{P_0}{\delta_0} \,. \tag{2.20}$$

In frequency-domain models this linearisation has to be carried out.

2.7 Non-Hertzian models for normal contact

Under the assumptions listed in the previous section, the Hertzian theory gives the exact solution of the normal contact problem. But real wheel and rail surfaces never meet these assumptions exactly and, in consequence, the Hertzian solution can only be an approximate one. In many situations, the Hertzian contact theory might still be sufficient, but it is important to be aware of its limitations. The intention of this section is to discuss the adequacy of the Hertzian contact theory for the wheel/rail contact on the basis of a literature review and to present available non-Hertzian contact models. The focus is hereby on non-Hertzian geometry. The influence of friction and plasticity is not investigated.

Several phenomena lead to deviations from the Hertzian geometry in wheel/rail contact.

The Hertzian contact theory relies on constant radii of curvature of the (undeformed) bodies in the contact area. The radii of curvature of wheel and rail profiles may however change quickly or even jump in lateral direction. Jumps in radius of curvature occur for example for the standard rail profile UIC60, which consists of a sequence of circular arcs with the radii of $300\,\mathrm{mm}$, $80\,\mathrm{mm}$ and $13\,\mathrm{mm}$ [112]. Quick changes in radius of curvature are especially pronounced for worn profiles. As a result of vehicle dynamics, the lateral contact position of the wheel on the rail varies during operation and the changes in radii of curvature in the contact area lead to the formation of non-elliptical contact patches and pressure distributions differing significantly from the Hertzian distribution [48, 107, 112]. Even greater deviations from the Hertzian geometry occur for a wheel flat. In the flat area the radii of curvature of the wheel change quickly and the wheel surface cannot be described by quadratic functions. Baeza et al. [5] compared the impact forces caused by a wheel flat calculated with the Hertzian model and a non-Hertzian model based on influence functions for the elastic half-space and found that the Hertzian model tends to overestimate the peak impact force.

Another important assumption in Hertzian contact theory is that the contacting bodies can be locally approximated by elastic half-spaces for the purpose of contact-stress and deformation calculations. This assumption is valid when the bodies are non-conformal implying that the dimensions of the contact area are small in comparison to the characteristic dimensions of the contacting bodies, e.g. the diameter and the radii of curvature. The half-space assumption is reasonable for wheel/rail tread contact (Figure 2.5(a)), but it is violated for flange contact and contact near the gauge corner of the rail (Figure 2.5(b)) [49]. In the latter case, the flange thickness and the radius of curvature at the gauge corner are of the same order of magnitude as the contact length and the contact is conformal. But this does not necessarily mean that the Hertzian model is a bad choice for all practical cases, where the half-space assumption is obviously not fulfilled. Yan and Fischer [112]

found surprisingly good agreement between the Hertzian pressure distribution and the distribution obtained with a finite-element program for one case of rail gauge corner contact between the rail UIC60 and the wheel UICORE. The work of Wu and Wang [107] indicates, however, that the situation changes when in addition to the violation of the half-space assumption, the radii of curvature of one of the two bodies jump in the contact area. They report errors in maximum contact stress and contact area of up to 72% when comparing the Hertzian solution with the solution obtained with a program for conformal contact.

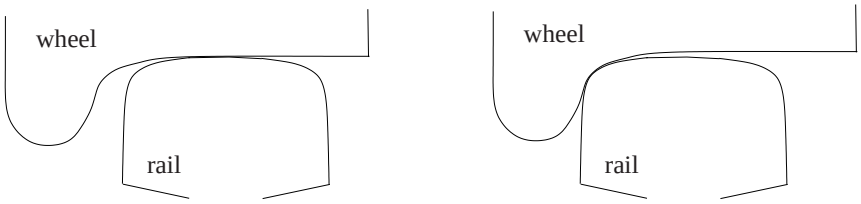

(a) Tread contact. (b) Flange/gauge corner contact.

Figure 2.5: Wheel/rail contact situations.

Additionally, the standard Hertzian contact theory is limited to one single contact patch, but the development of two- or multi-point contact is a common phenomenon in wheel/rail interaction. A typical example is the two-point contact for guiding wheels in curves with one contact patch on the wheel tread and one on the wheel flange. Multiple contact patches also occur frequently at other locations on the wheel profile [73].

A fourth phenomenon leading to deviations from the Hertzian geometry is the occurrence of surface roughness. Roughness is not only a source of excitation, but it also changes the geometry of the contacting surfaces and thereby the stiffness of the contact and the size and shape of the contact area. This effect is not included in the Hertzian contact model, which assumes smooth wheel and rail surfaces. In reality, contact does not occur continuously over the whole nominal area of contact, but at many discrete locations, where asperities of the rough surfaces make contact. All the discrete contact locations together form the real area of contact, which is only a fraction of the nominal area of contact. Accordingly, the real contact pressure also differs from the predictions by the Hertzian model. Locally, it is several times higher than the maximum Hertzian pressure [49].

In order to solve the three-dimensional contact problem for arbitrary non-Hertzian geometries, the continuum equations of elasticity have to be solved (see e.g. Appendix A in [43]). This is, in the most general case, only possible numerically, e.g. by using finite-element methods.

If the contacting bodies are subject to certain regularity conditions, the constitutive

relations can be brought into a surface mechanical form [43]:

$$\begin{aligned} \mathbf{u}(\mathbf{x}) &= \int_{\partial V} \mathbf{A}(\mathbf{x},\mathbf{x}^*)\,\mathbf{p}(\mathbf{x}^*)\,\mathrm{d}S \\ u_i(\mathbf{x}) &= \int_{\partial V} \sum_{j=1}^{3} A_{ij}(\mathbf{x},\mathbf{x}^*)\,p_j(\mathbf{x}^*)\,\mathrm{d}S\,, \quad i=1,2,3\,. \end{aligned} \tag{2.21}$$

The displacement $\mathbf{u}$ at a point $\mathbf{x}$ in the body is obtained by integrating over the surface tractions $\mathbf{p}$ on the surface S of the body. The functions $\mathbf{A}(\mathbf{x},\mathbf{x}^*)$, which are called influence functions, indicate the displacement $\mathbf{u}$ at $\mathbf{x}$ due to a point load at surface point $\mathbf{x}^*$. The elastic half-space is one of the few geometries in three-dimensional elasticity for which the influence functions are explicitly known. In the general case they can only be evaluated numerically. This is the reason why the half-space assumption considerably simplifies the solution of the three-dimensional contact problem. The influence functions for the elastic half-space have been derived by Boussinesq [7] and Cerruti [11] and may also be found in [43]. Equations (2.21) with $\mathbf{A}(\mathbf{x},\mathbf{x}^*)$ specified for the elastic half-space are called the Boussinesq-Cerruti integral equations. If the normal elastic displacement, u_3, is assumed not to be influenced by the tangential tractions, p_1 and p_2, the Boussinesq-Cerruti integral equation for the normal displacement, $u_3^{[k]}$, of body k, $k=1,2$, at the surface point $\mathbf{x}=[x_1,x_2,0]^{\mathrm{T}}$ simplifies to

$$u_3^{[k]}(x_1,x_2) = \frac{1-[\nu^{[k]}]^2}{\pi E^{[k]}} \int_{A_c} \frac{p_3(x_1^*,x_2^*)}{\sqrt{[x_1-x_1^*]^2+[x_2-x_2^*]^2}}\,\mathrm{d}x_1^*\mathrm{d}x_2^*\,, \quad k=1,2\,, \tag{2.22}$$

where A_c is the contact area and the normal surface traction, p_3, vanishes outside the contact area. The former assumption implies that the contacting bodies are quasi-identical, which is satisfied e.g. when the two bodies are made of the same material or when both are incompressible. The complete definition of quasi-identity may be found in [43]. As railway wheel and rail are both made of steel, quasi-identity is satisfied in wheel/rail contact.

Many of the contact models published in the 1970s and 1980s for non-Hertzian geometry are a special type of boundary-element approach based on the Boussinesq-Cerruti expressions for the elastic half-space. Only some examples are cited here:

Kalker's programme CONTACT [43, 44], which he developed in the years 1983-1990, is the most successful of these models and is still widely used today. Kalker uses a variational method based on the principle of maximum complementary energy and applies an effective active-set method to solve the contact problem. He discretises the potential contact area with rectangular elements in which the surface traction is constant. Kalker himself calls his method 'exact' [43], which is meant in the sense that the exact Boussinesq-Cerruti equations are implemented [53]. But of

course the method is still subjected to numerical errors and the errors introduced by the half-space assumption. The main advantages and disadvantages of CONTACT are described in the state-of-the-art article about rail (and road) contact mechanics by Knothe et al. [49]. On the one hand, CONTACT is very versatile. It deals with the normal and the tangential problem in rolling contact for arbitrary geometries - as long as the half-space assumption is valid, it handles materials that are not quasi-identical, and provides steady-state and transient solutions. On the other hand, the calculation times are generally considered too high for the implementation into on-line simulations of vehicle system dynamics.

Another contact model was presented by Le-The [53] in 1987. He assumes quasi-identity of the contacting surfaces and starts directly from equation (2.22) to solve the normal contact problem. An additional assumption made by Le-The is that the contacting bodies are bodies of revolution with almost parallel axes, which is approximately true in wheel/rail contact. In this case, the contact area and the normal pressure distribution are almost symmetrical with respect to an axis, y, perpendicular to the rolling direction, x. The contact area can then be discretised in strips in the x-direction that are assigned an elliptical pressure distribution in the rolling direction

$$p_k(x,y) = \hat{p}_k \sqrt{1 - x^2/x_{rk}^2}\,, \tag{2.23}$$

where $\hat{p}_k$ is the maximum pressure amplitude in strip k and x_{rk} is half of the strip length. The pressure in y-direction is assumed constant in each strip. This type of contact elements, which is inspired from line contact and is suitable for slender ellipses [43], had been used before by Reusner [80] and Nayak and Johnson [59], who treated the contact problem for roller bearings. Le-The applied his contact algorithm to the wheel/rail contact problem and showed that the wheel/rail profile combination S1002/UIC60 leads to strongly non-elliptical contact patches, especially at positions where contact-point jumps are encountered for lateral shifting of the rigid wheel profile on the rigid rail profile.

A third contact model was published by Paul and Hashemi in 1981 [70]. They abandoned the half-space assumption and developed a boundary-element approach for conformal contact. Using an approximate analytical expression for the influence function, they solved the conformal contact problem between the railhead and the throat of the wheel flange.

In recent years, two opposing trends are observed in the development of contact algorithms for non-Hertzian geometries. One trend goes to advanced finite-element formulations and another trend goes to approximate and fast solution methods.

The first trend to advanced numerical methods is described by Knothe et al. in their state-of-the-art article from 2001 [49]. Finite-element methods, not being limited to half-spaces, have the capability to include arbitrary contact geometries. In addition, they can account for all kinds of non-linearities such as temperature ef-

fects and plastic deformation. Their drawback is the computational time required. Knothe et al. stated in 2001 [49] that, despite many advances in the field and the development of powerful computers, a solution of the time-dependent problem with a complete three-dimensional contact model was not yet available. Many contributions to the finite-element modelling of the wheel/rail contact have been added in the last few years (see e.g. [15, 84, 87]) but, to the knowledge of the author, Knothe et al.'s statement is still true today at least with regard to tangential contact modelling.

The second trend to simplified, approximate solutions is outlined in an article by Piotrowski and Chollet [73]. Contact algorithms implemented in online simulations of vehicle system dynamics and high-frequency wheel/rail interaction models have to be fast. Generally, neither the earlier mentioned boundary-element methods nor the finite-element methods meet this requirement. Therefore a lot of effort is made to develop fast, approximate methods that are reliable in non-Hertzian conditions. Piotrowski and Chollet [73] distinguish between two types of methods: (1) multi-Hertzian methods and (2) virtual-penetration methods. The first type of methods has been developed by Pascal and Sauvage [69]. They replace multi-point contacts and non-elliptical contact patches by a set of Hertzian ellipses. They also proposed a method to replace the set of ellipses by a single equivalent ellipse. While the multi-Hertzian method agrees reasonably with Kalker's CONTACT, the equivalent-ellipse method has its limitations. Piotrowski and Chollet [73] estimate that the latter method is still adequate for dynamic simulations, but the former should be used for surface stress analysis and wear calculations. The second type of methods estimates the contact area from the interpenetration area that is obtained by virtually penetrating the undeformed surfaces. Such virtual-penetration methods have been proposed by Ayasse and Chollet [3], Linder [54] and Piotrowski and Kik [74]. Owing to the assumption that the normal stress distribution is elliptical in the direction of rolling in a similar manner as presented in Equation (2.23), these methods are valid for quasi-Hertzian cases, where the contact conditions do not deviate much from Hertzian conditions [73].

A third and widely used type of fast and approximate models for normal contact is based on a bedding of independent springs, the Winkler bedding. These methods are fast because the coupling between different points in the continuum is omitted. Examples of the application of Winkler beddings in wheel/rail contact are the DPRS models proposed by Remington and Webb [75] for the three-dimensional case and by Ford and Thompson [23] for the two-dimensional case. The DPRS models were adapted such that they agree with Hertzian contact for smooth surfaces and then applied to consider roughness with wavelengths down to the millimetre range in the contact area.

To treat the contact problem for surfaces with roughness of even shorter wavelengths down to the micrometre range, two types of models have historically been

used: statistical models and deterministic models. The statistical models rely on a description of the surfaces with some statistical parameters, an assumed simple asperity shape and an assumed asperity height distribution function. The best-known of these models has been proposed by Greenwood and Williamson [28] for nominally flat surfaces and extended by Greenwood and Tripp [27] to the contact of rough spheres. In this model, the surface asperities are approximated by hemispheres that all have the same radius, and a Gaussian distribution of asperity heights is adopted. Alonso and Giménez applied this model with several sets of wheel roughness data and found that the apparent pressure distribution for a typical wheel/rail load condition is almost identical to the Hertzian distribution [2]. The apparent pressure distribution is calculated by dividing the force calculated in a small surface element by the area of the element. Deterministic models solve the contact problem for the actual measured surface topography. Such a model has recently been applied by Bucher et al. to the wheel/rail contact [9]. They pointed out that the results are dependent on the wavelength content of the measured roughness, which is influenced by the measurement resolution and the data processing. The shorter the wavelengths considered, the more the real area of contact decreases and the more the real pressure distribution becomes cleft. The results of Bucher et al. are partly contradictory to results obtained with the simpler Greenwood/Tripp model. It still seems to be an open question whether and in which way micro-roughness influences the wheel/rail interaction.

Independently of this question, it is unrealistic to include contact models with a resolution in the micrometre range into wheel/rail interaction models, due to the high computational effort and the lack of input data. As already mentioned, however, it is possible to include the roughness distribution with a lower resolution and thereby consider the effect of roughness wavelengths in the order of the contact dimensions.

The literature review showed that significant errors may occur if Hertzian contact theory is used in cases where the radii of curvature are not constant in the contact area. It is as yet difficult to draw a general final conclusion about the applicability of Hertzian contact in wheel/rail contact. The problem is that in all investigations only some specific examples and/or simplified geometries have been considered. An extensive investigation of contact between different real wheel and rail surfaces would be needed in order to decide whether the errors occurring when using Hertzian contact theory for non-Hertzian geometry are still acceptable in praxis. The answer to this question certainly depends also on the purpose of investigation. In cases where only the total normal force is of interest, Hertzian contact theory has a wider range of applicability than in e.g. wear calculations where the pressure distribution and size and shape of the contact area are of interest.

2.8 Tangential contact models

In this section, tangential contact models for rolling contact are reviewed in the context of wheel/rail interaction. Particular attention is given to the requirements on tangential contact models with regard to squeal prediction.

Before the relevant contact models are outlined, the phenomena occurring in the contact zone during rolling are discussed briefly. An important quantity in the context of tangential contact is the creepage as defined in *Section 2.4*. It characterises "the overall relative motion" [88] between wheel and rail. The corresponding relative velocities would be observed in the contact *point* if wheel and rail did not deform locally. In reality, wheel and rail deform locally and make contact over an *area*. In part of this area, the creepage is completely compensated for by the local tangential deformation of the bodies, and the bodies 'stick' to each other. In the remaining part of the contact area, the creepage is partly relieved by local 'slip'. This situation is illustrated by the following equations for the local slip, which are valid for linear elastic materials [43]:

$$s_\tau = w_\tau - v\frac{\partial u_\tau}{\partial x} + \frac{\partial u_\tau}{\partial t}\,, \quad \tau = 1, 2\,, \tag{2.24}$$

where v is the rolling velocity, s_τ the local slip (i.e. the local relative velocity), u_τ the displacement difference between wheel and rail, and w_τ the 'rigid' (overall) slip obtained from the longitudinal, lateral and spin creepages, ξ, η and ϕ, by

$$w_1 = [\xi - \phi y]v \tag{2.25}$$

$$w_2 = [\eta + \phi x]v\,. \tag{2.26}$$

These equations are formulated for wheel and rail particles flowing through the contact zone and a coordinate system moving with the contact zone along the rail. The rolling direction is the x-direction or 1-direction, and the lateral direction is denoted y-direction or 2-direction. In the stick area, the local slip vanishes, i.e. $s_1 = s_2 = 0$.

Equations (2.24) describe the general case of transient (or non-steady-state) rolling. In steady-state rolling, the term showing explicit time dependence vanishes and the equations for the local slip read

$$s_\tau = w_\tau - v\frac{\partial u_\tau}{\partial x}\,, \quad \tau = 1, 2\,. \tag{2.27}$$

The rolling process can be treated as steady-state if relevant contact variables (e.g. contact pressure, imposed creepages, form and size of the contact area etc.) do not change significantly during the time needed for wheel and rail particles to pass through the contact zone [47]. Or formulated differently, a transient analysis becomes necessary if the characteristic wavelength of the motion (rolling speed/characteristic frequency) is in the order of, or smaller than, the contact patch length [47].

Tangential contact models for rolling contact have been discussed in review articles by Elkins [20], Kalker [44] and Knothe et al. [49]. Valuable sources are also the books by Johnson [41] and Kalker [43]. The outline of wheel/rail rolling contact models given below follows mainly the review article by Kalker [44]. All the presented models rely on the half-space assumption (unless stated otherwise) and the assumption of a constant friction coefficient μ.

Carter [10], who was concerned with driving or braked locomotive wheels, investigated the tractive rolling of a cylinder representing the wheel on an elastic half-space representing the rail. Tractive rolling means that a resultant tangential force (creep force) is transmitted in the contact. Carter carried out a two-dimensional (2D) analysis including only longitudinal forces for the case of steady-state rolling, and presented an exact solution of the problem. Figure 2.6(a) shows a sketch of the distribution of the tangential traction obtained over the width of the contact strip; see e.g. [41] for the equations. A stick zone is located at the leading edge of the

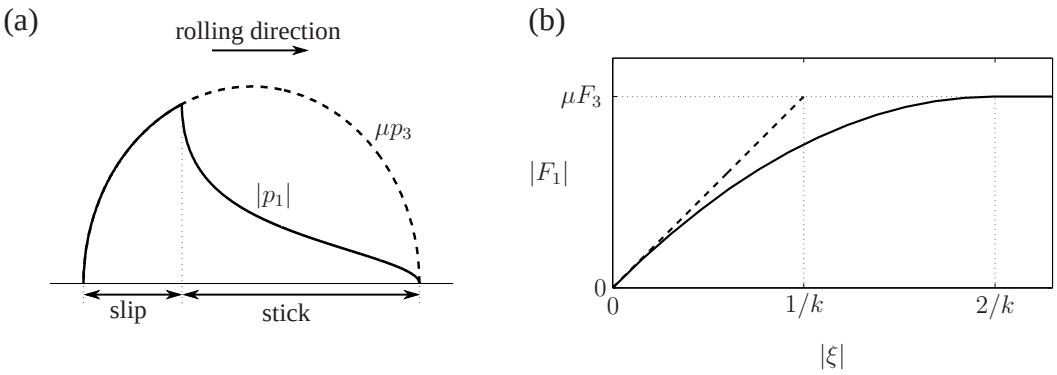

Figure 2.6: 2D steady-state rolling contact according to Carter: (a) Tangential traction $|p_1|$ (———) and traction bound μp_3 ($- - -$), (b) Creep force/creepage law from Equation (2.28) (———) in comparison to linear theory ($- - -$).

contact, while slip occurs in the remainder of the contact adjacent to the trailing edge. In the stick zone, the tangential (longitudinal) traction $|p_1|$ is below the traction bound μp_3 determined by friction coefficient μ and contact pressure p_3. In the slip zone, in contrast, the tangential traction equals the traction bound. The extent of the slip zone increases with increasing longitudinal creepage $|\xi|$ until gross sliding is reached. The resulting creep force/creepage law is given by [44]

$$\frac{F_1}{\mu F_3} = \begin{cases} -k\xi + \frac{1}{4}k^2\xi|\xi| & \text{if } k|\xi| \le 2 \\ -\mathrm{sign}(\xi) & \text{if } k|\xi| > 2 \end{cases}, \tag{2.28}$$

where $k = 4R_\mathrm{W}/[\mu a]$ is Carter's creepage coefficient, and R_W and a denote respectively the wheel radius and the half-width of the contact strip. The force F_1

is the longitudinal creep force and F_3 denotes the total normal contact force. Figure 2.6(b) illustrates that the non-linear creep force/creepage law can be approximated by a linear theory for small creepages. The creep force F_1 is bounded by the limiting force μF_3 corresponding to gross sliding.

Several models have been proposed for three-dimensional (3D) rolling contact under steady-state conditions. Four of these models are outlined here:

Kalker developed a linear theory, which is the exact solution in the limiting case of 'no slip' and results in a good approximation for small creepages [44]; cf. Figure 2.6(b) in the 2D case. Under the assumption that the contact area is elliptical according to Hertz theory with semi-axes a and b, the longitudinal and lateral creep forces, F_1 and F_2, are obtained as [44]

$$F_1 = -c^2 G C_{11} \xi \tag{2.29}$$

$$F_2 = -c^2 G C_{22} \eta - c^3 G C_{23} \phi \,, \tag{2.30}$$

where $c = [ab]^{1/2}$ and G is the shear modulus. Kalker's creepage coefficients C_{11}, C_{22} and C_{23}, which are tabulated e.g. in [44], are solely functions of the ratio a/b of the semi-axes of the elliptical contact area and Poisson's ratio ν.

Vermeulen and Johnson [102] presented an approximate non-linear rolling contact theory for longitudinal and lateral creepage in the case of an elliptical contact area. The effect of spin is disregarded. The theory is based on the approximation that also the stick zone is elliptical. The model by Vermeulen and Johnson gives reasonably good results for the creep force/creepage relation in comparison to laboratory experiments [102] and Kalker's 'exact' theory (see *Section 2.7* and below) [44].

Shen, Hedrick and Elkins [83] improved the theory by Vermeulen and Johnson with regard to longitudinal and lateral creepage, and introduced the influence of spin. Kalker [44] estimates that their theory is, however, valid only for cases with small spin.

Kalker also developed a simplified theory [42, 44], in which he replaced the elastic half-space by a bedding of uncoupled springs. In this model, the displacement difference between wheel and rail in one point is assumed proportional to the surface traction in the same point and independent of the surface traction in all other points. Kalker determined the proportionality constant on the basis of his linear theory. Nevertheless, he also found good quantitative agreement with his 'exact' theory for large creepages in the case of an elliptical contact area. The simplified theory implemented in the computer program FASTSIM is, according to Kalker, about 400 times faster than the implementation CONTACT of his 'exact' theory [44].

Only a few theories deal with transient rolling contact. Knothe and Groß-Thebing [46] and Groß-Thebing [29] presented a linear, transient theory. They calculated frequency-dependent complex creep coefficients for the case of small harmonic variations of

the creepages around a reference state. While the reference state in [46] is the state with vanishing creepages, the theory has been extended to an arbitrary reference state in [29]. Recently, Alonso and Giménez [1] proposed a modified version of FASTSIM, which allows the consideration of larger harmonic variations of one type of creepage. They found reasonably good agreement with Kalker's 'exact' theory in the case of an elliptical contact area and a constant normal force.

The only available rolling contact theory that is fully non-linear and transient is Kalker's 'exact' theory implemented in the computer program CONTACT [43]. This theory, which has already been outlined in *Section 2.7*, solves the kinematic equations for transient rolling contact (2.24) and accounts for arbitrary varying creepages, normal forces and contact geometries as long as the half-space assumption is fulfilled. Its main drawback is a relatively long computation time.

In the context of squeal prediction, a non-linear tangential contact model is needed since large creepages and large variations of creepages occur. Furthermore, a transient model should be used, since typical wavelengths are in the order of or smaller than the contact patch length. For example, for a train speed of $36\,\mathrm{km/h}$ and a squeal frequency of $1\,\mathrm{kHz}$, the wavelength obtained is $1\,\mathrm{cm}$, which is in the range of the typical contact patch length. The assumption that the contact variables do not change significantly during the time that is needed for wheel and rail particles to pass through the contact zone, thus does not hold for squealing. Finally, the tangential contact model should allow for both a constant friction coefficient and a velocity-dependent friction coefficient, in order to be able to consider the two different squeal mechanisms according to *Section 2.4*.

As discussed above, the only non-linear and transient rolling contact model is CONTACT. The model has been developed by Kalker under the assumption of a constant friction coefficient. An extension to slip-velocity dependent friction has recently been proposed by Croft [13]. However, due to the computational effort required, CONTACT has so far not been used online in a squeal model.

In the absence of a suitable transient theory, authors of squeal models have instead implemented simpler steady-state formulations. Périard [71] introduced a slip-velocity dependent friction coefficient in Kalker's numerical steady-state algorithm FASTSIM. More commonly, analytical formulas are used to represent the creep force/creepage relation (which is sometimes given in terms of a friction characteristic) [12, 16, 22, 33]. Chiello et al. [12], for example, adopted an exponential creep force/creepage relation, which they combined with a linearly falling friction coefficient. In the simplest case, point contact is assumed together with a constant friction coefficient [25]. As no simulation results are available so far from a squeal model that includes a transient rolling contact model, it is difficult to assess the errors introduced by simplified contact models.

Chapter 3

Implementation of a wheel/rail interaction model in the time domain

Based on the literature review presented in the previous chapter, the requirements on the combined vertical and tangential wheel/rail interaction model developed in this thesis can now be specified and modelling choices can be justified.

In order to include the non-linearities occurring in the contact zone, the interaction model has to be formulated in the time domain. Non-linearities cannot be neglected in the case of discrete irregularities, and are also important in the case of severe roughness and/or low static preload. The occurrence of squeal is an intrinsically non-linear phenomenon and only time-domain models are able to predict squeal amplitudes. As calculation times for time-domain models are generally high, special attention has to be given to computational efficiency. An efficient technique that has been pointed out in the literature review is the representation of track and wheel by Green's functions, which can be pre-calculated before starting the dynamic simulations. This technique will be used here. On the one hand, the usage of Green's functions implies a simplification since only linear wheel and track models can be represented by Green's functions. On the other hand, this approach is very versatile because any wheel or track model represented by Green's functions can be used without changing the mathematical formulation of the interaction model.

The wheel and track model should represent with sufficient precision the dynamic behaviour of wheel and track in the frequency range of interest, which has been identified as the range from $100\,\mathrm{Hz}$ to at least $5\,\mathrm{kHz}$. In vertical wheel/rail interaction, it is generally considered sufficient to include the wheel as a rigid mass. Accordingly, the wheel model is kept simple when only vertical interaction is calculated. As the extension to tangential interaction requires the inclusion of the wheel's flexibility, a second wheel model, which is a modal wheel model derived from a detailed FE model, is introduced for this purpose. The inclusion of the wheel's modal behaviour is essential for the prediction of squeal noise. Following similar reasoning as for the wheel, two different track models are used. The first track model, which is suitable for vertical wheel/rail interaction only, comprises

a Rayleigh-Timoshenko beam model of the rail and discrete supports. The cross-sectional deformations occurring at high frequencies are thus not included and according to the discussion in *Section 2.5* the validity of this track model above about $2.5\,\mathrm{kHz}$ has to be questioned. In order to be able to model tangential interaction, a second track model is introduced, which is based on a waveguide finite element model of the rail. This model includes the cross-sectional deformations of the rail and is consequently also valid in the very-high-frequency range. A minor drawback of this model is that the rail support is modelled as continuous, which implies that parametric excitation due to discrete supports is not included. Wheel and track models and their respective representation as Green's functions are presented in detail in *Sections 3.2* and *3.3*.

The question whether the Hertzian contact model is sufficient for vertical wheel/rail interaction could not be answered completely in the literature review. For this reason, two non-Hertzian contact models are introduced in this thesis, which allow contributing to the clarification of this question. A two-dimensional model is presented in *Section 3.4.1* and a three-dimensional one in *Section 3.4.2*. These two models include the contact-filter effect dynamically and do not require the calculation of an equivalent roughness as pre-processing step.

Kalker's theory for transient rolling contact [43] is the most complete tangential contact model available in the literature and it is therefore selected as tangential contact model. Due to its high computational cost, this model has not been used previously in a wheel/rail interaction model in the context of noise prediction. The efficiency of the selected time-domain approach based on pre-calculated Green's functions makes it possible to include Kalker's model. It is, however, not known whether such a detailed modelling of the tangential contact is actually required for the prediction of noise.

3.1 Reference frame

In the dynamic simulations, the wheel is moved along the rail with constant velocity v. Its absolute position in the rolling direction on the rail at time t is indicated by the coordinate $x = v\,t$. In order to describe the variables in the contact zone, a moving reference frame (x', y', z') is introduced (see Figure 3.1), which moves with the nominal contact point along the rail. The nominal contact point is the point where the rigid profiles of wheel and rail touch first, when contact is initiated. Its lateral position, which is kept constant in the simulation, is either pre-calculated or assumed. The x'-axis (1-axis) points in the rolling direction along the rail. The lateral direction is the y'-direction (2-direction) pointing towards the field side of the wheel. The vertical (or normal) z'-coordinate (3-coordinate) points into the rail. It is assumed that the distributions of tangential stresses and contact pressure

in the contact zone can be represented by the point forces F_1, F_2 and F_3, when the excitation of wheel and track to vibrations is calculated. These point forces act in the nominal contact point.

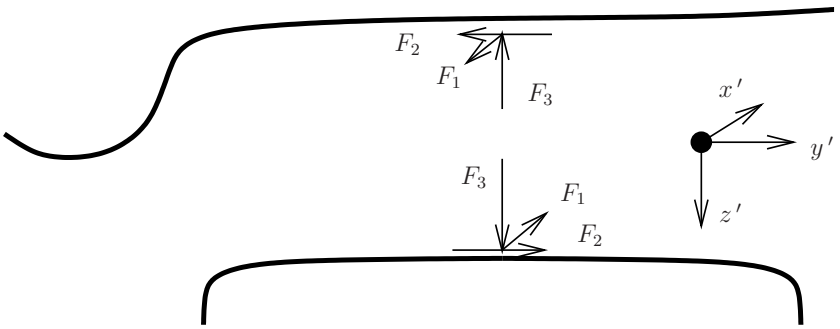

Figure 3.1: Moving reference frame of the interaction model.

3.2 Wheel models

Before the different wheel models are introduced, the general procedure of including the wheel dynamics in the interaction model is described. This procedure is the same for all types of linear wheel models that can be represented by Green's functions.

The vehicle model includes one wheel (or half a wheelset) and the primary suspension. The wheel rotation is neglected. All the vehicle components above the primary suspension of the wheel are simplified to a static preload, P.

The displacements of the wheel at the contact point due to the wheel's global dynamics are denoted $\xi_j^{\mathrm{W}}(t),\ j = 1,2,3$. In the frequency domain, the wheel is represented by its receptances

$$\tilde{G}_{ij}^{\mathrm{W}}(f) = \frac{\xi_j^{\mathrm{W}}(f)}{F_i(f)}, \quad i,j = 1,2,3\,, \tag{3.1}$$

which indicate the displacement response, $\xi_j^{\mathrm{W}}(f)$, to a harmonically exciting contact force, $F_i(f)$, at frequency f. In the time domain, the wheel is represented by its impulse response functions (Green's functions), $\tilde{g}_{ij}^{\mathrm{W}}(t)$, which are obtained from the receptances by an inverse Fourier transform:

$$\tilde{g}_{ij}^{\mathrm{W}}(t) = \mathscr{F}^{-1}\left(\tilde{G}_{ij}^{\mathrm{W}}(f)\right), \quad i,j = 1,2,3\,. \tag{3.2}$$

In the interaction model, the displacements of the wheel, $\xi_j^{\mathrm{W}}(t)$, are obtained by convoluting the contact forces with the Green's functions of the wheel:

$$\xi_j^{\mathrm{W}}(t) = -\int_0^t \sum_{i=1}^{3} F_i(\tau)\tilde{g}_{ij}^{\mathrm{W}}(t-\tau)\,\mathrm{d}\tau\,, \quad j = 1,2,3\,. \tag{3.3}$$

Introducing the time increment Δt and the discrete time vector with the elements

$$t(\alpha) = [\alpha - 1]\Delta t, \quad \alpha = 1, 2, \ldots N_t\,, \tag{3.4}$$

the discretised version of Equation (3.3) at time step α reads

$$\xi_j^{\mathrm{W}}(\alpha) = -\sum_{n=1}^{\min(N_{\mathrm{W}},\alpha)} \sum_{i=1}^{3} g_{ij}^{\mathrm{W}}(n)\, F_i(\alpha - n + 1)\,, \tag{3.5}$$

where the $g_{ij}^{\mathrm{W}}(n)$ are the discrete time-integrated versions of the Green's functions $\tilde{g}_{ij}^{\mathrm{W}}(n)$ of the wheel, which have the N_{W} elements

$$g_{ij}^{\mathrm{W}}(n) = \begin{cases} 0.5\Delta t\, \tilde{g}_{ij}^{\mathrm{W}}([n-1]\Delta t) & \text{for} \quad n = 1, N_{\mathrm{W}} \\ \Delta t\, \tilde{g}_{ij}^{\mathrm{W}}([n-1]\Delta t) & \text{for} \quad n = 2, 3 \ldots N_{\mathrm{W}} - 1 \end{cases}\,. \tag{3.6}$$

At $N_{\mathrm{W}}\,\Delta t$, the Green's functions are assumed to have decayed to zero.

At time step α, the forces at previous time steps are known and the only unknown forces are $F_i(\alpha)$. The sum in Equation (3.5) can therefore be split up into an unknown term containing $F_i(\alpha)$ and a known term denoted $\xi_j^{\mathrm{W,\,old}}(\alpha)$

$$\begin{aligned} \xi_j^{\mathrm{W}}(\alpha) &= -\sum_{i=1}^{3} g_{ij}^{\mathrm{W}}(1) F_i(\alpha) - \sum_{n=2}^{\min(N_{\mathrm{W}},\alpha)} \sum_{i=1}^{3} g_{ij}^{\mathrm{W}}(n)\, F_i(\alpha - n + 1) \\ &= -\sum_{i=1}^{3} g_{ij}^{\mathrm{W}}(1) F_i(\alpha) - \xi_j^{\mathrm{W,\,old}}(\alpha)\,. \end{aligned} \tag{3.7}$$

If the first value in the Green's functions, $g_{ij}^{\mathrm{W}}(1)$, is set to zero, the wheel displacement at the current time step is only influenced by the forces in previous time steps. It is thus known:

$$\xi_j^{\mathrm{W}}(\alpha) = -\xi_j^{\mathrm{W,\,old}}(\alpha)\,. \tag{3.8}$$

In a detailed wheel model, the first value of the Green's function describes mainly the local instantaneous deformation of the wheel at the contact point occurring in the same instant as the applied force is acting. The wheel models used are, however, not detailed enough to give realistic values of the local deformation (which is instead modelled in the contact model) and the first value of the Green's functions obtained is relatively small. The same applies also for the track models used. It is

thus a reasonable assumption to set the first value of the Green's function to zero. In addition, this assumption considerably simplifies the equation system that has to be solved at each time step in the interaction model. In cases where only vertical interaction was considered in the interaction model (*Papers I to III*), the first value of the Green's functions has not been set to zero, while the assumption has been used in the combined vertical/tangential interaction model (*Papers IV and V*).

3.2.1 Rigid wheel models

Two rigid wheel models are introduced, which are suitable for use in vertical wheel/rail interaction only. The first model of this type is a single-degree-of-freedom (1-dof) system comprising half the wheelset mass, M_{W}, and the primary suspension consisting of a spring with constant k_{S} in parallel with a damper with constant c_{S} (see Figure 3.2). The second rigid wheel model is a two-degree-of-

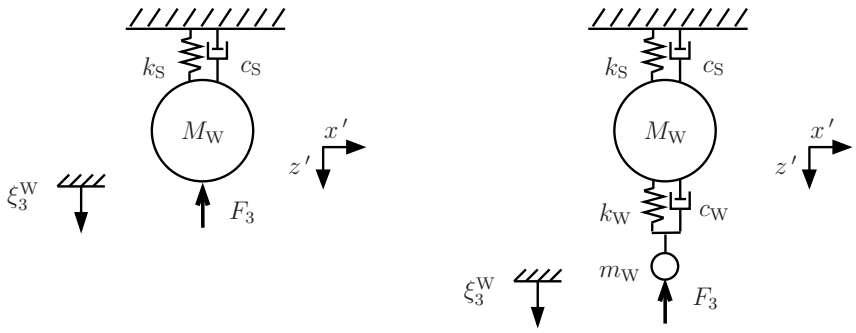

Figure 3.2: Wheel modelled as single-degree-of-freedom system (left) and two-degree-of-freedom system (right).

freedom (2-dof) system that includes in comparison to the 1-dof model an additional small mass, m_{W}, and an additional spring with constant k_{W} in parallel with a damper with constant c_{W} (see Figure 3.2). These additional components do not have a direct physical meaning, but can be used to tune the receptance in the higher frequency range to resemble the receptance obtained with a finite-element model (see *Section 3.2.2*). Provided that modal behaviour of the wheel is not of interest, this type of wheel model has shown good performance [62, 109].

Figure 3.3 shows a comparison of the receptances G_{33} of the two wheel models for the numerical values of the parameters $M_{\mathrm{W}} = 341.5\,\mathrm{kg}$, m_{W}=3 kg, $k_{\mathrm{S}} = 1.12\,\mathrm{MN/m}$, $c_{\mathrm{S}} = 13.2\,\mathrm{kNs/m}$, $k_{\mathrm{W}} = 6.0\,\mathrm{GN/m}$ and $c_{\mathrm{W}} = 155\,\mathrm{kNs/m}$. For this configuration, the receptances differ from each other from above about $100\,\mathrm{Hz}$. The Green's functions g_{33} of both wheel models appear almost identical, as can be seen in Figure 3.4. It should however be noted that the scale in Figure 3.4 is linear and therefore does not allow identifying differences in the dynamics at lower levels.

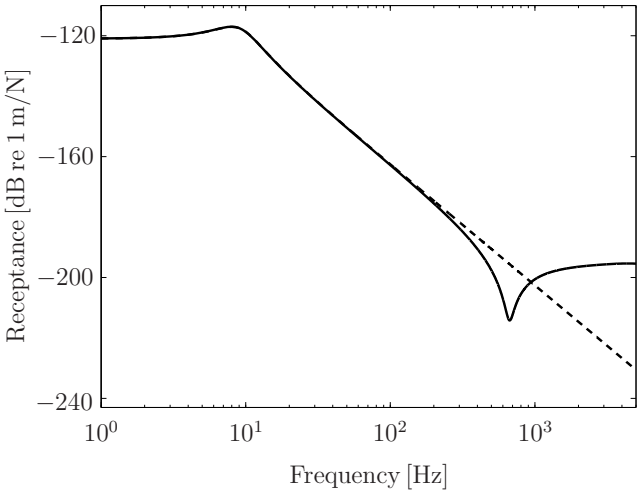

Figure 3.3: Magnitude of the wheel receptance G_{33}: 1-dof model ($-\ -\ -$), 2-dof model (———).

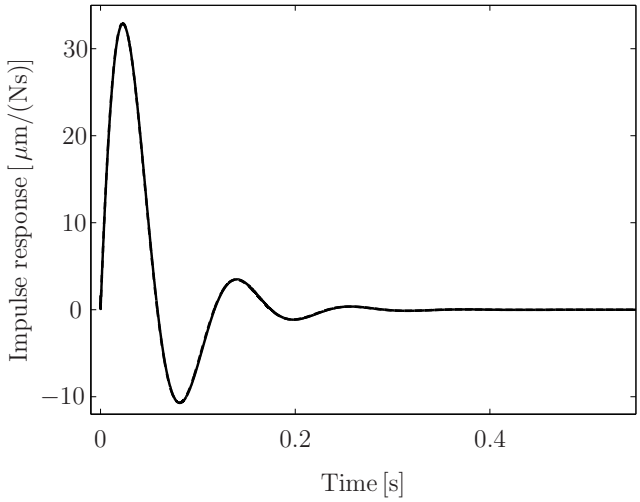

Figure 3.4: Impulse response g_{33} of the wheel: 1-dof model ($-\ -\ -$), 2-dof model (———). The curves appear almost identical.

3.2.2 Flexible wheel model

The flexible wheel model is a finite element (FE) model based on axi-symmetric elements, similar to the model presented in [90], and could be used by courtesy of David Thompson (ISVR). The help of Briony Croft (previously ISVR) with the implementation of the model is greatly acknowledged. A commercial finite element software has been used. The model comprises a single wheel without the wheel axle. A rigid constraint is applied at the inner edge of the hub, where the wheel would be connected to the axle. Figure 3.5(a) shows the meshed cross-section of the selected wheel, which is a 780-mm C20 metro wheel. The steel wheel has a Young's modulus of $E^{\mathrm{W}} = 207\,\mathrm{GPa}$, a Poisson ratio $\nu^{\mathrm{W}} = 0.3$ and a density $\rho^{\mathrm{W}} = 7860\,\mathrm{kg/m^3}$.

The eigenfrequencies (Figure 3.6) and corresponding eigenmodes (Figures 3.7-3.9)

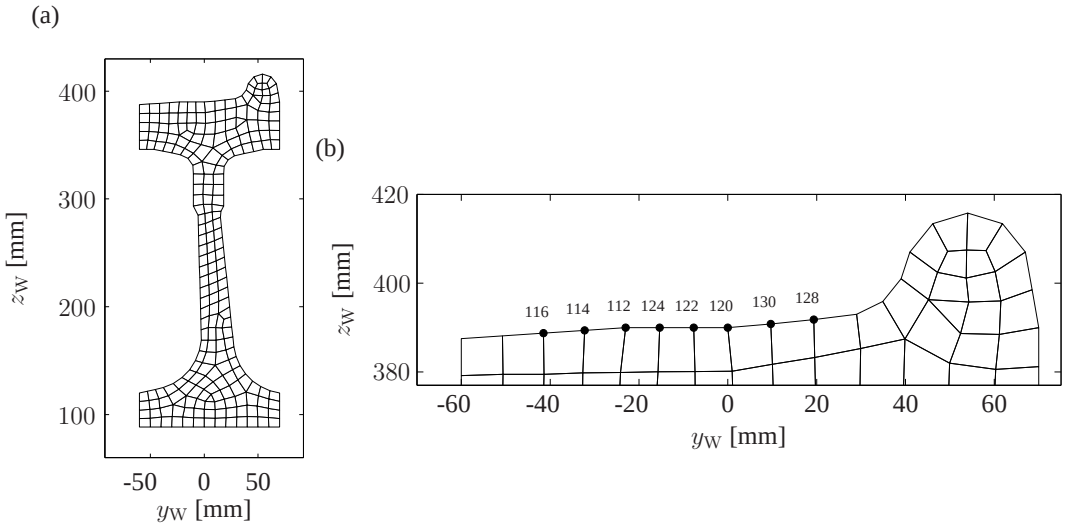

Figure 3.5: FE mesh of the C20 wheel cross-section: (a) complete mesh and (b) zoom on the tread with selected node numbers.

of this FE model have been calculated in the range up to $7\,\mathrm{kHz}$. Similar to the eigenmodes of a flat disc, the eigenmodes of the wheel are classified according to their predominant motion into axial, radial and circumferential modes, which have n nodal diameters and m nodal circles [88]. The axial modes will be denoted (n,m,a). As $m > 0$ does not occur for radial and circumferential modes in the frequency range of interest, they will be referred to as (n,r) and (n,c), respectively. The mode shapes have a harmonic variation $A \sin n\varphi$ (or $A \cos n\varphi$) around the circumference, where φ is the angular coordinate in the circumferential direction [88]. The amplitude A varies with the axial (lateral) and radial position on the wheel. The radial and axial components of this amplitude A are depicted in the section plots of the different types of mode shapes in Figures 3.7-3.9 . (The third circumferential

component is not seen.) As the cross-section of the wheel is not symmetric, the axial modes (Figure 3.7) also have a component of motion in radial direction and the radial modes (Figure 3.8) in axial direction. For illustration purposes, three of the mode shapes are also shown as three-dimensional plots in Figure 3.10.

The omission of the axle is known to lead to errors in eigenfrequency and mode shape for modes with $n \leq 1$, but has a negligible effect on higher-order modes [88]. As especially higher-order axial modes (with $n \geq 2$) have been found to be important for curve squeal [12], this is not seen as critical for the investigation of squeal noise.

The eigenmodes are assigned a modal damping ζ using the approximate values proposed by Thompson [88]:

$$\zeta = \begin{cases} 10^{-3} & \text{for} \quad n = 0 \\ 10^{-2} & \text{for} \quad n = 1 \\ 10^{-4} & \text{for} \quad n \geq 2 \end{cases} . \tag{3.9}$$

The mode (1,r) is assigned a damping of 1, since this mode appears too strongly in the frequency response function, when the influence of the axle is disregarded [88]. These damping values are used as a first approximation. Considering the importance of wheel damping for the occurrence of squeal, measured modal damping values should be used for the investigation of a specific squeal problem in a specific curve.

Starting from the modal basis, the receptances of the wheel in the pre-determined contact point on the wheel tread are calculated by modal superposition. The receptance $\tilde{G}^{\mathrm{W}}_{jk}(\omega)$, which represents the response in degree of freedom k due to a harmonic force of unit amplitude and angular frequency ω applied in degree of freedom j is obtained as [88]

$$\tilde{G}^{\mathrm{W}}_{jk}(\omega) = \sum_r \frac{\Phi_{jr}\Phi_{kr}}{m_r\left(\omega_r^2 - \omega^2 + i2\gamma_r\omega_r\omega\right)} \tag{3.10}$$

where Φ_{jr} is the amplitude of mode shape r in the degree of freedom j and the variables ω_r and m_r are the angular frequency and the modal mass of mode r, respectively. In addition to the eigenmodes calculated with the FE-model of the wheel, the rigid body modes of the complete wheelset, notably translation in vertical and lateral direction and rotation in the vertical/lateral plane, have to be taken into account in the modal summation [88].

Figure 3.11 shows as examples the vertical and lateral point receptances and the vertical/lateral cross-receptance calculated in the node 114 (see Figure 3.5(b)) situated towards the field side of the wheel tread at a distance of $32\,\mathrm{mm}$ from the centre. A strong coupling between the vertical and lateral directions can be seen at this location. The first $0.4\,\mathrm{s}$ of impulse response functions corresponding to the

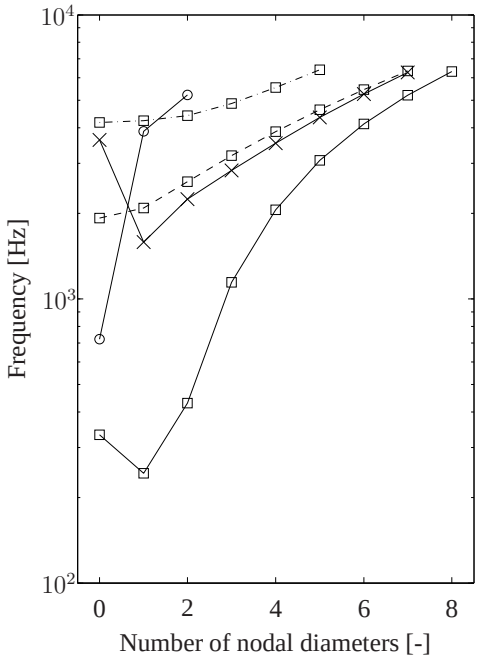

Figure 3.6: Eigenfrequencies of the C20 wheel up to $7\,\mathrm{kHz}$ calculated with the FE model: axial modes (□), radial modes (×) and circumferential modes (○) with zero nodal circles (———), one nodal circle (– – –) and two nodal circles (– · –).

receptances from Figure 3.11 are presented in Figure 3.12. The total length of the impulse response signals taken into account is $20\,\mathrm{s}$.

In order to demonstrate the applicability of the 2-dof wheel model from *Section 3.2.1*, a comparison of the vertical receptances of the 2-dof model and the flexible wheel model is presented in Figure 3.13. The receptance of the 2-dof model has been tuned to resemble the receptance of the flexible wheel model by adapting the parameters k_W and c_W. The receptance of the flexible wheel model used is the vertical point receptance calculated in the node 120 at the centre of the wheel tread, including only the rigid body mode in vertical translation (and all flexible wheel modes). At the centre of the wheel tread, only a small coupling between vertical and lateral directions arises due to the asymmetry of the wheel cross-section. The best fit of the receptance of the 2-dof model (corresponding to the parameter values already used in Figure 3.3 and listed in *Section 3.2.1*) is shown in Figure 3.13. The 2-dof model captures well the anti-resonance in the wheel receptance at about $650\,\mathrm{Hz}$ and gives a mean value of the receptance at higher frequencies. The comparison of the 2-dof model to the flexible model is less favourable if the receptance calculated at node 114 is taken, where the coupling between vertical and lateral directions has a bigger influence (Figure 3.14).

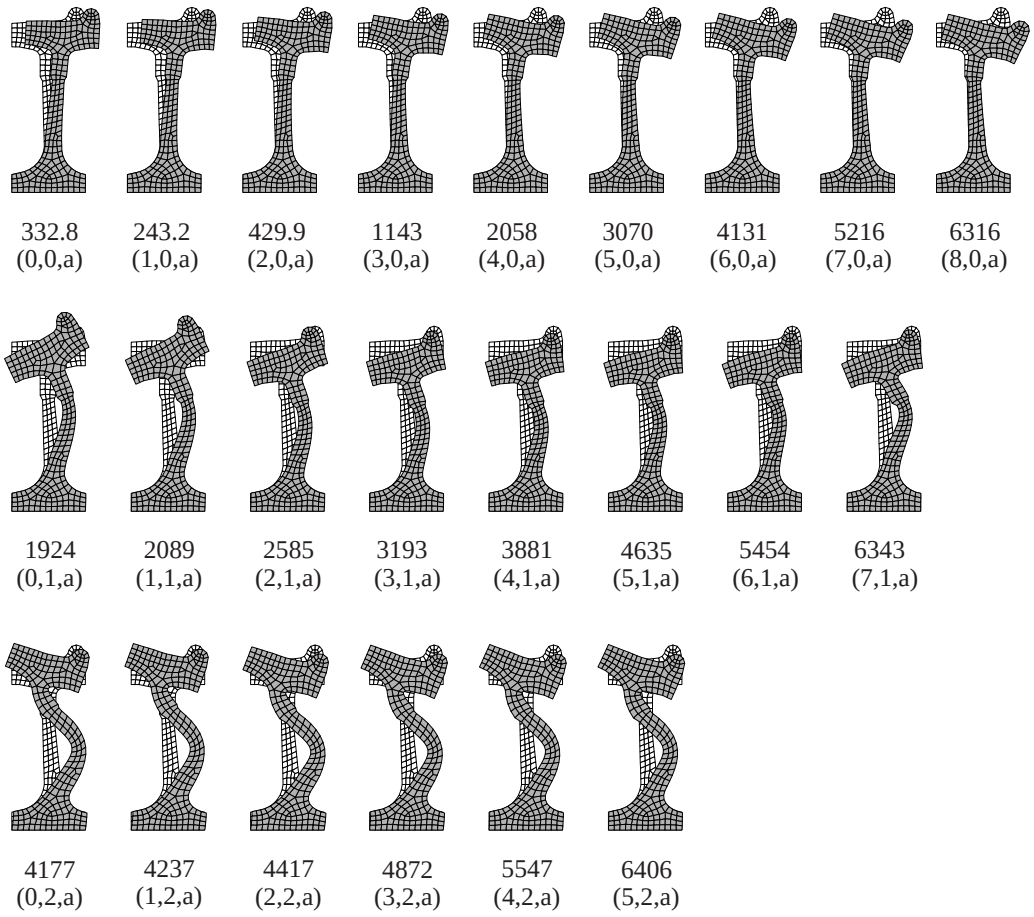

Figure 3.7: Axial modes (n,m,a).

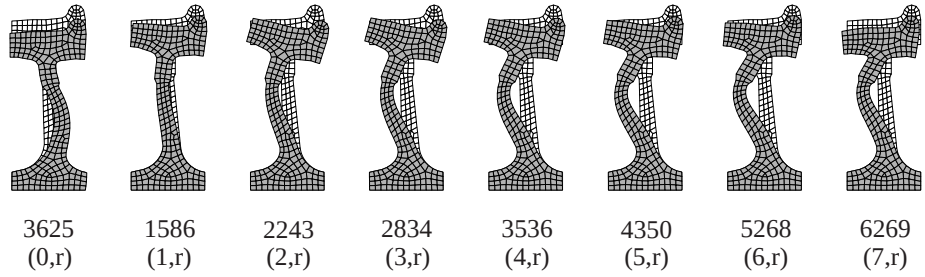

Figure 3.8: Radial modes (n,r).

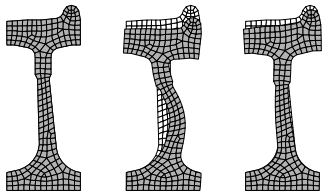

Figure 3.9: Circumferential modes (n,c).

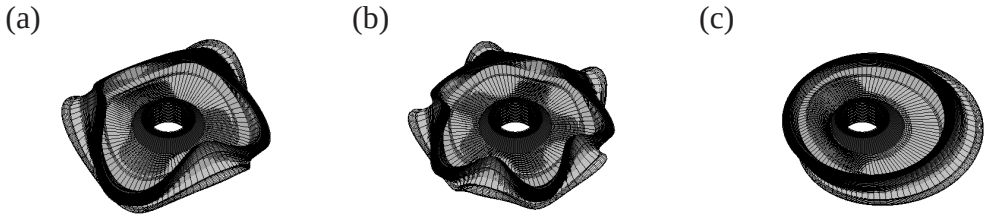

Figure 3.10: Examples of wheel modes: (a) Axial mode (3,0,a), (b) Axial mode (5,0,a), (c) Radial mode (1,r).

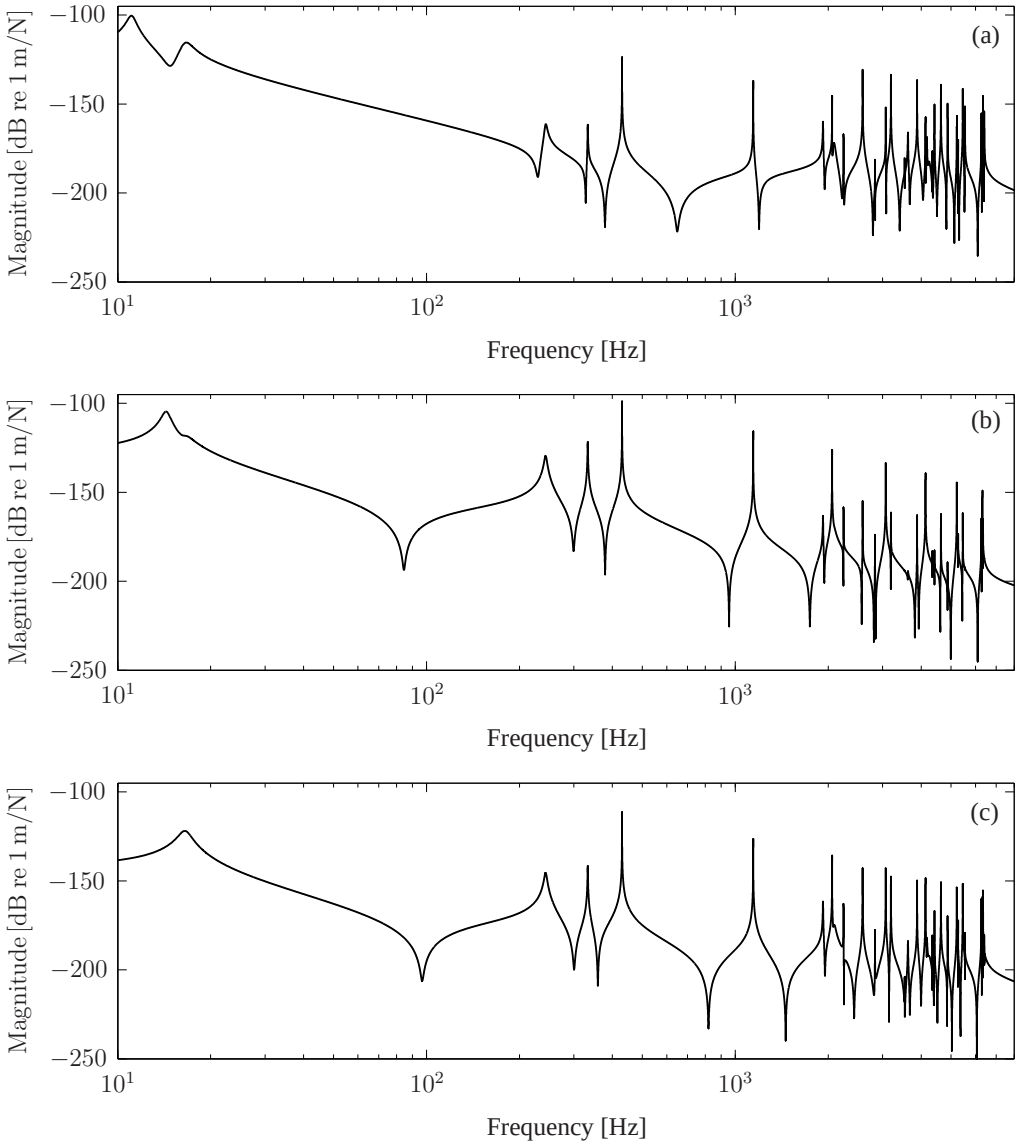

Figure 3.11: Magnitudes of the wheel receptance at the tread at $y_{\mathrm{W}} = -32\,\mathrm{mm}$: (a) vertical point receptance, (b) lateral point receptance, (c) vertical/lateral cross-receptance.

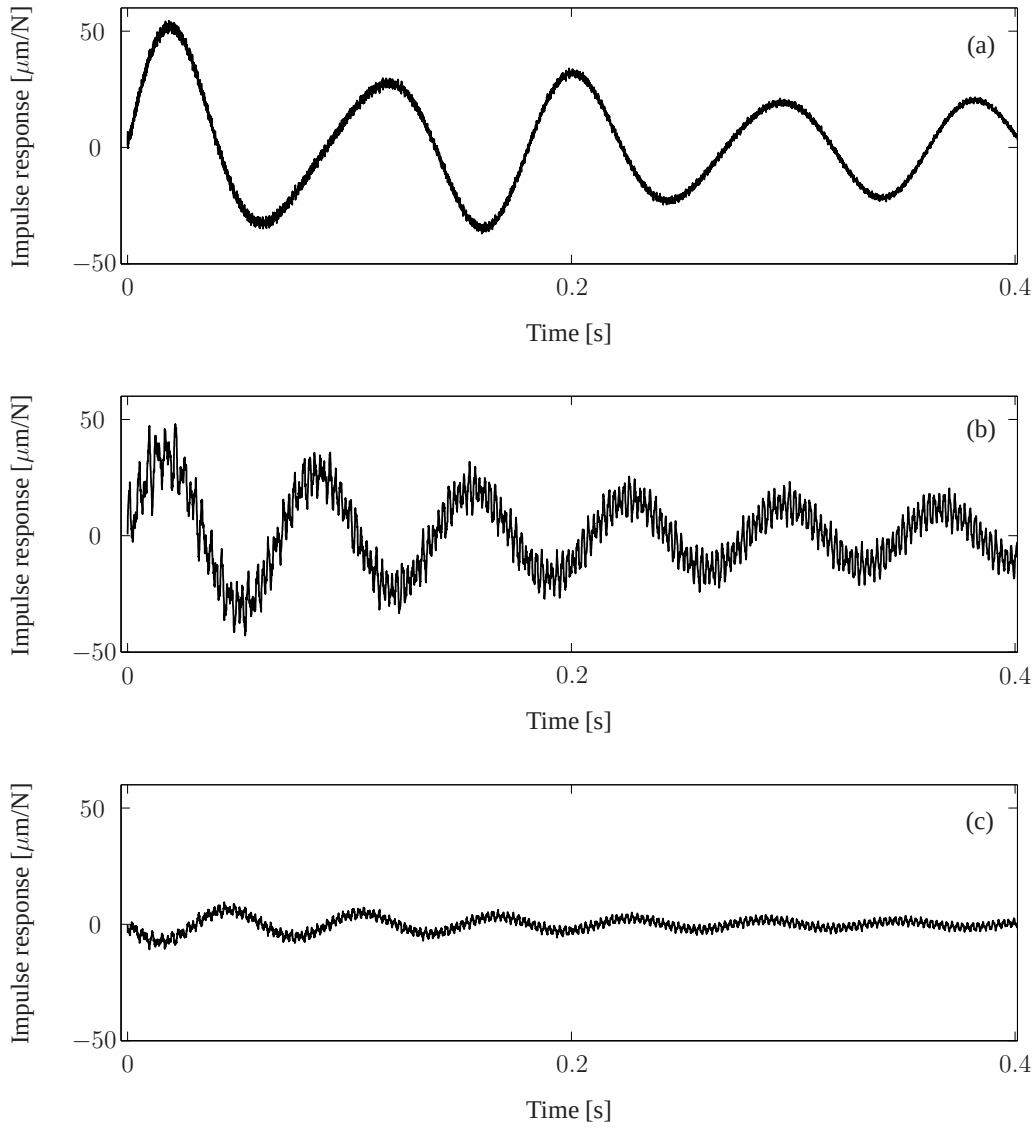

Figure 3.12: Impulse response functions of the wheel calculated at $y_{\mathrm{W}} = -32\,\mathrm{mm}$ at the tread : (a) vertical, (b) lateral, (c) vertical/lateral.

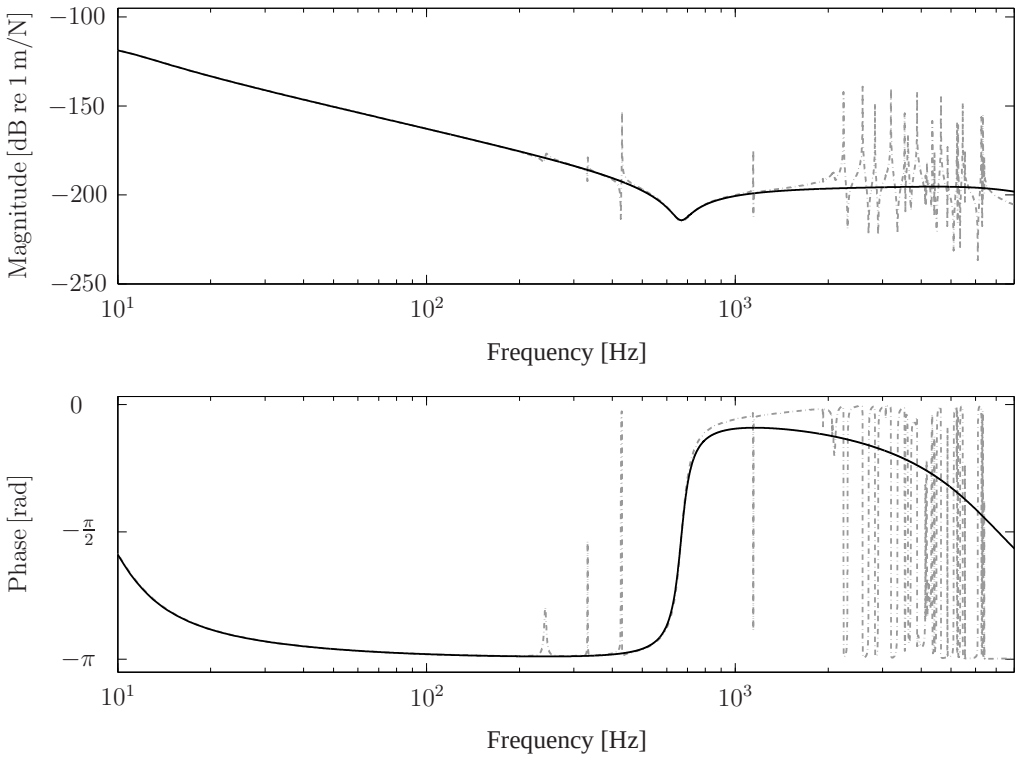

Figure 3.13: Best fit of the receptance of the 2-dof wheel model (———) to the vertical point receptance of the flexible wheel model calculated in node 120 at the centre of the wheel tread (– · –).

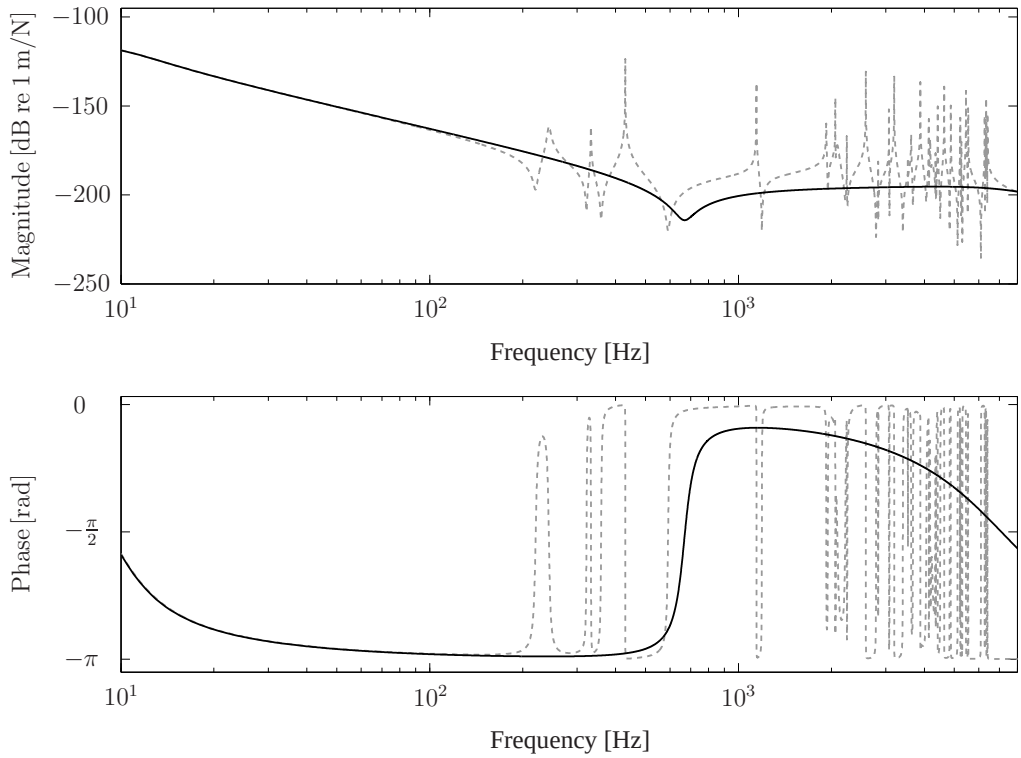

Figure 3.14: Comparison between the receptance of the 2-dof wheel model from Figure 3.13 (———) and the vertical point receptance of the flexible wheel model calculated in the off-centre node 114 (− · −).

3.3 Track models

The inclusion of the track dynamics in the wheel/rail interaction model is very similar to the inclusion of the wheel dynamics. However, while the rotation of the wheel was neglected in *Section 3.2*, the motion of the nominal contact point on the rail cannot be neglected. Consequently, a special type of Green's functions is needed, which take the motion of the contact point into account. These moving Green's functions [67], $\tilde{g}_{ij,v}^{\mathrm{R},x_0}(t)$, describe, for excitation of the rail (index R) in i-direction at the position x_0 at time $t_0 = 0$, the displacement response of the rail in j-direction at a point moving at train speed v away from the excitation, thus at the nominal contact point on the rail.

In the interaction model, the displacement of the rail in the nominal contact point, $\xi_j^{\mathrm{R}}(t)$, $j = 1, 2, 3$, is calculated by convoluting the contact forces with the moving Green's functions of the rail

$$\xi_j^{\mathrm{R}}(t) = \int_0^t \sum_{i=1}^{3} F_i(\tau) \tilde{g}_{ij,v}^{R,v\tau}(t-\tau)\,\mathrm{d}\tau\,, \quad j = 1, 2, 3\,. \tag{3.11}$$

The discrete version of $\tilde{g}_{ij,v}^{\mathrm{R},x_0}(t)$, denoted $g_{ij,v}^{\mathrm{R},x_0}(n)$, is constructed from a series of track transfer receptances, $\tilde{G}_{ij}^{\mathrm{R},\,x_0,\,x_0+\chi}(f)$. The superscripts specify the excitation point, x_0, and the response point, $x_0 + \chi$. The (ordinary) Green's functions, $\tilde{g}_{ij}^{\mathrm{R},\,x_0,\,x_0+\chi}(t)$, corresponding to these track receptances, are obtained by inverse Fourier transform

$$\tilde{g}_{ij}^{\mathrm{R},\,x_0,\,x_0+\chi}(t) = \mathscr{F}^{-1}\left(\tilde{G}_{ij}^{\mathrm{R},\,x_0,\,x_0+\chi}(f)\right)\,. \tag{3.12}$$

Exploiting the coupling

$$\Delta x = v\Delta t \tag{3.13}$$

between the time increment, Δt, and the space increment, Δx, the discrete moving Green's functions are constructed as

$$g_{ij,v}^{\mathrm{R},x_0}(n) = \begin{cases} 0.5\Delta t\; \tilde{g}_{ij}^{\mathrm{R},\,x_0,\,x_0+[n-1]\Delta x}([n-1]\Delta t) & \text{for} \quad n = 1, N_{\mathrm{R}} \\ \Delta t\; \tilde{g}_{ij}^{\mathrm{R},\,x_0,\,x_0+[n-1]\Delta x}([n-1]\Delta t) & \text{for} \quad n = 2, 3 \ldots N_{\mathrm{R}} - 1 \end{cases}, \tag{3.14}$$

where N_{R} is the number of samples. At $N_{\mathrm{R}}\Delta t$, the Green's functions of the rail are assumed to have decayed to zero.

The discrete version of Equation (3.11) formulated at time step α reads

$$\xi_j^{\mathrm{R}}(\alpha) = \sum_{n=1}^{\min(N_{\mathrm{R}},\alpha)} \sum_{i=1}^{3} g_{ij,v}^{\mathrm{R},v[\alpha-n]\Delta t}(n)\, F_i(\alpha - n + 1)\,, \quad j = 1, 2, 3\,. \tag{3.15}$$

Analogous to Equation (3.7), this equation can be split up into a part containing the only unknown forces, $F_i(\alpha)$, and the known part, $\xi_j^{\mathrm{R,\,old}}(\alpha)$,

$$\begin{aligned}\xi_j^{\mathrm{R}}(\alpha) &= \sum_{i=1}^{3} g_{ij,v}^{\mathrm{R},v[\alpha-1]\Delta t}(1)\, F_i(\alpha) + \sum_{n=2}^{\min(N_{\mathrm{W}},\alpha)} \sum_{i=1}^{3} g_{ij,v}^{\mathrm{R},v[\alpha-n]\Delta t}(n)\, F_i(\alpha-n+1) \\ &= \sum_{i=1}^{3} g_{ij,v}^{\mathrm{R},v[\alpha-1]\Delta t}(1)\, F_i(\alpha) + \xi_j^{\mathrm{R,\,old}}(\alpha)\,. \end{aligned} \tag{3.16}$$

If the first value in the Green's functions, $g_{ij,v}^{\mathrm{R},v[\alpha-1]\Delta t}(1)$, is again set to zero, the rail displacement at the current time step is only influenced by the forces in previous time steps and given by

$$\xi_j^{\mathrm{R}}(\alpha) = \xi_j^{\mathrm{R,\,old}}(\alpha)\,. \tag{3.17}$$

3.3.1 Finite element model of the track based on Rayleigh-Timoshenko beam elements

The first track model, which is suitable for vertical wheel/rail interaction only, is a linear finite element (FE) model based on a rail description by Rayleigh-Timoshenko beam elements. This model is implemented in the wheel/rail interaction model DIFF [64] and could be used by courtesy of Jens Nielsen.

The track model takes into account discrete supports and has a length of 70 sleeper bays with sleeper spacing L_{S}. Both rail ends are clamped. The rail, which is a UIC60 rail with bending stiffness EI, shear stiffness kGA and mass per unit beam length m', is modelled by eight Rayleigh-Timoshenko beam elements per sleeper bay. The discrete supports are composed of railpads and sleepers on ballast; see Figure 3.15. The railpads are represented by a spring with stiffness k_{P} in parallel with a viscous damper with constant c_{P}. The sleepers are modelled as rigid masses m_{SL} and the ballast is represented by a spring with stiffness k_{B} in parallel with a viscous damper with constant c_{B}. A detailed description of the track model is given in references [64] and [61].

Figure 3.16 shows the magnitude of the vertical track point receptance, $\tilde{G}_{33}^{\mathrm{R},x_0,x_0}$, and three examples of transfer receptances, $\tilde{G}_{33}^{\mathrm{R},x_0,x_0+\chi}$, for two different excitation positions x_0. The numerical values of the parameters used are $EI = 6.4\,\mathrm{MNm^2}$, $kGA = 250\,\mathrm{MN}$, $m' = 60\,\mathrm{kg/m}$, $L_{\mathrm{S}} = 0.65\,\mathrm{m}$, $k_{\mathrm{P}} = 120\,\mathrm{MN/m}$, $c_{\mathrm{P}} = 16\,\mathrm{kNs/m}$, $m_{\mathrm{SL}} = 125\,\mathrm{kg}$, $k_{\mathrm{B}} = 140\,\mathrm{MN/m}$ and $c_{\mathrm{B}} = 165\,\mathrm{kNs/m}$. For excitation at midspan between two sleeper positions, $x_0 = 0.5\,L_{\mathrm{S}}$, a sharp peak is observed at $943\,\mathrm{Hz}$, which is the pinned-pinned resonance frequency. Correspondingly, the receptances for excitation over a sleeper, $x_0 = 0$, show an anti-resonance in this frequency range, which has slightly shifted to higher frequencies. Additionally, the receptances for both excitation positions have an anti-resonance at about $2640\,\mathrm{Hz}$.

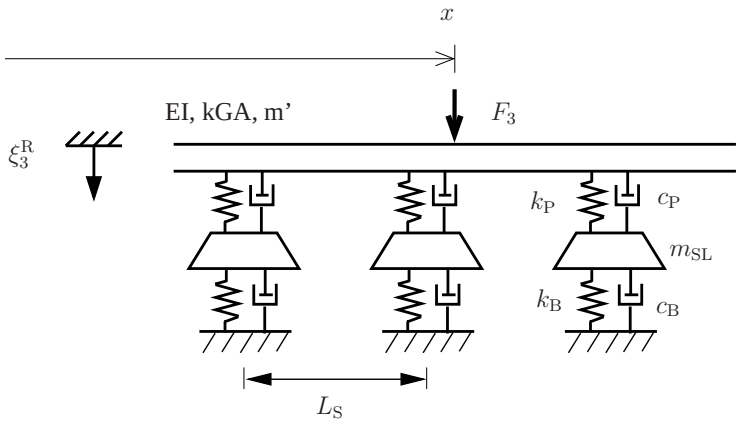

Figure 3.15: Rail model with discrete supports.

Examples of moving Green's functions for two different excitation positions and three different velocities are presented in Figure 3.17. The additional high-frequency oscillations for excitation at $x_0 = 0.5\,L_{\mathrm{S}}$ (Figure 3.17(b)) in comparison to excitation at $x_0 = 0$ (Figure 3.17(a)) are explained by the pinned-pinned resonance. Due to the periodicity of the track, $L_{\mathrm{S}}/\Delta x$ different moving Green's functions suffice to represent the track at each velocity v. With the parameters $L_{\mathrm{S}} = 0.65\,\mathrm{m}$ and $\Delta x = 1\,\mathrm{mm}$, this leads to 650 moving Green's functions.

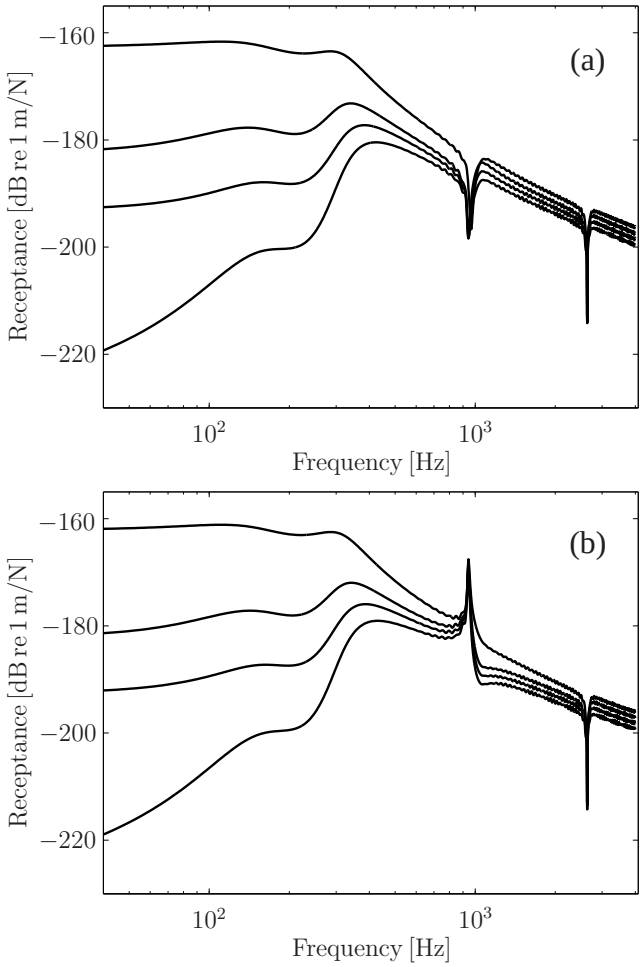

Figure 3.16: Magnitude of the track point and transfer receptances for excitation (a) above a sleeper position, $x_0 = 0$, and (b) at midspan between two sleeper positions, $x_0 = 0.5\,L_\mathrm{S}$: the plotted curves are from upper to lower $|\tilde{G}_{33}^{\mathrm{R},\,x_0,\,x_0}|$, $|\tilde{G}_{33}^{\mathrm{R},\,x_0,\,x_0+2\,L_\mathrm{S}}|$, $|\tilde{G}_{33}^{\mathrm{R},\,x_0,\,x_0+4\,L_\mathrm{S}}|$ and $|\tilde{G}_{33}^{\mathrm{R},\,x_0,\,x_0+6\,L_\mathrm{S}}|$.

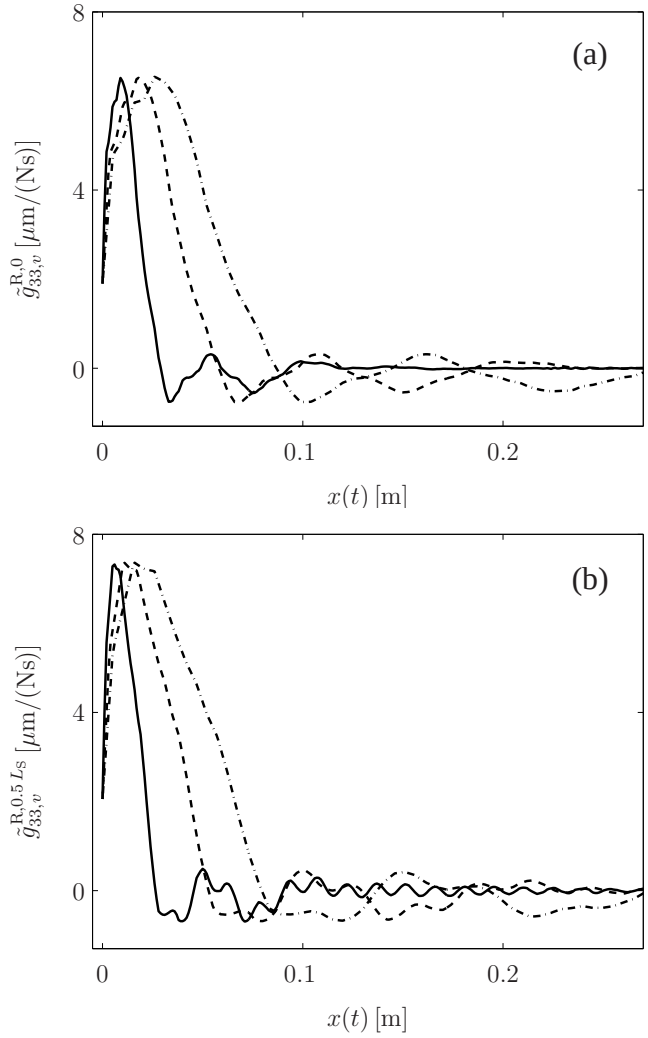

Figure 3.17: Moving Green's functions of the track for excitation (a) above a sleeper position, $x_0 = 0$, and (b) at midspan between two sleeper positions, $x_0 = 0.5\,L_\mathrm{S}$: —— $v = 50\,\mathrm{km/h}$, $- - -$ $v = 100\,\mathrm{km/h}$, $-\cdot-$ $v = 150\,\mathrm{km/h}$.

3.3.2 Waveguide finite element model of the track

The extension of the interaction model from vertical to tangential interaction requires the inclusion of cross-sectional deformations of the rail. For this reason, a waveguide finite element (WFE) model was built with the software package WANDS [66], which could be used by courtesy of the Dynamics Group at the Institute of Sound and Vibration, University of Southampton. This model takes advantage of the two-dimensional geometry of the rail having a constant cross-section in the x-direction, but nonetheless considers the three-dimensional nature of the vibration by assuming a wave-type solution along the rail.

The track model comprises one continuously supported rail of type BV50, which is a common Swedish rail type. The WFE mesh consisting of eight-noded isoparametric quadrilateral elements is presented in Figure 3.18(a). The material data of rail and support, which are chosen similar to the data given in [66], are listed in Table 3.1. The vertical stiffness of the continuous support corresponds to soft rail supports.

Table 3.1: Material properties of the continuously supported rail

	Rail	Pad
Young's modulus	207 GPa	4.8 MPa
Poisson's ratio	0.3	0.45
Density	7860 $\mathrm{kg/m^3}$	10 $\mathrm{kg/m^3}$
Damping loss factor	0.01	0.25

The equations of the WFE model are derived by Nilsson et al. in [66]. Only the most important equations are repeated here.

The basic principle of the WFE method is that the displacement $\mathbf{u} = [u_x, u_y, u_z]^{\mathrm{T}}$ – in x_{R}-, y_{R}- and z_{R}-directions – in one waveguide finite element is formulated as

$$\mathbf{u} = \mathbf{N}(y_{\mathrm{R}}, z_{\mathrm{R}})\hat{\mathbf{u}}(x_{\mathrm{R}})\,, \tag{3.18}$$

where $\hat{\mathbf{u}}$ is the vector of nodal displacements and $\mathbf{N}(y_{\mathrm{R}}, z_{\mathrm{R}})$ are two-dimensional (2D) FE shape functions; i.e. a 2D mesh is sufficient to describe the three-dimensional structure.

In the same manner as for standard FE models, the complete WFE model is assembled from the formulation on element level. Assuming a time dependence of $\mathrm{e}^{\mathrm{i}\omega t}$ and a wave of the type $\mathrm{e}^{-\mathrm{i}kx_{\mathrm{R}}}$, the assembled model reads

$$\left[\mathbf{K}(k) - \omega^2\mathbf{M}\right]\tilde{\mathbf{U}} = \tilde{\mathbf{F}}\,, \tag{3.19}$$

where $\mathbf{K}(k)$ is the stiffness matrix of the cross-section, which depends on the wavenumber k in x_{R}-direction, and $\mathbf{M}$ is the mass matrix of the cross-section. The

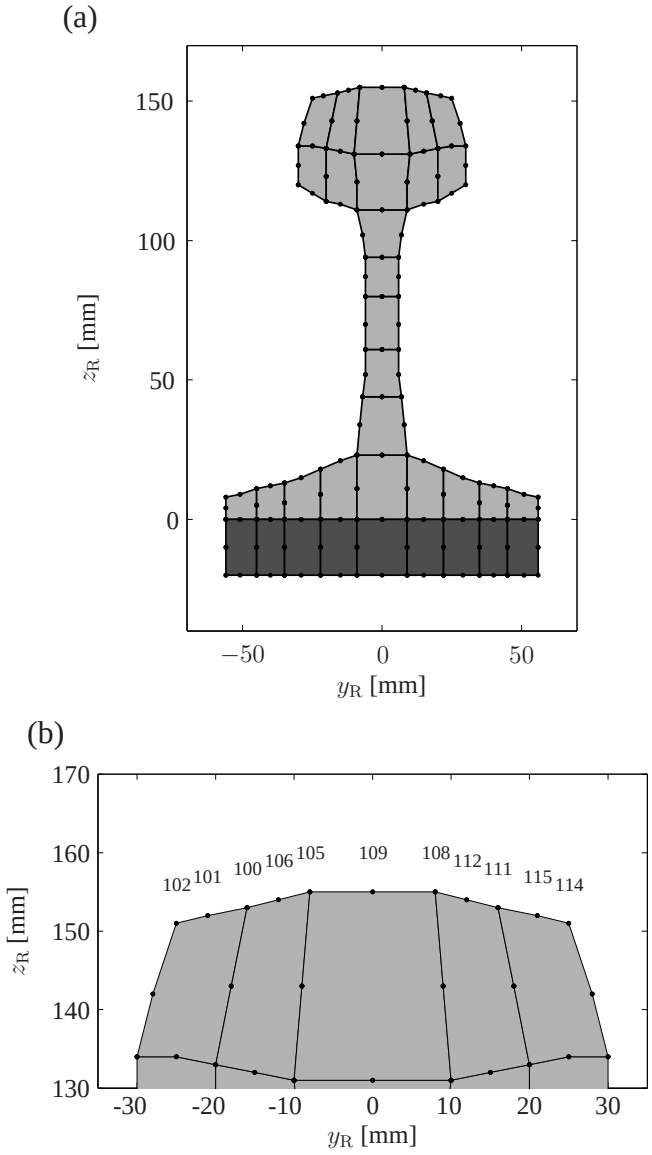

Figure 3.18: WFE mesh of the BV50 rail: (a) complete mesh and (b) zoom on rail head with selected node numbers. The dark grey area corresponds to the rail pad.

vector $\tilde{\mathbf{U}}$ is the global displacement vector, containing the displacements for all degrees of freedom in the cross-section, and the vector $\tilde{\mathbf{F}}$ is the vector of external forces. For free harmonic motion, the equation of the assembled WFE model,

$$\left[\mathbf{K}(k) - \omega^2 \mathbf{M}\right] \tilde{\mathbf{U}} = \mathbf{0}\,, \tag{3.20}$$

represents a (quadratic) eigenvalue problem in wavenumber k at a given frequency ω. The eigenvectors $\tilde{\mathbf{U}}_n$ correspond to cross-sectional wave shapes. The eigenval-

ues k_n obtained as complex-valued wavenumbers describe propagation and decay of the waves along the rail. The amplitude of a free harmonic wave propagating in the positive x_R-direction is thus described by

$$\hat{\mathbf{U}}_n(x_\mathrm{R}) = \tilde{\mathbf{U}}_n \mathrm{e}^{-\mathrm{i}k_n x_\mathrm{R}} \,. \tag{3.21}$$

The eigenvalues are represented in Figure 3.19 in the form of the dispersion relation. The wave shapes belonging to the different wave types in Figure 3.19 are shown in Figure 3.20 for the case $k_n = 1\,\mathrm{rad/m}$.

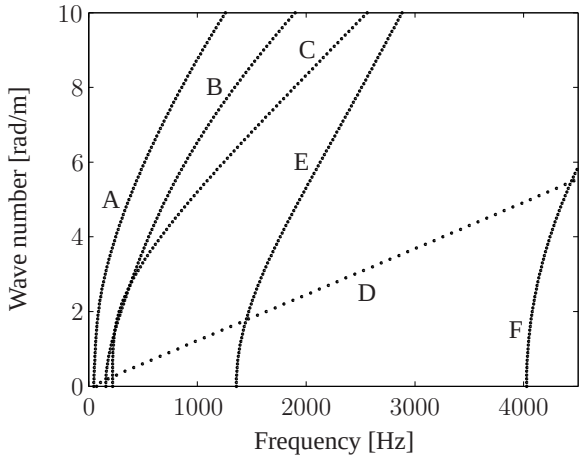

Figure 3.19: Dispersion relation for the continuously supported rail. Wave types: (A) Lateral bending wave, (B)Vertical bending wave, (C) Torsional wave, (D) Longitudinal wave, (E) Web bending wave 1, (F) Web bending wave 2.

The response to forced excitation is obtained by superposing the contributions from the different waves. The global displacement vector $\hat{\mathbf{U}}_0$ obtained due to a harmonic point force at $x_\mathrm{R} = 0$ reads, for propagation in the positive x_R-direction [66],

$$\hat{\mathbf{U}}_0(x_\mathrm{R}) = \sum_n A_n(\tilde{\mathbf{F}}_0)\tilde{\mathbf{U}}_n \mathrm{e}^{-\mathrm{i}k_n x_\mathrm{R}} \,, \tag{3.22}$$

where the force vector $\tilde{\mathbf{F}}_0$ is formulated in the wavenumber domain. The expression for the amplitudes $A_n(\tilde{\mathbf{F}}_0)$ is given in [66].

For a pre-determined lateral contact position on the rail head, receptances are calculated from the result of Equation (3.22). Figure 3.21 shows as examples the magnitude and phase of the vertical and lateral point receptances and the vertical/lateral cross-receptances in the node 112 (see Figure 3.18(b)). The offset of $12\,\mathrm{mm}$ of this node from the symmetry axis of the rail introduces the coupling between the vertical and lateral directions. The peaks in the magnitude of the receptances correspond to the cut-on of the different wave types (see Figure 3.19).

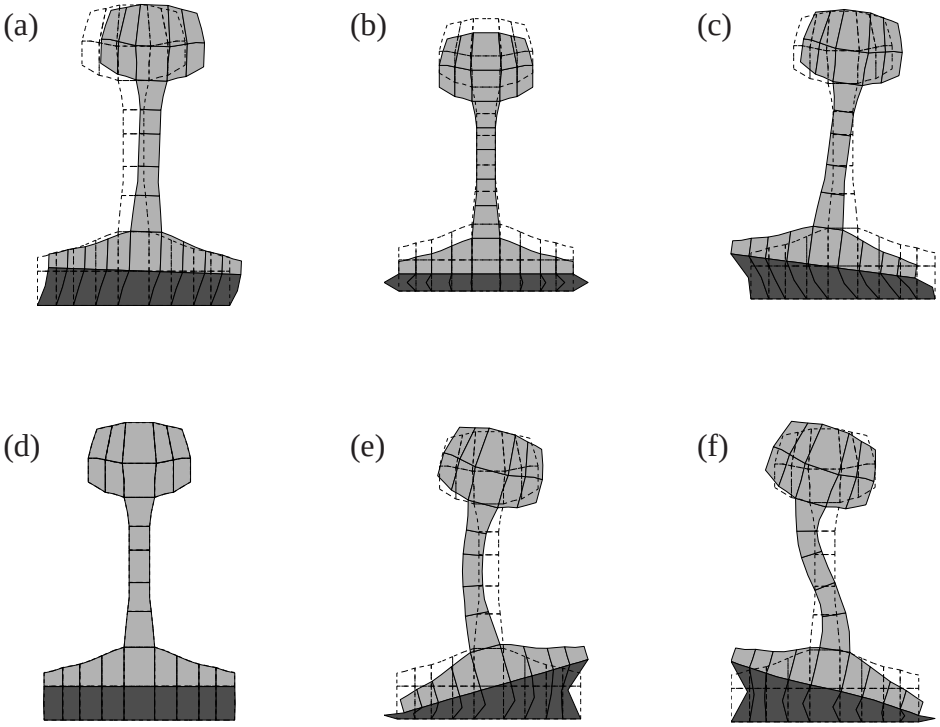

Figure 3.20: Wave shapes at $k = 1\,\mathrm{rad/m}$: (a) Lateral bending wave, (b) Vertical bending wave, (c) Torsional wave, (d) Longitudinal wave, (e) Web bending wave 1, (f) Web bending wave 2.

The corresponding moving Green's functions for a train speed of $50\,\mathrm{km/h}$ are presented in Figure 3.22. As the rail is continuously supported, the Green's functions $\tilde{g}_{ij,v}^{\mathrm{R},x_0}(t)$ do not differ from each other for different excitation positions x_0.

Figure 3.23 shows the influence of the lateral position of the excitation point on the vertical point receptance of the track. The larger the distance from the symmetry line of the track, the larger the influence of wave types with predominately lateral motion on the vertical receptance. The peaks emerging for an off-centre position of the excitation point are notably the peaks associated with the cut-on of lateral bending waves at about $50\,\mathrm{Hz}$ and web bending waves at $1362\,\mathrm{Hz}$ and $4030\,\mathrm{Hz}$.

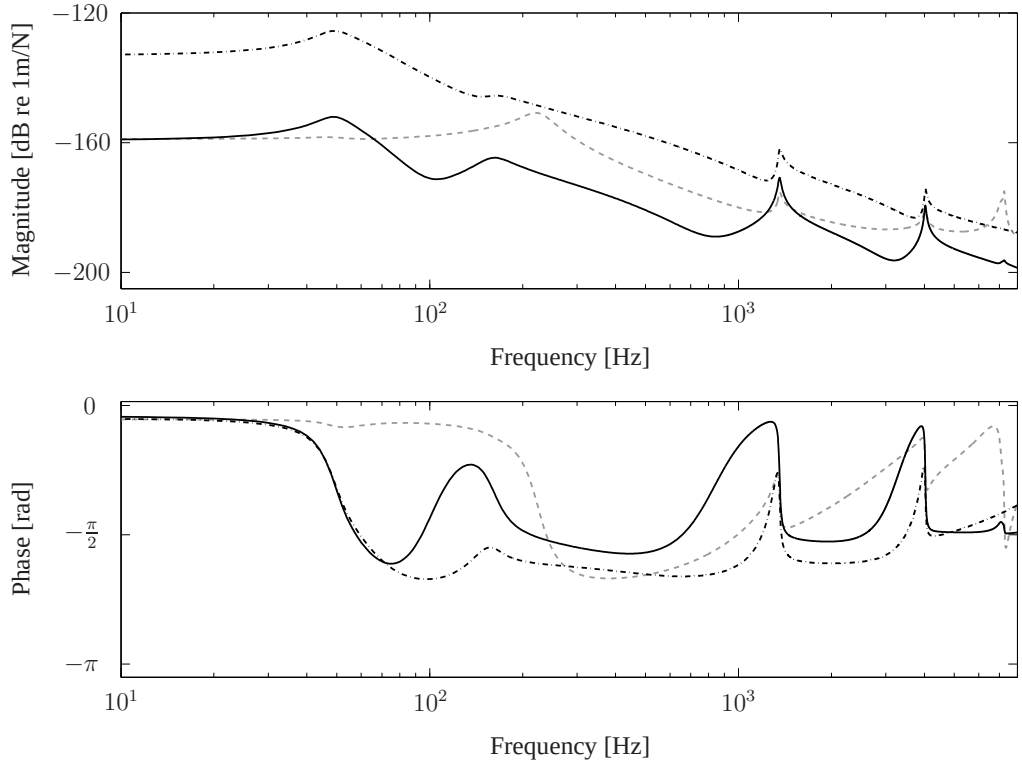

Figure 3.21: Magnitude and phase of the track receptance at the rail head at node 112: − − − (*grey*) vertical point receptance, − · − lateral point receptance, —— vertical/lateral cross-receptance.

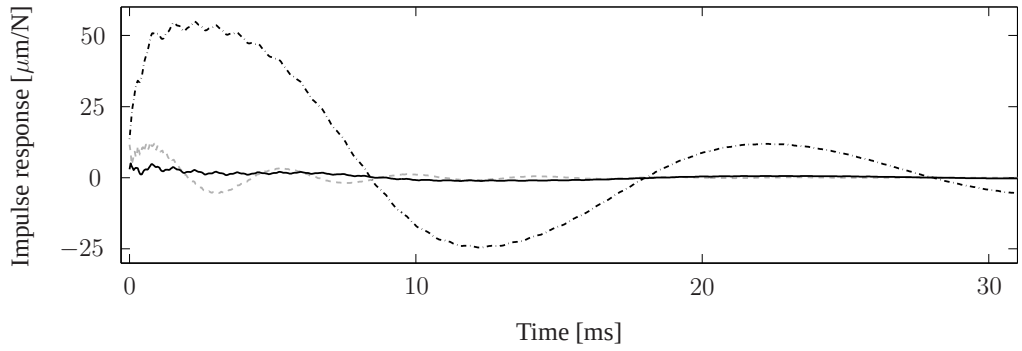

Figure 3.22: Moving Green's functions of the track calculated for a lateral contact position on the rail head at node 112 and a train speed $v = 50\,\mathrm{km/h}$: − − − (*grey*) vertical, − · − lateral, —— vertical/lateral.

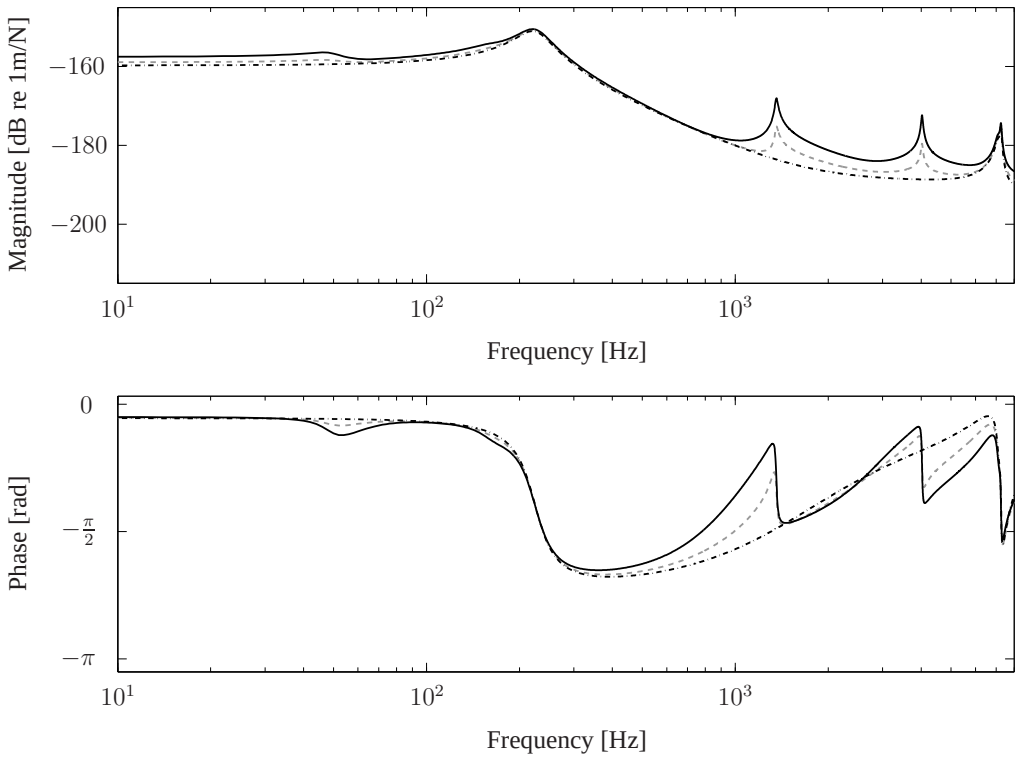

Figure 3.23: Comparisons of the magnitude and phase of the vertical point receptance calculated at different lateral positions on the rail head: Node 109 (– · –), node 112 (– – –, *grey*) and node 115 (——).

3.4 Non-Hertzian models for vertical contact

In this section, two non-linear and non-Hertzian models for the vertical contact between wheel and rail are presented, which are solved at each time step in the interaction model. Solving the vertical contact problem means (1) to determine the size and shape of the contact zone, and (2) to calculate the distribution of the contact pressure and the local vertical displacements in the contact zone. It is assumed that the vertical contact problem can be solved independently of the tangential contact problem.

3.4.1 Winkler bedding

The first of the two vertical contact models is a two-dimensional model. It is based on a Winkler bedding consisting of independent springs introduced between wheel and rail (see Figure 3.24). The model considers the roughness profile in one longitudinal line throughout the contact patch. For simplicity, only the rail is displayed

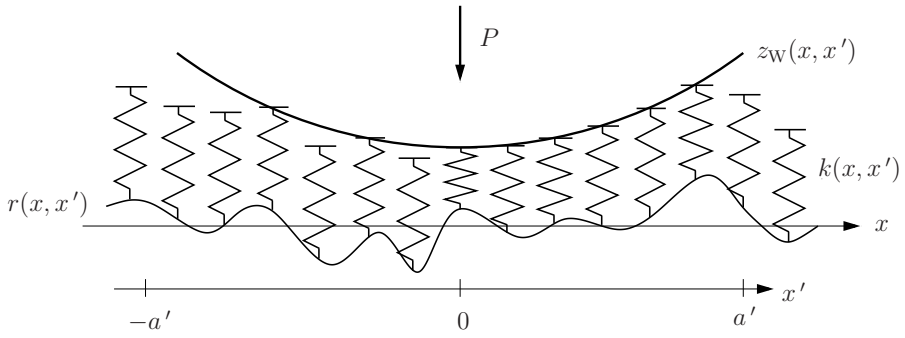

Figure 3.24: Bedding model for the wheel/rail contact.

as rough in Figure 3.24, but both wheel and rail are considered as rough. The combined roughness is contained in the variable $r(x) = r_{\mathrm{W}}(x) - r_{\mathrm{R}}(x)$. Both the wheel roughness, r_{W}, and the rail roughness, r_{R}, are taken positive in the direction of the z'-axis (see Figure 3.1).

For the wheel positioned at x, the deflection, $\Delta\zeta(x, x')$, of all involved contact springs depends on the vertical wheel displacement, $\xi_3^{\mathrm{W}}(x)$, the vertical rail displacement, $\xi_3^{\mathrm{R}}(x)$, the combined roughness, $r(x, x')$, and the wheel profile, $z_{\mathrm{W}}(x, x')$, as

$$\Delta\zeta(x, x') = \xi_3^{\mathrm{W}}(x) - \xi_3^{\mathrm{R}}(x) + r(x, x') + z_{\mathrm{W}}(x, x')\,. \tag{3.23}$$

The total vertical contact force is obtained by an integration over the bedding:

$$F_3(x) = \int_{-a'}^{a'} \tilde{k}(x, x')\,\Delta\zeta(x, x')\,\mathrm{d}x\,, \tag{3.24}$$

which has a stiffness per unit length

$$\tilde{k}(x,x') = \begin{cases} \frac{1}{2}\frac{E}{[1-\nu^2]} & \text{for} \quad \Delta\zeta(x,x') \geq 0 \\ 0 & \text{for} \quad \Delta\zeta(x,x') < 0 \end{cases} , \tag{3.25}$$

where E is the Young's modulus and ν the Poisson's ratio of rail and wheel (assumed to be of the same material). The integration domain, $[-a', a']$, has to be chosen long enough to include all potential points of contact. Loss of contact can occur for each of the springs in the bedding. This takes place if $\Delta\zeta(x,x') < 0$. In this case, the stiffness, $\tilde{k}(x,x')$, is set to zero.

The choice of $\tilde{k}(x,x')$ in Equation (3.25) makes it possible for the bedding to correctly model the contact length, total contact load and deflection as predicted by the Hertzian theory for smooth surfaces if, in addition, the wheel radius is adjusted according to [23]

$$R_{\mathrm{W}}^{\mathrm{m}} = \frac{1}{2}R\,. \tag{3.26}$$

The radius R is the original radius of curvature of the conical wheel in the rolling direction, which is assumed to equal the transverse radius of curvature of the straight rail.

Introducing $2N_{\mathrm{C}}+1$ contact springs at the discrete positions

$$x'(\beta) = \beta\,\Delta x, \quad \beta = -N_{\mathrm{C}}, -N_{\mathrm{C}}+1, -N_{\mathrm{C}}+2, \ldots, N_{\mathrm{C}}\,, \tag{3.27}$$

the discrete versions of Equations (3.23)-(3.25) formulated at time step α corresponding to time $(\alpha-1)\Delta t$ and wheel centre position on the rail $(\alpha-1)\Delta x$ read

$$\Delta\zeta(\alpha,\beta) = \xi_3^{\mathrm{W}}(\alpha) - \xi_3^{\mathrm{R}}(\alpha) + r(\alpha,\beta) + z_{\mathrm{W}}(\alpha,\beta) \tag{3.28}$$

$$F_3(\alpha) = \sum_{\beta=-N_{\mathrm{C}}}^{N_{\mathrm{C}}} k(\alpha,\beta)\,\Delta\zeta(\alpha,\beta) \tag{3.29}$$

$$k(\alpha,\beta) = \begin{cases} \frac{1}{2}\frac{E}{[1-\nu^2]}\Delta x & \text{for} \quad \Delta\zeta(\alpha,\beta) \geq 0 \\ 0 & \text{for} \quad \Delta\zeta(\alpha,\beta) < 0 \end{cases} . \tag{3.30}$$

If $\xi_3^{\mathrm{W}}(\alpha)$ and $\xi_3^{\mathrm{R}}(\alpha)$ are known from Equations (3.8) and (3.17), respectively, (i.e. the first value of the Green's functions is set to zero), Equations (3.28)-(3.30) can be solved directly.

If the first value of the Green's functions is instead not set to zero (but the cross-coupling between vertical and tangential directions is neglected), Equations (3.7) and (3.16) read

$$\xi_3^{\mathrm{W}}(\alpha) = -g_{33}^{\mathrm{W}}(1)F_3(\alpha) - \xi_3^{\mathrm{W,old}}(\alpha) \tag{3.31}$$

$$\xi_3^{\mathrm{R}}(\alpha) = g_{33,v}^{\mathrm{R},v[\alpha-1]\Delta t}(1)F_3(\alpha) + \xi_3^{\mathrm{R,old}}(\alpha)\,. \tag{3.32}$$

Equations (3.28)-(3.30) together with Equations (3.31) and (3.32) then form a nonlinear equation system that is solved for $F_3(\alpha)$ by applying the Newton-Raphson method [45].

3.4.2 Elastic half-space model

The contact model based on the Winkler bedding presented in the previous section is computationally efficient and allows considering the contact filter effect in a natural way. Yet the model is only a two-dimensional one, and only the roughness in one line in the longitudinal x'-direction is taken into account. Additionally, the springs in the bedding deform independently of each other, while the points in a real continuum are coupled to each other. This requires reducing the wheel radius in order to simulate Hertz contact for smooth surfaces.

An alternative contact model that overcomes these shortcomings is based on the influence functions for the elastic half-space. It is assumed that wheel and rail can be locally approximated by elastic half-spaces. A potential contact area between wheel and rail is introduced and divided into N_p rectangular elements with side lengths Δx and Δy in the x'- and y'-directions, respectively. Kalker [43] investigated the case where the traction is piecewise constant over the mesh of rectangles and evaluated the corresponding influence coefficients A_{IiJj}. The coefficient A_{IiJj} gives the displacement in i-direction at the centre of element I due to a unit traction in j-direction in element J. These influence coefficients are also given in *Appendix B* in the form needed here, where it is assumed that wheel and rail are made of the same material. This assumption implies that the influence coefficients for coupling between the normal and tangential directions, i.e. A_{I1J3}, A_{I3J1}, A_{I2J3} and A_{I3J2}, are zero and the normal contact problem can be solved independently of the tangential contact problem.

In the following, the indices I and J denote an element in the set of elements forming the potential contact area P, i.e. $I \in P$ and $J \in P$, if not stated differently. The potential contact area consists of the contact area C and the exterior area E.

The local vertical displacement, u_{I3}, at the centre of one element I, which is defined as the displacement difference between rail and wheel

$$u_{I3} = u_{I3}^\mathrm{R} - u_{I3}^\mathrm{W} \,, \tag{3.33}$$

is influenced by the contact pressure throughout the contact area. It is obtained by superposing the contributions from each loaded element

$$u_{I3} = \sum_{J=1}^{N_\mathrm{p}} A_{I3J3}\, p_{J3} \,. \tag{3.34}$$

The total vertical contact force at the current time step, $F_3(\alpha)$, is obtained by summing the forces acting in the different elements

$$F_3(\alpha) = \sum_{I=1}^{N_\mathrm{p}} p_{I3} \Delta x \Delta y \,. \tag{3.35}$$

In addition to Equations (3.34) and (3.35) a kinematic constraint equation such as Equation (3.23) has to be introduced to describe the normal contact problem. As the points of the elastic half-space are coupled, in contrast to the springs in the Winkler bedding, the kinematic constraint Equation (3.23) has to be extended. The spring deflection, $\Delta\zeta$, is replaced by the local vertical displacement, u_3, and the distance, d, between the deformed bodies is introduced:

$$d_I = \xi_3^{\mathrm{R}}(\alpha) - \xi_3^{\mathrm{W}}(\alpha) + u_{I3} + z_I^{\mathrm{R}} - z_I^{\mathrm{W}} + r_I^{\mathrm{R}} - r_I^{\mathrm{W}} \,. \tag{3.36}$$

The distance, d_I, depends on the global vertical displacements of the rail, $\xi_3^{\mathrm{R}}(\alpha)$ and the wheel, $\xi_3^{\mathrm{W}}(\alpha)$, at the current time step, on the profiles of rail, z_I^{R}, and wheel, z_I^{W}, and on the roughness of rail, r_I^{R}, and wheel, r_I^{W}.

The contact conditions are formulated as

$$d_I \geq 0 \tag{3.37}$$

$$p_{I3} \geq 0 \,. \tag{3.38}$$

$$d_I p_{I3} = 0 \tag{3.39}$$

If contact occurs in a surface element, the distance is zero and the contact pressure is positive. If contact does not occur, the distance is positive and the pressure is zero. A negative value of the distance would mean that the two bodies penetrate into each other, which is physically impossible. A negative contact pressure would correspond to adhesion. Both penetration and adhesion are excluded by (3.37)-(3.39).

If the first value of the Green's functions is set to zero, $\xi_3^{\mathrm{R}}(\alpha)$ and $\xi_3^{\mathrm{W}}(\alpha)$ are known from Equations (3.8) and (3.17), respectively, and Equations (3.34) to (3.39) form a non-linear equation system that completely describes the normal contact problem at each time step α. An explicit equation for u_{I3} is only available for the elements that are in contact, where $d_I = 0$,

$$u_{I3} = -\xi_3^{\mathrm{R}}(\alpha) + \xi_3^{\mathrm{W}}(\alpha) - z_I^{\mathrm{R}} + z_I^{\mathrm{W}} - r_I^{\mathrm{R}} + r_I^{\mathrm{W}} \,, \tag{3.40}$$

and it is *a priori* unknown which elements are in contact.

An efficient iterative method to solve the normal contact problem is the algorithm proposed by Kalker [43]. He used a variational method and formulated the normal contact problem as a minimisation problem of an appropriate energy functional. To solve this problem, Kalker developed his active set algorithm NORM. The reason why this algorithm is called an active set algorithm is as follows. The solution, in the form of the contact pressure distribution, is subjected to the inequality constraint $p_{I3} \geq 0$. The elements in the potential contact area are divided into two sets.

The set of elements where the inequality constraint is active, i.e. $p_{I3} = 0$, is called the active set A. The remaining elements form the set N. In the normal contact problem, the active set thus comprises the elements which are *not* in contact, i.e. $A = E$ and $N = C$. Initially, an assumption is made about which elements belong to the active set. The active set is then updated step-by-step in the algorithm until the final solution is found. In detail, the active set algorithm used works as follows:

1. Initially, all elements are placed in the active set $A = E$ (which means $p_{I3} = 0$ in all elements).

2. The distance is calculated for all elements from Equation (3.36), which reduces to
$$d_I = \xi_3^{\mathrm{R}}(\alpha) - \xi_3^{\mathrm{W}}(\alpha) + z_I^{\mathrm{R}} - z_I^{\mathrm{W}} + r_I^{\mathrm{R}} - r_I^{\mathrm{W}} \,, \tag{3.41}$$
since $u_{I3} = 0$ (due to $p_{I3} = 0$ in all elements).

3. All points with a negative distance, $d_I < 0$, are removed from the set E and added to the set of contact elements C.

4. For the elements in the contact set C, the distance is zero and the surface displacement u_{I3} is calculated from Equation (3.40).

5. The contact pressure of all elements in contact is evaluated by setting up Equation (3.34) for all N_{c} elements in C:
$$u_{I3} = \sum_{J=1}^{N_c} A_{I3J3}\, p_{J3} \,, \quad I \in C \tag{3.42}$$
and solving the resulting linear equation system for the unknown p_{J3}.

6. All elements with negative pressure, $p_{I3} < 0$, are removed from C and added to E.

7. Steps 4-6 are repeated until no negative pressure is present anymore.

8. It has to be verified whether the solution found fulfils Equation (3.37). Therefore the displacement u_{I3} is calculated for all elements in E with Equation (3.34) and the distance is evaluated according to Equation (3.36).

9. If there are any points with negative distance, $d_I < 0$, these points are removed from the exterior area E and added to the contact area C.

10. Steps 4-9 are repeated until no negative distance is present anymore.

At the end of this iterative procedure, the size and shape of the contact zone and the contact pressure distribution are known.

If the first value of the Green's functions is not set to zero, i.e. Equations (3.8) and (3.17) are replaced by (3.31) and (3.32), respectively, the solution of the normal contact problem requires an additional iteration loop. In this case, the Newton-Raphson method [45] is used to solve the complete non-linear equation system for the contact force $F_3(\alpha)$. At each iteration step of the Newton-Raphson method, the active-set algorithm is applied to determine which points are in contact.

3.5 Inclusion of discrete irregularities

Discrete irregularities such as wheel flats and rail joints can easily be included in the interaction model. For this purpose, the surface profile corresponding to the irregularity, i.e. the wheel or rail profile, is updated in each time step in Equation (3.28) for the Winkler bedding model, or in Equation (3.36) for the elastic half-space model. In *Paper II* this is demonstrated for the case of a wheel flat.

3.6 Tangential contact model

The tangential contact model used in this work is based on Kalker's transient rolling contact model [43], which is implemented in his code CONTACT. The model is used with a constant friction coefficient as in the original implementation (*Section 3.6.1*), but has also been extended for use with a slip-velocity dependent friction coefficient (*Section 3.6.2*).

In frictional rolling contact, the contact area is divided into a stick area H and a slip area S. The tangential contact problem, which is solved after the normal contact problem at each time step, consists in determining which elements of the contact area are in stick and which are in slip, and calculating the local tangential displacements, $u_{I\tau}$, and tangential stresses, $p_{I\tau}$, at the surface.

3.6.1 Constant friction

In the following, all variables are evaluated at the current time step α, if not stated differently. The index τ takes the values 1 and 2, for the longitudinal and the lateral direction, respectively. The indices I and J denote an element in the set of elements forming the contact area C, i.e. $I \in C$ and $J \in C$, if not stated differently. The contact area consists of N_c elements.

The relation between the local tangential displacements in element I, $u_{I\tau}$, defined

as the displacement difference between rail and wheel

$$u_{I\tau} = u^{\mathrm{R}}_{I\tau} - u^{\mathrm{W}}_{I\tau}\,, \tag{3.43}$$

and the tangential stresses, $p_{I\tau}$, is given by

$$u_{I\tau} = \sum_{\alpha=1}^{2}\sum_{J=1}^{N_{\mathrm{c}}} A_{I\tau J\alpha}\, p_{J\alpha}\,, \tag{3.44}$$

where the $A_{I\tau J\alpha}$ are the influence coefficients for the elastic half-space given in *Appendix B*. The tangential forces, F_τ, are obtained by summing up the contributions from the different elements

$$F_\tau = \sum_{I=1}^{N_{\mathrm{c}}} p_{I\tau}\Delta x\Delta y\,. \tag{3.45}$$

A contact element belongs to the stick area, if the local shift, $S_{I\tau}$, vanishes:

$$S_{I\tau} = 0\,, \quad I \in H\,. \tag{3.46}$$

Otherwise the contact element belongs to the slip area. The local shift, defined as the relative displacement of two opposing particles of the wheel and the rail with respect to each other in one time step, is obtained as

$$S_{I\tau} = u_{I\tau}(\alpha) + W^*_\tau - u_{I\tau}(\alpha-1)\,, \quad I \in C\,. \tag{3.47}$$

The variable $u_{I\tau}(\alpha-1)$ represents the local displacement at the previous time step, which is known, and $u_{I\tau}(\alpha)-u_{I\tau}(\alpha-1)$ is called the deformation shift. In Kalker's formulation, $W_{I\tau}$ is the rigid shift calculated as

$$W_{I1} = [\xi - y'\phi]\,\Delta x \tag{3.48}$$
$$W_{I2} = [\eta + x'\phi]\,\Delta x\,, \tag{3.49}$$

where ξ, η and ϕ are the longitudinal, lateral and spin creepages. In the model proposed here, the contribution of the structural dynamics of wheel and track is added to the rigid shift:

$$W^*_{I1} = W_{I1} + \left[\xi^{\mathrm{R}}_1(\alpha) - \xi^{\mathrm{W}}_1(\alpha)\right] - \left[\xi^{\mathrm{R}}_1(\alpha-1) - \xi^{\mathrm{W}}_1(\alpha-1)\right] \tag{3.50}$$
$$W^*_{I2} = W_{I2} + \left[\xi^{\mathrm{R}}_2(\alpha) - \xi^{\mathrm{W}}_2(\alpha)\right] - \left[\xi^{\mathrm{R}}_2(\alpha-1) - \xi^{\mathrm{W}}_2(\alpha-1)\right]\,, \tag{3.51}$$

where the $\xi^{\mathrm{R}}_\tau(\alpha-1)$ and $\xi^{\mathrm{W}}_\tau(\alpha-1)$ are the tangential displacements of rail and wheel at the previous time step.

In the slip area, the following relations hold

$$\frac{p_{I\tau}}{\sqrt{p_{I1}^2 + p_{I2}^2}} = -\frac{S_{I\tau}}{\sqrt{S_{I1}^2 + S_{I2}^2}}, \quad I \in S \tag{3.52}$$

$$p_{I1}^2 + p_{I2}^2 = [\mu_{\mathrm{s}} p_{I3}]^2, \quad I \in S, \tag{3.53}$$

where μ_{s} is the constant friction coefficient. Equation (3.52) ensures that the slip occurs in the direction opposite to the tangential stress. Equation (3.53) states that the tangential stress in the slip zone is equal to the traction bound $\mu_{\mathrm{s}} p_{I3}$. In the stick area, the tangential stress is below the traction bound:

$$p_{I1}^2 + p_{I2}^2 < [\mu_{\mathrm{s}} p_{I3}]^2 . \tag{3.54}$$

Given that the $\xi_\tau^{\mathrm{R}}(\alpha)$ and $\xi_\tau^{\mathrm{W}}(\alpha)$ are known from Equations (3.8) and (3.17), Equations (3.44) to (3.54) form a set of non-linear equations that completely describes the tangential contact problem at each time step. The set of equations has to be solved iteratively, since the division of the contact zone into stick and slip zones is initially unknown. Even if the division into stick and slip were known, the equation system would still be a non-linear one.

An efficient algorithm to solve the non-linear set of equations is Kalker's active set algorithm TANG [43], also summarised in [106]. This algorithm, which has been used here, is very similar to the algorithm NORM described in *Section 3.4.2* and works as follows.

The set of contact elements is divided into two sets, the active set A and the set of remaining elements N. The active set comprises the elements where the constraint $p_{I1}^2 + p_{I2}^2 \leq [\mu_{\mathrm{s}} p_{I3}]^2$ is active. This is the case for the elements in the slip zone, where $p_{I1}^2 + p_{I2}^2 = [\mu_{\mathrm{s}} p_{I3}]^2$; i.e. $A = S$. Consequently, the set N consists of the elements in the stick zone; i.e. $N = H$. The steps in the algorithm – as used here – are

1. Initially all elements are placed in the stick zone H (i.e. the initial estimation of the active set is $A = \emptyset$).

2. For the current division of the contact zone into stick zone and slip zones, the non-linear system of equations consisting of Equations (3.46), (3.53) and

   $$p_{I1} S_{I2} - p_{I2} S_{I1} = 0, \quad I \in S \tag{3.55}$$

   is solved for the unknown tractions, making use of the definition of $S_{I\tau}$, Equation (3.47). Equation (3.55), which is taken from [106], replaces Equation (3.52) and allows in contrast to Equation (3.52) also that the slip occurs in the direction of the tangential traction (not only in the opposite direction).

3. All elements in H with tangential tractions exceeding the traction bound, i.e. $p_{I1}^2 + p_{I2}^2 > [\mu_s p_{I3}]^2$, are removed from H and added to S.

4. Steps 2 and 3 are repeated until there are no stick elements anymore that exceed the traction bound.

5. Now, it has to be verified whether the slip in all slip elements is opposite to the tangential tractions. All elements violating this condition are removed from S and added to H.

6. Steps 2 to 4 are repeated until the slip is opposite to the tangential tractions in all slip elements.

The Newton-Raphson method [45] is applied to solve the non-linear equation system in step 2. At the end of the iterative procedure, the division of the contact zone in stick and slip zones and the tangential stresses are known.

In the same manner as described for the normal contact problem, the solution of the tangential contact problem would require an additional exterior iteration loop, if the first value of the Green's functions were not set to zero. This has however not been implemented.

3.6.2 Slip-velocity dependent friction

The active set algorithm TANG presented in the previous section relies on the traction bound $\mu_I p_{I3}$ as input variable. In the case of a constant friction coefficient, the traction bound is known (after the normal contact problem has been solved). If a slip-velocity dependent friction coefficient is introduced, the friction coefficient in each element I depends on the slip velocity, which is an output variable of TANG. Consequently, the traction bound is unknown.

The methodology adopted to circumvent this problem follows essentially the procedure proposed by Croft [13]; see Figure 3.25. At each time step, an initial estimate of the traction bound is obtained by using the distribution of friction coefficients from the previous time step. The tangential contact algorithm TANG is then solved with this estimated distribution of traction bounds. Subsequently, the slip velocity distribution obtained as output is used in the friction characteristic in order to update the distribution of friction coefficients. Thereafter, TANG is solved again with the updated distribution of traction bounds, etc. The procedure continues until convergence is obtained for the contact variables. The experience with this method is that it is very reliable, but the convergence can be slow.

As an alternative to this 'direct' method of consecutive evaluations of TANG and the friction characteristic, Broyden's method [45] has been implemented to update

the distribution of the friction coefficients. In this method, belonging to the quasi-Newton methods, an approximate Jacobian is used, which is updated during the iteration process. The method looks for the root of the function

$$g(\boldsymbol{\mu}) = \boldsymbol{\mu} - f(\boldsymbol{s})\,, \tag{3.56}$$

where $\boldsymbol{\mu}$ and $\boldsymbol{s}$ are the vectors containing respectively the friction coefficients and absolute values of the slip velocity in all contact elements. The function $f(\boldsymbol{s})$ is the friction characteristic. The experience with Broyden's method is that it converges generally faster than the 'direct' method for this tangential contact problem, but fails more often.

In this work, both methods have been used complementarily – Broyden's method as first choice and, in the event of failure, the 'direct' method as backup.

The friction characteristic used in this thesis is taken from [13] and goes originally

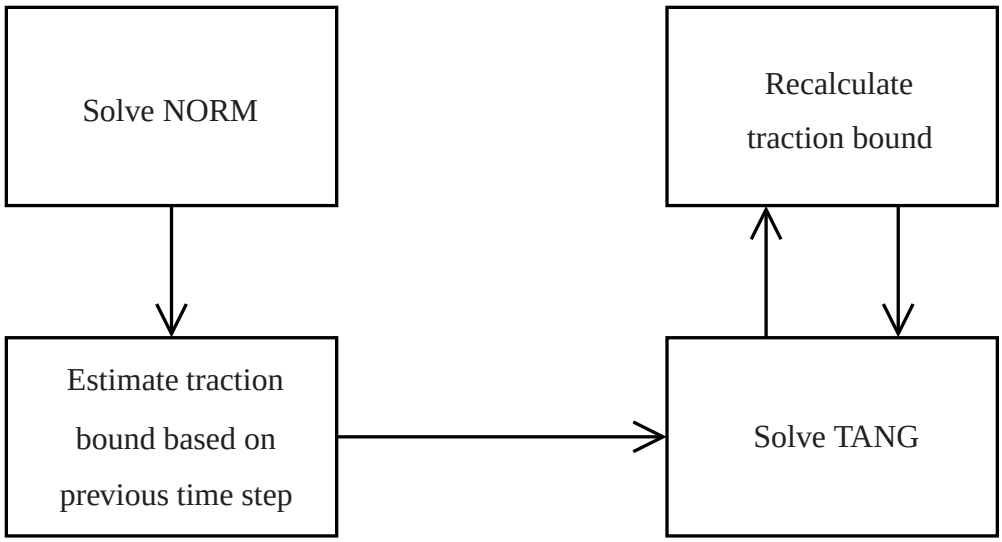

Figure 3.25: Iteration loop at each time step for the solution of the tangential contact problem in the case of a slip-velocity dependent friction coefficient (modified from [13]).

back to Kraft [52]. It reads

$$\mu_I(s_I) = \mu_\mathrm{s}\left[\frac{50}{100+s_I^2} + \frac{0.1}{0.2+|s_I|}\right]\,, \tag{3.57}$$

where μ_s is the static friction coefficient and $s_I = \sqrt{s_{I1}^2 + s_{I2}^2}$ is the absolute value of the slip velocity in the element I in $\mathrm{m/s}$. The components of the slip velocity are obtained from the local shift by [43]:

$$s_{I\tau} \approx S_{I\tau}/\Delta t\,, \quad \tau = 1,2\,. \tag{3.58}$$

The friction characteristic is depicted in Figure 3.26 for the choice $\mu_{\mathrm{s}} = 0.3$.

The extension of the contact algorithm to slip-velocity dependent friction is still a

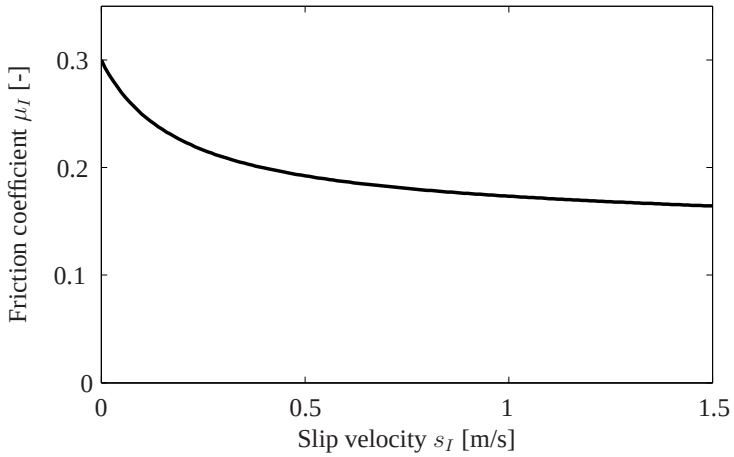

Figure 3.26: Friction characteristic according to Equation (3.57) for $\mu_{\mathrm{s}} = 0.3$.

subject of on-going research. While the tangential contact problem has a unique solution in the case of a constant friction coefficient [43], multiple solutions may exist in the case of a slip-velocity dependent friction coefficient [14]. This is further discussed in *Section 5.3.2*.

Chapter 4
Validation and verification of the wheel/rail interaction model

The wheel/rail interaction model proposed in this thesis has been validated partially against existing established models and existing measurement data. This chapter provides an overview of the different validations and verifications carried out.

The vertical interaction model has been validated for roughness excitation (*Section 4.1*) and excitation by wheel flats (*Section 4.2*). The implementation of the three-dimensional rolling contact model has been verified against the original implementation CONTACT (*Section 4.3*). The results of the interaction model in the case of frictional instabilities have, however, been verified qualitatively only by comparing with findings about curve squeal in the literature (*Section 4.4*).

A complete validation of the combined vertical and tangential wheel/rail interaction model against full-scale measurements, which would have been the ideal solution, was beyond the scope of this thesis. Full-scale validation tests for wheel/rail interaction models are not only an expensive undertaking, but also pose a challenge in terms of accessibility and measurability of certain important parameters. Two examples are the lateral wheel/rail contact position and the actual prevailing friction conditions. Good knowledge of these parameters is in practice difficult to achieve. This is especially problematic in the case of curve squeal, where rather small changes in parameters may lead to large variations in results. One possibility to overcome these difficulties would be to adopt a statistical approach for the validation of squeal models.

4.1 Comparison of the vertical interaction model to two existing interaction models

The vertical wheel/rail interaction model described in *Chapter 3* has been compared to two established time-domain models for wheel/rail interaction, notably the model by Croft [13] and DIFF [64]. The model DIFF itself has been validated against field measurements [63]. In contrast to the approach based on Green's functions used in the present model, the model by Croft and DIFF are both based on a

state-space approach. All three models were used with the same submodels. The wheel was represented by an unsprung mass (1-dof model) and the track model was the FE model with discrete supports originally implemented in DIFF, described in *Section 3.3.1*. To allow for the comparison, the contact model has been simplified to a Hertzian contact spring. The calculations have been carried out with a freight wheel of mass $M_{\mathrm{W}} = 488.5\,\mathrm{kg}$ passing at $v = 106\,\mathrm{km/h}$ along a track having soft rail pads and a sleeper spacing $L_{\mathrm{S}} = 0.6\,\mathrm{m}$. Three different roughness cases have been considered: smooth wheel and rail surfaces, a sinusoidal roughness and a broadband roughness. The data presented here have also been included in the thesis of Briony Croft [13] and are reused with permission. The author would like to acknowledge the contribution of Briony Croft, who took the initiative to make this comparison and provided the results from her model.

The results for smooth wheel and rail, where the excitation is solely due to paramet-

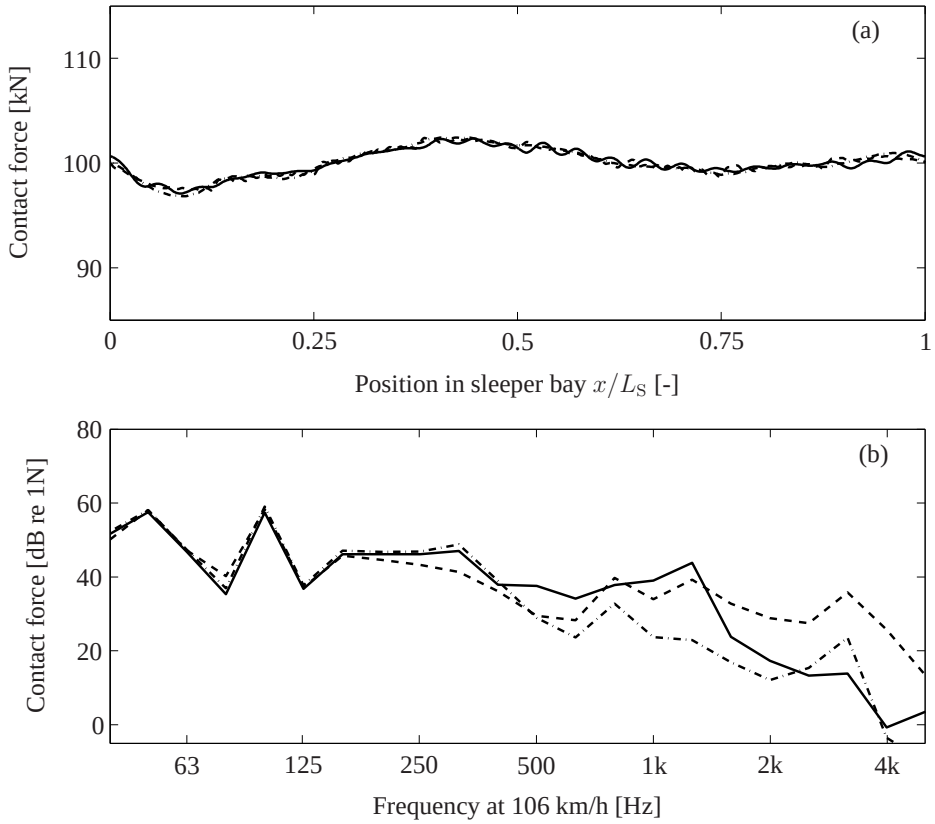

Figure 4.1: Comparison of the vertical contact force obtained for smooth wheel and rail: (a) time series in one sleeper bay, (b) one third-octave band spectra; —— model by Pieringer, – – – DIFF, – · – model by Croft.

ric excitation on the discretely supported rail, are presented in Figure 4.1. Shown

are the time series of the vertical contact force in one sleeper bay and the one-third octave band spectra of the contact force (calculated from the signal belonging to 31 sleeper bays). The three models give similar results at lower frequencies, especially at the peaks corresponding to the sleeper passing frequency at $49\,\mathrm{Hz}$ and twice the sleeper passing frequency. This is also reflected in the time series, which look rather similar. At higher frequencies, however, the spectra reveal bigger differences. It should be noted that minor differences between the models are emphasised in this case of parametric excitation, where the dynamic excitation is generally low.

In the second case, the models have been compared for a sinusoidal roughness with wavelength $40\,\mathrm{mm}$ and amplitude $10\,\mu\mathrm{m}$ (Figure 4.2). The time series show only small differences and, in the spectra, the agreement is very good at the main peak corresponding to the sinusoidal excitation and the two peaks corresponding to the sleeper-passing frequency. Nevertheless, as in the previous case of smooth wheel and rail surfaces, significant differences are observed at higher frequencies.

In the last case, a measured broadband roughness has been used, which has been pre-processed to account for the contact filter effect. Figure 4.3 shows excellent agreement between the models in both the time series and the force spectra for this case with a realistic roughness excitation.

A comparison of the vertical wheel/rail interaction model to DIFF, for different parameter values but otherwise similar to the one that has been presented here, is included in *Paper I*. Also in this comparison, good agreement has been found.

It is thus concluded that the vertical interaction model proposed in this thesis is valid for roughness excitation.

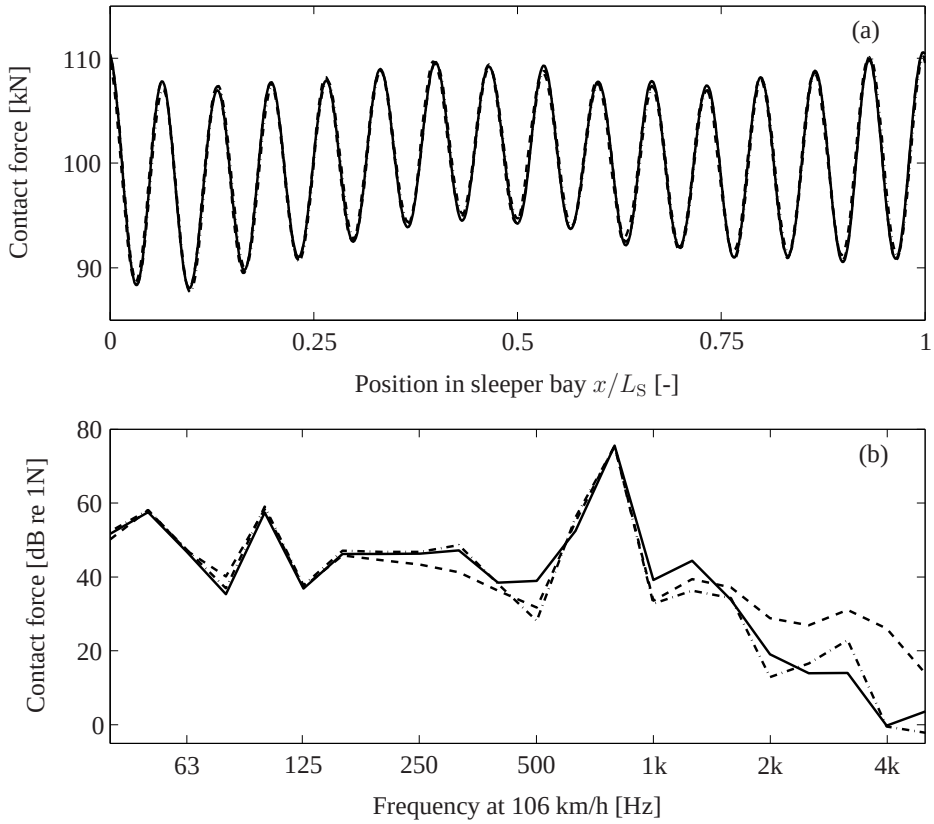

Figure 4.2: Comparison of the vertical contact force obtained for sinusoidal roughness: (a) time series in one sleeper bay, (b) one third-octave band spectra; —— model by Pieringer, – – – DIFF, – · – model by Croft.

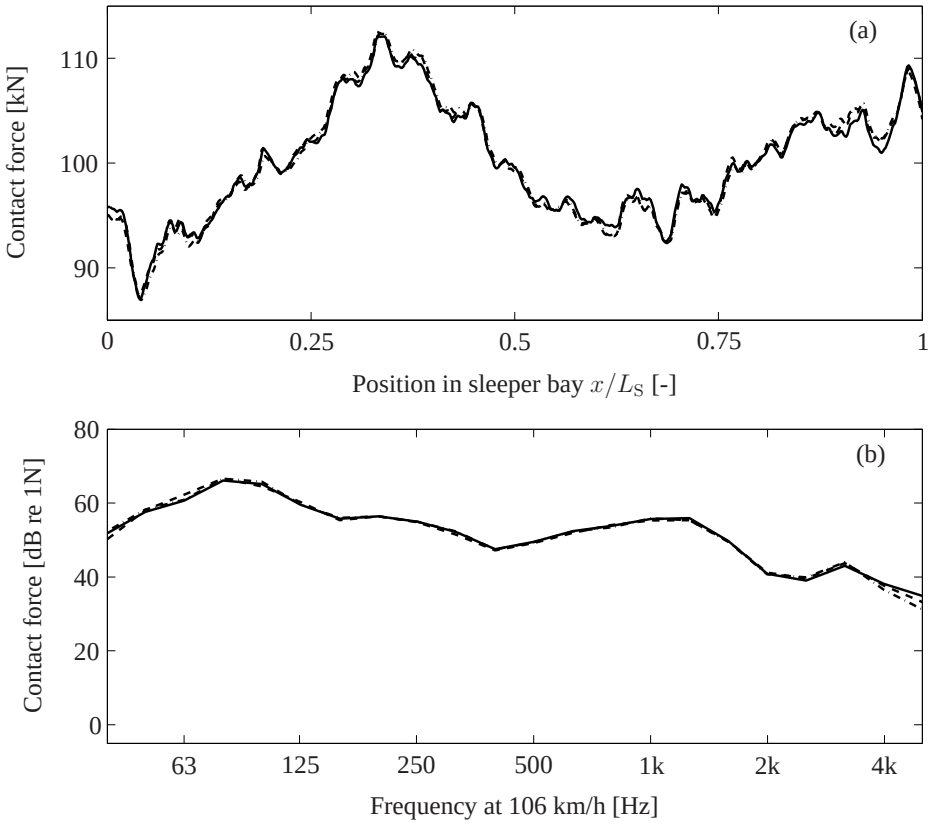

Figure 4.3: Comparison of the vertical contact force obtained for broadband roughness: (a) time series in one sleeper bay, (b) one third-octave band spectra; —— model by Pieringer, – – – DIFF, – · – model by Croft.

4.2 Impact forces due to wheel flats in comparison to measurement data

In *Paper II*, the vertical interaction model together with the 2D Winkler contact model has been applied to calculate impact forces caused by wheel flats. Simulation results have been compared with field measurements from reference [24] in terms of the maximum impact load during pass-by of the wheel flat. Considering the uncertainty in the track parameters characterising the test site, the level of agreement found between simulations and measurements is encouraging. Please refer to *Paper II* for a detailed discussion or *Section 5.2* for a summary of the results.

4.3 Quantitative verification of the contact models

The 3D model for vertical and tangential contact presented in *Sections 3.4.2* and *3.6.1* is based on Kalker's variational theory of transient rolling contact [43]. In order to verify the implementation, the model has been compared to Kalker's own implementation CONTACT [105].

As both models are implementations of the same theoretical formulation, very similar results are expected. Differences can arise from the different solvers used for the non-linear problem occurring in the tangential contact problem. CONTACT uses a specially designed Gauss-Seidel type solver [104], while a Newton-Raphson method is used in the present implementation. Furthermore, different tolerances and round-off practices can lead to slightly different results.

The two contact models have been compared for cylindrical wheel and rail profiles with wheel radius $R^{\mathrm{W}} = 0.39\,\mathrm{m}$ and rail head radius $R^{\mathrm{R}} = 0.30\,\mathrm{m}$, a friction coefficient $\mu = 0.3$ and a lateral creepage $\eta = 0.1\,\%$. Longitudinal creepage and spin creepage have been set to zero.

Figure 4.4 shows the divisions of the contact area into stick and slip zones obtained with both models, which are seen to be identical. The rolling direction is the positive x-direction. The corresponding distribution of the contact pressure and the total tangential stress depicted in Figure 4.5 are also very similar in both cases. As an example, Figure 4.6 presents the comparison on the lateral line $y' = 3\,\mathrm{mm}$. The relative difference between the distributions does not exceed $0.15\,\%$, which is also true for the complete contact area.

In *Paper V*, the contact models are compared for a case where real measured wheel and rail profiles have been used. Also in this case, very good agreement has been found. It is therefore concluded that the implementation of the 3D contact model presented in this thesis is correct.

The implementation of the 2D vertical contact model presented in *Section 3.4.1* has

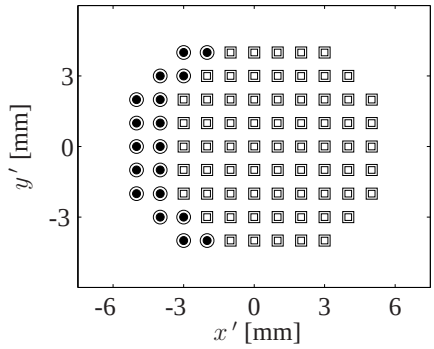

Figure 4.4: Division of the contact zone. Stick zone: □ CONTACT, ▫ implementation by Pieringer; Slip zone: ○ CONTACT, ● implementation by Pieringer.

been verified in [72]. In the case of smooth surfaces, the contact force-deflection characteristic agrees with Hertzian contact. The 2D contact models has also been compared to the 3D contact model as part of the vertical wheel/rail interaction model. When only parametric excitation caused by the space-dependent stiffness of the track is considered, the 2D and 3D contact models give very similar results in terms of the contact forces. In the case of roughness excitation, the 2D and 3D contact models give generally different results, since the 2D contact model does not consider roughness variations in lateral direction across the width of the contact, which are included in the 3D model.

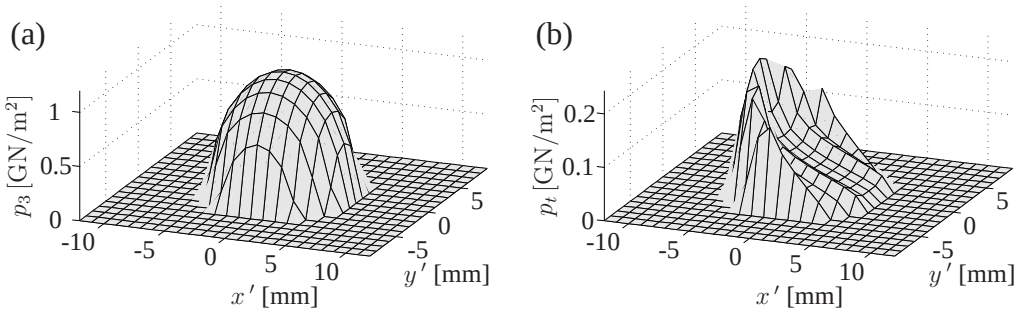

Figure 4.5: Distribution of (a) contact pressure p_3 and (b) total tangential stress $p_t = \sqrt{p_1^2 + p_2^2}$ in the contact zone.

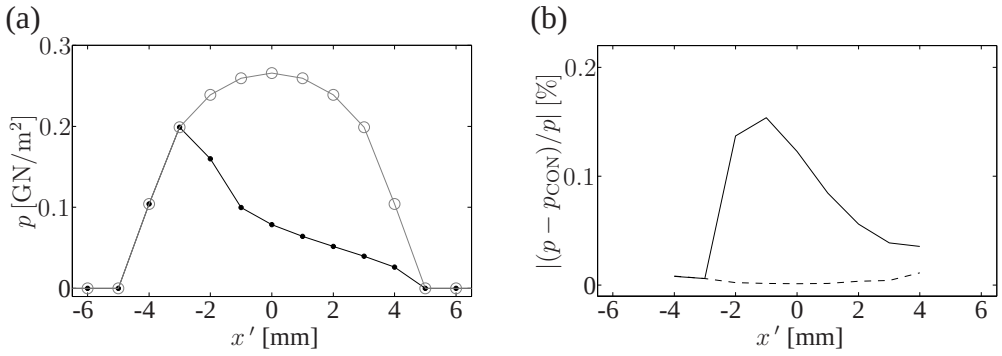

Figure 4.6: Comparison of tangential stress p_t and traction bound μp_3 on line $y' = 3\,\mathrm{mm}$: (a) absolute values of p_t (*in black*) and μp_3 (*in grey*); implementation by Pieringer (———); CONTACT (• /○); (b) relative difference in p_t (———) and μp_3 ($- - -$).

4.4 Qualitative verification of the simulation results including friction

The combined vertical and tangential wheel/rail interaction model used for the investigation of frictional instabilities has not yet been validated quantitatively.

The simulation results for a constant friction coefficient presented in *Paper V* and summarised in *Section 5.3.1* are, however, in good qualitative agreement with general observations about squeal noise and results reported in the literature. In all cases where stick/slip oscillations developed, the main frequency component was close to wheel resonances corresponding to axial modes of the wheel, which is typical for squeal [88]. The imposed lateral creepage, the friction coefficient and the lateral contact position were found to be key parameters in the occurrence of squeal. In particular, the conditions prevailing at the leading inner wheel of the bogie during curving (i.e. underradial position and contact towards the field side of the tread) were found to promote squeal. According to [88], squeal is usually excited most at the leading inner wheel. These findings demonstrate that the model gives reasonable results in the case of a constant friction coefficient.

The tangential contact model in the case of slip-velocity dependent friction is not yet considered fully reliable, though. A particular difficulty is the possible existence of multiple solutions of the contact problem; see *Section 5.3.2*.

Chapter 5

Applications of the wheel/rail interaction model

This chapter presents a selection of results and application areas of the wheel/rail interaction model that has been developed in *Chapter 3*. *Sections 5.1* and *5.2* discuss the application of the vertical interaction model for the evaluation of the contact filter effect and for the calculation of impact forces caused by wheel flats, respectively. In *Section 5.3*, which focuses on stick/slip oscillations induced by frictional instability, the combined vertical/tangential interaction model is applied. The results from a study of stick/slip in the case of constant friction are presented in *Section 5.3.1*. In *Section 5.3.2*, the case of a slip-velocity dependent friction law and the difficulties occurring with the contact model from *Section 3.6.2* are discussed.

5.1 Evaluation of the contact filter effect

Two studies about the contact filter effect are included in the appended papers. *Paper I* treats briefly the contact filter effect for passing over a rail with sinusoidal corrugation, while *Paper III* is solely devoted to the contact filter effect in the case of measured detailed roughness data.

In *Paper I*, simulations with the 2D contact model and in *Paper III*, simulations with both the 2D and the 3D contact models are compared with simulations using a non-linear Hertzian spring as contact model. The 2D and the 3D contact models consider the contact filter effect dynamically, since they incorporate the roughness in several discrete points in the rolling direction and account for a time-variant contact patch length. The models are therefore said to perform a dynamic roughness filtering. The 3D contact model considers, in addition, variations in roughness profile height in the lateral direction across the width of the contact. Using the single Hertzian spring, the contact filter effect has to be accounted for explicitly by calculating an equivalent roughness as a pre-processing step, which is called quasi-static roughness filtering. Three such calculation methods are considered:

- An equivalent roughness is calculated by means of the Winkler bedding depicted in Figure 3.24. Details about the procedure can be found in reference [23].
- An equivalent roughness is obtained by averaging over the nominal contact patch length (corresponding to the static preload and smooth surfaces).
- No equivalent roughness is calculated, and the simulations are carried out with the original roughness excitation (i.e. the contact filter effect is not taken into account).

In both studies of the contact filter effect, the discretely supported FE model of the track from *Section 3.3.1* is used. The wheel models in *Paper I* and *Paper III* are respectively the 1-dof model and the 2-dof model from *Section 3.2.1*. Typical calculation times for the simulations on a standard PC are a few minutes in the case of the 2D contact model or the Hertzian spring and a few tens of minutes in the case of the 3D contact model.

In *Paper I*, the idealised corrugation is assumed to consist of only one sine curve with corrugation wavelength λ and amplitude A. Simulations have been carried out for a wide range of wavelengths and two different amplitudes. The results have been analysed in terms of the maximum vertical contact force during pass-by as function of the corrugation wavelength. The contact filter effect in the simulation results is clearly noticeable for corrugation wavelengths that are up to three to four times the nominal contact patch length (the latter being $10.7\,\mathrm{mm}$). This means that considerable errors are made if the contact filter effect is not considered. However, not much difference is observed between the different methods of roughness filtering in the investigated wavelength range down to somewhat smaller than the nominal contact patch length. The simple averaging filtering performs surprisingly well. The maximum difference between averaging filtering and dynamic filtering reaches slightly over $3\,\mathrm{dB}$ at short wavelengths. No significant difference is observed between quasi-static filtering with the Winkler bedding and dynamic filtering. The results could look substantially different at corrugation wavelengths shorter than the ones considered.

In *Paper III*, the contact filter effect is evaluated for excitation by detailed roughness data measured in several parallel longitudinal lines in the running band. The roughness data comprise one set of rail roughness measured at a site showing severe corrugation [101] and three sets of wheel roughness data originating from one wheel with cast-iron block brakes and two wheels with sinter block brakes [99]. The calculations are carried out using one data set at a time, i.e. the wheel or the rail is considered to be smooth. The 3D contact model considers the complete roughness profile, while the 2D model and the Hertzian spring only operate on one longitudinal roughness line. It is not evident which roughness line should be chosen.

As examples of the results of the dynamic calculations in *Paper III*, the results for excitation by the roughness from one of the wheels with sinter block brakes are presented in Figure 5.1. For the other roughness sets please refer to *Paper III*. Fig-

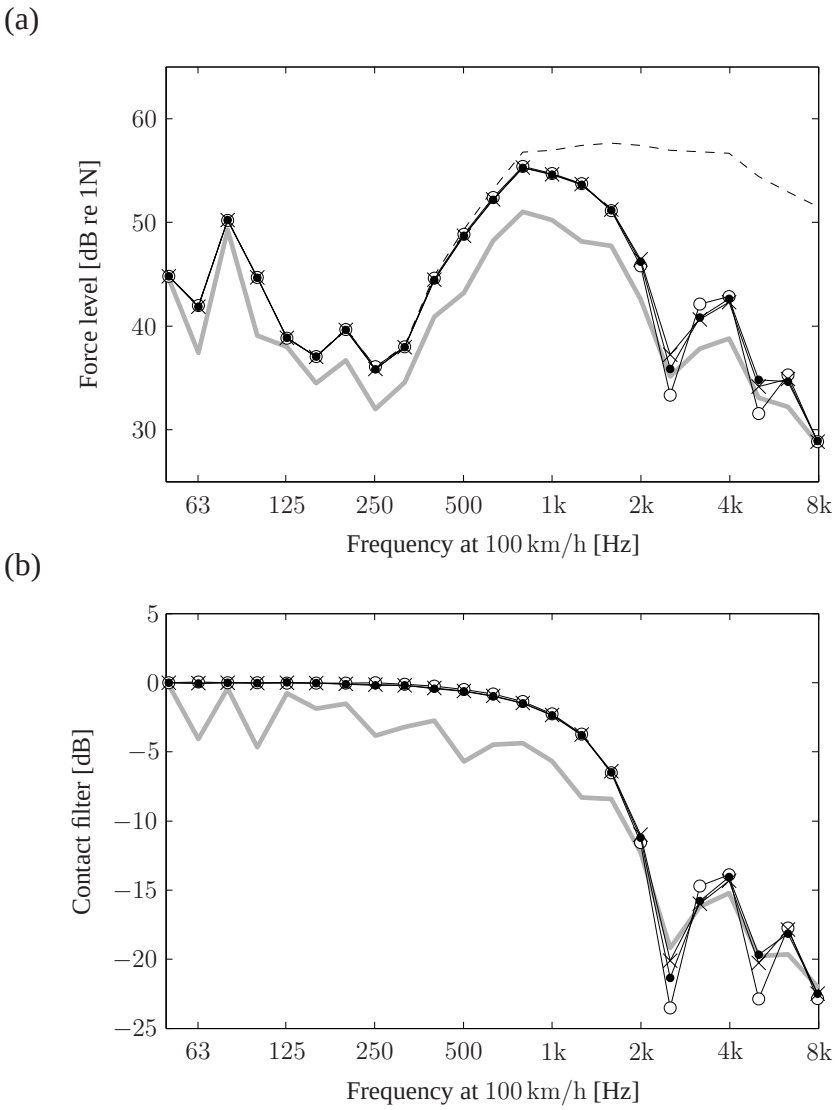

Figure 5.1: Dynamic wheel/rail interaction excited by roughness measured on a wheel with sinter block brakes (wheel 2 in Paper III): (a) average one third-octave band spectra of the vertical contact force and (b) average contact filter effect calculated from runs with seven different longitudinal roughness lines; contact model: ——— (*thick grey line*) 3D contact model, —×— 2D contact model, —●— Hertzian spring with roughness pre-filtering by the Winkler bedding, —○— Hertzian spring with roughness pre-filtering by averaging, – – – Hertzian spring with no roughness pre-filtering.

ure 5.1(a) shows the third-octave band spectrum of the vertical contact force. In the case of the 2D contact model and the Hertzian contact model, the spectrum shown is an average of the seven spectra obtained from separate runs with seven different roughness lines. Figure 5.1(b) presents the contact filter effect obtained for the different contact models. This is calculated by taking the level difference in dB values between each of the spectra and the spectrum obtained in the case of the Hertzian spring with no roughness pre-filtering. In the same manner as before, the calculations have been carried out for seven different roughness lines separately. The filter curves shown are the average of the filter curves obtained for each run.

In the excitation case shown in Figure 5.1 and the other three cases treated in *Paper III*, the models performing filtering on one roughness line – either dynamically or by pre-filtering – are found to give very similar results up to about $2\,\mathrm{kHz}$ (i.e. wavelengths of over $14\,\mathrm{mm}$ at the chosen train speed of $100\,\mathrm{km/h}$). These results are in good agreement with the findings in *Paper I*. At higher frequencies, dynamic filtering and quasi-static filtering with the Winkler bedding are still very similar in three out of the four excitation cases in *Paper III*. The Hertzian model with pre-filtering by averaging gives, however, significantly different results at higher frequencies, the biggest differences occurring for the corrugated rail (up to $9\,\mathrm{dB}$ mean difference).

The main findings in *Paper III* concern the differences obtained between the 2D and 3D contact models. The 3D contact model gives, as a general tendency, a contact force level several dB lower than the 2D model. The analysis in *Paper III* shows that the differences obtained depend on the degree of correlation of the roughness across the width of the contact patch. At frequencies where the correlation is high, both models give similar results. With decreasing correlation, the differences increase. A parameter based on the coherence of several parallel roughness lines is proposed in *Paper III* to assess the correlation across the width of the contact patch. In the case shown in Figure 5.1, the roughness correlation is low in the whole frequency range and the 3D contact model is seen to result in lower contact forces than the 2D model in a wide range. At higher frequencies (above $2\,\mathrm{kHz}$ for the chosen model parameters), the differences in contact force level obtained with the 3D and 2D models are increased or diminished by distinct dips in the 2D filter. These are an inherent property of the 2D filter operating on an (approximately constant) contact length. The simulation results in *Paper III* show, too, that the differences in contact force level obtained with the 3D and 2D models vary significantly with the roughness line chosen in the 2D model. Using an average of roughness lines as input in the 2D model results in sufficient accuracy in the 2D model in only one out of the four cases. The 3D model still gives satisfactory results, when a lateral roughness resolution of $4\,\mathrm{mm}$ (instead of originally $2\,\mathrm{mm}$) is used. The former corresponds to measuring the roughness on five parallel lines.

The primary conclusion from *Paper III* is thus that the common practice to measure

only one longitudinal roughness line that is taken as typical of the running band is generally not sufficient, since significant errors may occur when the 3D roughness distribution is represented by only one roughness line. Detailed roughness measurements are also necessary in order to be able to estimate the error occurring when using the 2D model instead of the 3D model.

5.2 Calculation of impact forces caused by wheel flats

In *Paper II*, the vertical interaction model together with the 2D contact model is applied to calculate impact forces caused by wheel flats. The track is represented by the FE model with discrete supports, and the wheel model used is the 1-dof model. The flat is introduced on a rotating wheel whose profile in the contact zone is updated in every time step. Two kinds of wheel-flat geometries are considered: the newly formed wheel flat with sharp edges as occurring right after formation, and the rounded wheel flat which rapidly develops from the newly formed flat as a result of wheel tread wear and plastic deformation.

To demonstrate the functioning of the modelling approach, simulation results are compared with field measurements from reference [40] in terms of the maximum impact load; see Figure 5.2. In the field test, the impact load caused by a rounded wheel flat with depth $d = 0.9\,\mathrm{mm}$ and length $l = 0.1\,\mathrm{m}$ on a freight train with axle load $24\,\mathrm{t}$ ($P = 117.7\,\mathrm{kN}$) was measured for train speeds between $30\,\mathrm{km/h}$ and $100\,\mathrm{km/h}$. As the receptance of the loaded track in the frequency range of interest could not be measured during the field tests, Nielsen et al. determined rail pad and ballast parameters through model calibration [65]. These model parameters (listed in *Paper II*) are also used in the present simulations. As the calculated impact force varies depending on where the wheel flat hits the rail in relation to the sleeper location, simulations with 40 different initial angular wheel positions are run in order to cover the whole range of maximum impact force magnitudes. Considering the uncertainty in the track parameters, the level of agreement between simulations and measurements seen in Figure 5.2 is encouraging.

In addition to the maximum forces used for comparison to the field measurements, Figure 5.2 also shows the minimum contact force, allowing identification of loss of contact between wheel and rail. Beside the $0.9\,\mathrm{mm}$ deep rounded wheel flat, also a $0.9\,\mathrm{mm}$ deep new wheel flat is considered. A more detailed description and analysis of Figure 5.2, as well as additional simulation results, can be found in *Paper II*. Beside train speed and wheel-flat type, the wheel-flat depth is also identified as an important parameter for the magnitude of impact forces caused by wheel flats. Especially at higher train speeds, the impact position of the wheel on the rail in relation to the sleeper location has a significant influence, too.

A minor disadvantage of the 2D contact model, in the context of wheel flats (or

other wheel irregularities), is that this contact model requires a reduced wheel radius in order to model Hertzian contact for smooth surfaces. Consequently, the wheel flat has to be mapped onto the reduced wheel, implying that it is not possible to represent correctly both wheel-flat depth and length. Though this has not been done yet, it seems promising to apply the 3D contact model to simulate impact forces caused by wheel flats. It would be possible not only to keep the original wheel radius, but also to include the complete 3D geometry of the wheel flat. This requires, however, that measurement data of the 3D wheel-flat geometry with sufficient resolution are available.

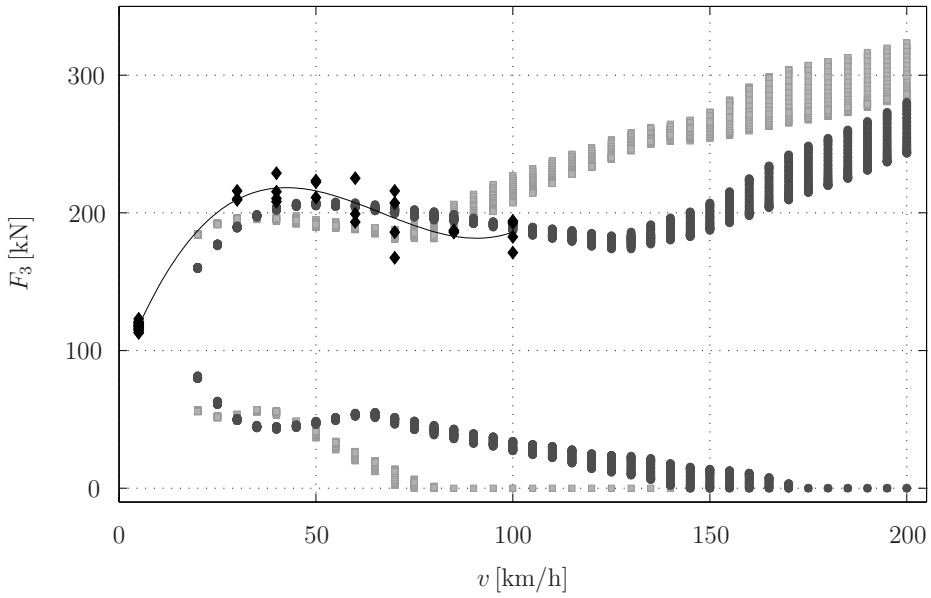

Figure 5.2: Measured maximum impact forces (◇, black) due to a $0.9\,\mathrm{mm}$ deep rounded wheel flat in comparison to calculated maximum and minimum impact forces (○, dark grey). Shown are also a third-degree polynomial fitted to the measured data (——) and calculated results for a $0.9\,\mathrm{mm}$ deep new wheel flat (□, light grey).

5.3 Frictional instability in wheel/rail contact

In this section, the combined vertical and tangential wheel/rail interaction model is applied to calculate stick/slip oscillations induced by frictional instability. The submodels used are the FE model of the wheel from *Section 3.2.2*, the WFE model of the track from *Section 3.3.2* and the 3D contact models for normal and tangential contact presented in *Sections 3.4.2 and 3.6*. Although the detailed FE models

used for wheel and track include the longitudinal, lateral and vertical dynamics, the simulations presented in this section are limited to vertical and lateral dynamics of wheel and track. The wheel/rail contact, however, is treated as fully three-dimensional. Typical calculation times for the simulations are a few days on a standard PC.

5.3.1 Investigation of stick/slip oscillations in the case of constant friction

Most researchers working with the modelling of curve squeal introduce the negative slope of the friction characteristic as source of the instability, while others have found that squeal can also occur in the case of constant friction due to the coupling between normal and tangential dynamics; see *Section 2.4*. As a contribution to this discussion on the squeal mechanism, an investigation has been carried out in *Paper V* into stick/slip oscillations in the case of constant friction, which is summarised in the following.

Real measured wheel and rail profiles have been used in the investigation. The wheel profile is a S1002 profile worn over $169\,000\,\mathrm{km}$. The rail profile is a BV50 profile with inclination 1:40 measured at a curve in the network of Stockholm metro, where severe corrugation and squeal occur [101]. For these profiles, the contact points on wheel and rail have been determined as a function of the relative lateral displacement Δy^{WR} of the wheelset on the rail with a pre-processor of the commercial vehicle-track interaction software GENSYS [18]. The author acknowledges the assistance of Peter Torstensson (CHARMEC, Chalmers University of Technology), who provided the measured profiles and carried out the GENSYS calculations.

A parameter study has been carried out, where the influence of the friction coefficient μ_{s}, the imposed lateral creepage η and the relative lateral displacement of the wheelset on the rail Δy^{WR} on the dynamic wheel/rail interaction has been investigated. A total of 108 different parameter combinations has been tested.

The most important result from the parameter study is that stick/slip during curving (and consequently curve squeal) is indeed possible not only in the case of a falling friction coefficient, but also in the case of constant friction. In 14 of the investigated cases, pronounced stick/slip oscillations developed in the first $3.5\,\mathrm{s}$ of the simulation. The occurrence of these stick/slip oscillations is attributed to the coupling between vertical and tangential dynamics.

An example of the stick/slip oscillations from *Paper V* is shown in Figure 5.3 in terms of the lateral contact force. In this simulation, denoted simulation I in *Paper V*, the parameter values $\mu_{\mathrm{s}} = 0.3$, $\eta = -1\%$ and $\Delta y^{\mathrm{WR}} = -15\,\mathrm{mm}$ have been used. A negative value of the lateral creepage corresponds to an underradial

position of the wheelset in the curve, where the wheelset has an angle of attack against the track. For the chosen relative lateral displacement Δy^{WR}, the contact on the wheel tread occurs at the field side of the tread; see *Paper V*. Details of the stick/slip cycle are depicted in Figure 5.4. During most of the cycle the contact area is in full slip and the lateral contact force F_2 coincides with the traction limit μF_3. Only during a short phase in each cycle, partial stick occurs and the lateral force takes a value below the traction bound.

The results of the complete parameter study from *Paper V* are depicted in Figure 5.5(a) for the variation of the friction coefficient and the lateral creepage, and in Figure 5.5(b) for the variation of the relative lateral displacement of the wheelset on the rail. The relative stability of the simulations is characterised by the measure L_{F_2} which is based on the rms-value of the lateral contact force signal and gives low values in cases where stick/slip does not occur; see *Paper V*. All three investigated parameters are seen to have a strong influence on the occurrence of stick/slip:

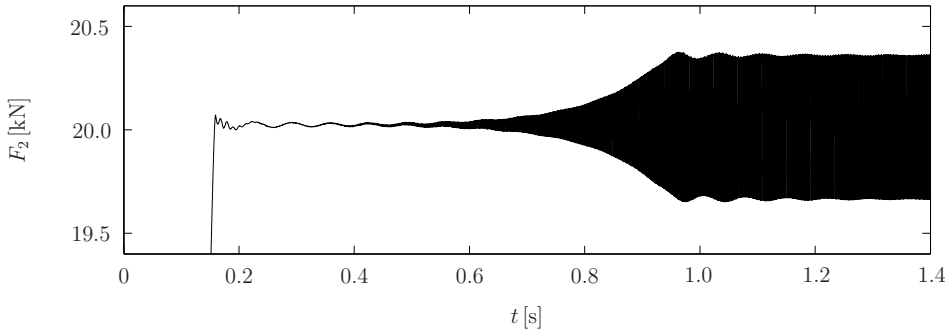

Figure 5.3: Stick/slip in the case of constant friction: time series of the lateral contact force F_2 (corresponding to Simulation I in *Paper V*).

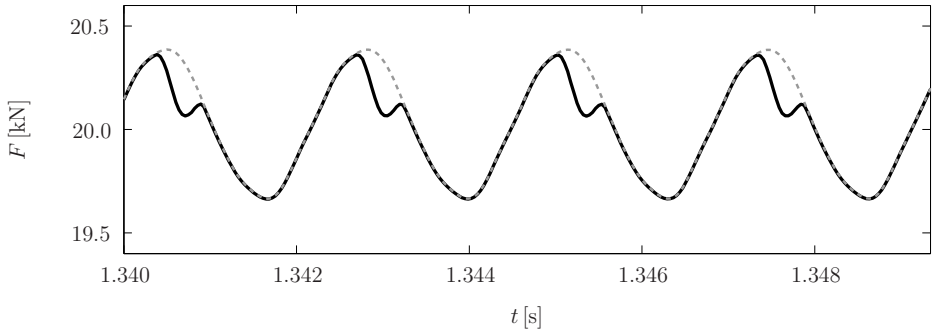

Figure 5.4: Stick/slip in the case of constant friction: zoom on time series of the contact forces (corresponding to Simulation I in *Paper V*); —— lateral force F_2, $---$ (*grey*) traction bound μF_3.

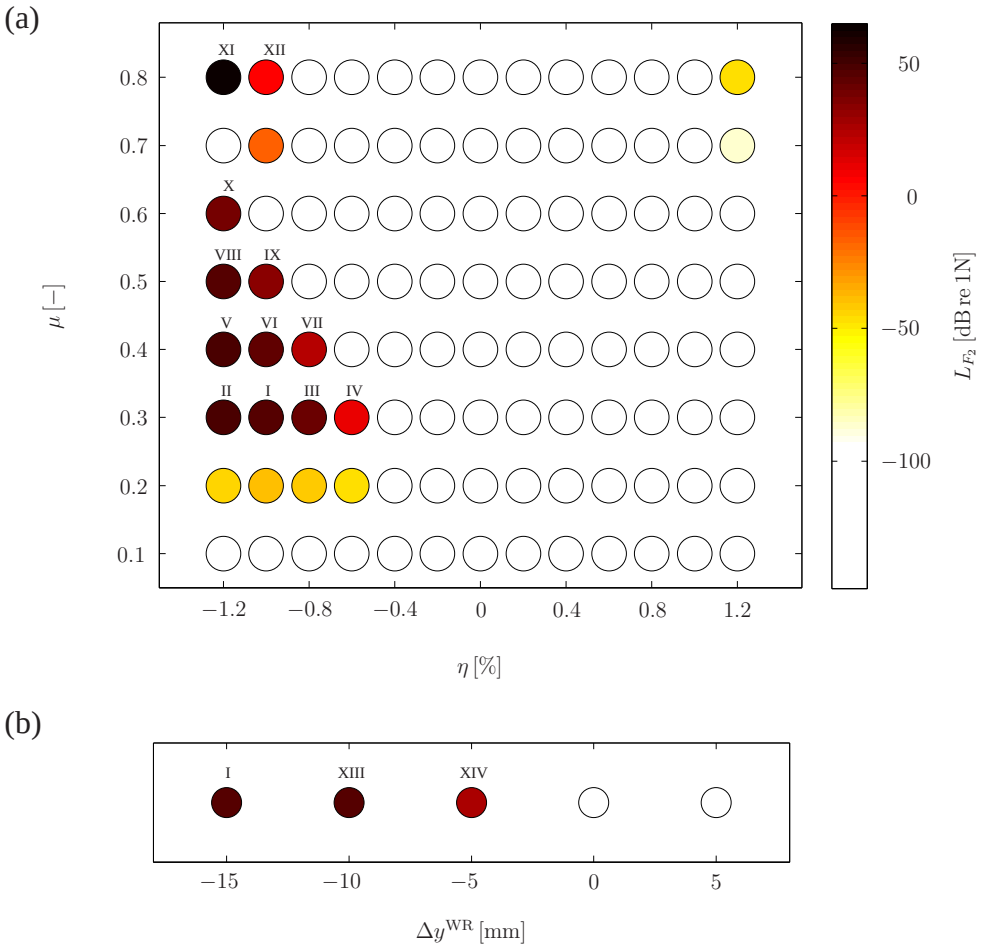

Figure 5.5: Results of the dynamic simulations as function of (a) the imposed lateral creepage η and the friction coefficient μ and (b) the relative lateral displacement Δy^{WR} of the wheelset on the rail: force level L_{F_2} calculated according to Equation (25) in *Paper V*; simulations with $L_{F_2} > 0\,\mathrm{dB}$ are denoted by Roman numerals. The same colour bar applies in both subfigures.

Significant stick/slip developed only for negative values of the lateral creepage (i.e. underradial positions of the wheelset) and not below a threshold of (the absolute value of) the lateral creepage of 0.6%. Furthermore, pronounced stick/slip oscillations did not occur for low friction coefficients (below 0.3) and occurred only for contact positions on the wheel tread towards the field side of the wheel. Another observation from the parameter study is that small changes in the parameters can lead to a sudden appearance (or disappearance) of stick/slip oscillations. In all cases where stick/slip developed, the main frequency component of the oscillation was close to wheel resonances corresponding to axial modes of the wheel with zero nodal circles.

As already discussed in *Section 4.4*, the results of the parameter study are in good qualitative agreement with published findings about curve squeal.

5.3.2 Grid-size dependent high-frequency oscillations and non-uniqueness of solution in the case of slip-velocity dependent friction

Combining the tangential contact algorithm with a slip-velocity dependent friction coefficient as described in *Section 3.6.2* entails two different problems. First, grid-size dependent high-frequency oscillations are observed in the quasi-static case, which are not yet fully explained. Second, the uniqueness of the solution given in the case of a constant friction law [43], is not guaranteed anymore for a slip-velocity dependent friction coefficient. Both phenomena are exemplified in the following.

Under quasi-static conditions, i.e. when wheel and track dynamics are not included, the interaction model converges to a steady-state solution for an imposed constant creepage and a constant normal force if the friction coefficient is constant. In the case of a falling friction curve, high-frequency stick/slip oscillations may occur under otherwise identical circumstances. Figure 5.6, which shows the time series of the lateral contact force, demonstrates that the occurrence and amplitude of these oscillations depend on the element length in the rolling direction Δx (hence on the time step $\Delta t = \Delta x / v$ with v being the train speed). The simulations have been carried out for the falling friction curve (3.57) together with a static friction coefficient $\mu_{\mathrm{S}} = 0.3$, a lateral creepage $\eta = 0.5\%$, a train speed $v = 50\,\mathrm{km/h}$ and a static preload $P = 65\,\mathrm{kN}$. Longitudinal and spin creepage have been set to zero and cylindrical wheel/rail profiles have been used. The oscillations in Figure 5.6 are increasingly unstable for decreasing Δx. The fundamental frequency component of the oscillations occurs at a divisor of the sampling frequency. Different divisors are found for different Δx.

Figure 5.7 shows the time series of the tangential stress and the local slip on the centre line of the contact in rolling direction for the case $\Delta x = 0.25\,\mathrm{mm}$ from

Figure 5.6. The steps shown correspond to the time steps marked in Figure 5.6. A small slip zone occurs at the trailing edge of the contact in step 1. Subsequently, this slip zone is seen to grow gradually. At the same time, tangential stress builds up until a "collapse" occurs between time steps 6 and 7. The system jumps to slip in the complete contact zone and the tangential stress is relieved. Due to the decreased stress, the system goes back to mainly stick in the next step and the cycle recommences.

The problem of multiple solutions can also be exemplified by means of Figure 5.7. To calculate the solution in each time step of Figure 5.7, the distribution of slip velocities of the previous time step has been taken as initial estimate in the iterative method. The solution obtained by this means in step 6 showing a decreased slip zone does not seem to fit into the stick/slip cycle. When a full slip solution is taken as initial estimate instead, another solution with a larger slip zone is found; see Figure 5.8.

The same phenomena have also been reported by Croft et al. [14]. They compared two independent implementations of the same tangential contact model also used

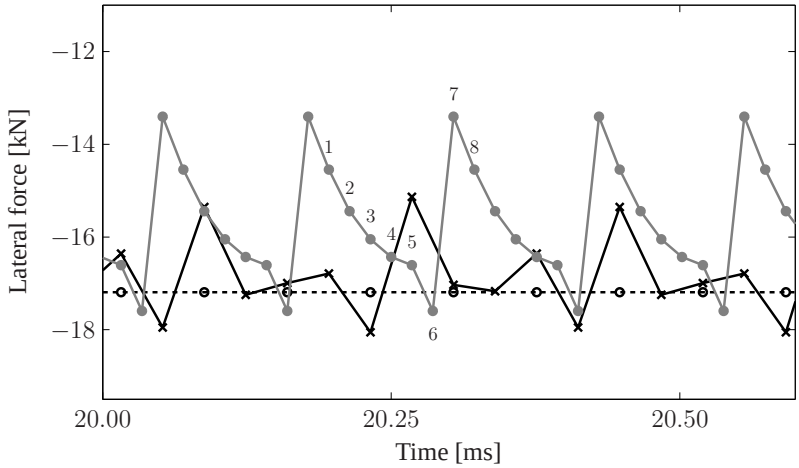

Figure 5.6: High-frequency oscillations under quasi-static conditions for different element lengths Δx: $-\circ-$ $1\,\mathrm{mm}$; $-\times-$ $0.5\,\mathrm{mm}$; $-\bullet-$ $0.25\,\mathrm{mm}$. Selected time steps are denoted by Arabic numerals.

in this work: the time-stepping model by Croft [13] and a modified version of CONTACT [105] by Vollebregt. In their investigation carried out for a constant longitudinal creepage, they observed the same type of stick/slip oscillations at the trailing edge of the contact. The oscillations were found to be increasingly unstable with increasing creep, increasing slope of the falling friction curve, and decreasing element length in rolling direction. The dependence of the amplitude of the oscillations on the element length is explained by the fact that the "collapse" occurs in

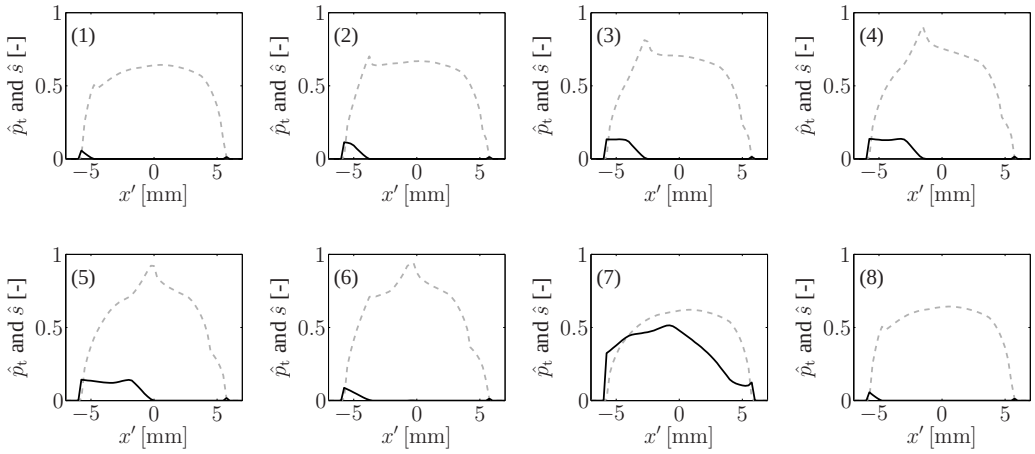

Figure 5.7: Time history corresponding to the time steps numbered in Figure 5.6 for the case $\Delta x = 0.25\,\mathrm{mm}$: − − − (*in grey*) normalised tangential stress $|p_\mathrm{t}|/p_\mathrm{ref}$, —— normalised local slip $|s|/s_\mathrm{ref}$ on line $y' = 0$.

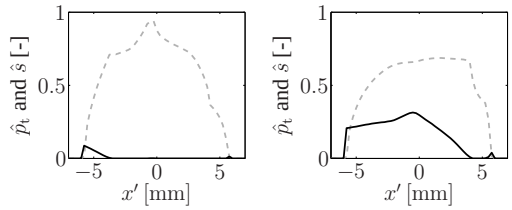

Figure 5.8: Low and high slip solution in time step 6 of Figure 5.7: − − − (*in grey*) normalised tangential stress $|p_\mathrm{t}|/p_\mathrm{ref}$, —— normalised local slip $|s|/s_\mathrm{ref}$ on line $y' = 0$.

one time step. When the time step is reduced, the change of the system occurs in a shorter time period, which entails a higher slip velocity [14]. Croft et al. [14] reported also about the existence of multiple solutions. One principal difference between the results presented in [14] and the results in Figure 5.7 (deliberately presented in the same types of plots as in [14]) concerns the tangential stress distribution in the stick zone. While Croft et al. found distinct (so far unexplained) peaks in the stick zone, this phenomenon is not seen in Figure 5.7. It should however be noted that Croft et al. carried out the simulations with different parameters (e.g. longitudinal creepage instead of lateral creepage) and that their analyses is two-dimensional in contrast to the three-dimensional version of the model used here.

The occurrence of the grid-size dependent stick/slip oscillations in two additional independent implementations of the contact model suggests that this phenomenon

is a consequence of the modelling approach, and rules out programming errors as reason for their occurrence. E.H.A. Vollebregt relates the phenomenon to the quasi-static assumption made in CONTACT [43] in combination with the falling friction law employed (personal communication, February 2, 2011). A possible solution could thus be to include the contact dynamics in the model. This is however beyond the scope of this thesis. A correct handling of the problem of multiple solutions would require us to identify all solutions and to find a way to select the "physical" one.

More research is needed on the handling of the described phenomena in the dynamic algorithm and their implications. Nevertheless, results from the combined vertical/tangential interaction model including the wheel and track dynamics are also presented in the following, in order to demonstrate the behaviour of the model in the case of a slip velocity-dependent friction coefficient.

In particular, the quasi-static simulation from Figure 5.6 with $\Delta x = 0.5\,\mathrm{mm}$ has been repeated with the wheel and track dynamics included. The main frequency component of the lateral contact force occurs then at $5235\,\mathrm{Hz}$, see Figure 5.9, which corresponds to the (7,0,a) axial wheel mode at $5216\,\mathrm{Hz}$. When this mode is removed from the wheel receptance, the stick/slip oscillation occurs at another frequency; see Figure 5.10. By contrast, the removal of the second wheel mode close to the main frequency component, the circumferential (2,c) mode at $5228\,\mathrm{Hz}$, did not have a significant influence on the spectrum. Figure 5.9 shows also the spectrum of the lateral contact force in the quasi-static case. In this case, peaks occur at $F_\mathrm{s}/10$ and higher harmonics of this frequency, where $F_\mathrm{s} = 27.8\,\mathrm{kHz}$ is the sampling frequency. These peaks are not present anymore in the dynamic case.

Similar results are also presented in *Paper IV* for the train speed $v = 100\,\mathrm{km/h}$. Additionally, the effect of roughness excitation on the stick/slip oscillations has been investigated in *Paper IV*. The inclusion of roughness led to generally higher contact force levels in comparison to the case with smooth surfaces, but left unchanged the main peaks in the spectrum corresponding to the (8,0,a) axial mode of the wheel and higher harmonics.

It is to be assumed that the results from the dynamic simulations shown in this section and in *Paper IV* are equally grid-size dependent as the results from the quasi-static simulations. Furthermore, it cannot be excluded that the existence of multiple solutions (not specially accounted for in the algorithm) has an influence on the outcome of the dynamic simulations.

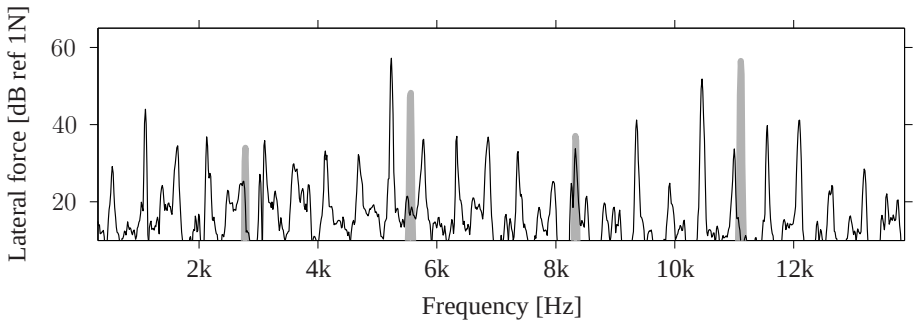

Figure 5.9: Power spectrum of the lateral contact force in the case of falling friction, $\eta = 0.5\%$, $v = 50\,\mathrm{km/h}$: dynamic wheel/rail interaction (——) in comparison to the corresponding quasi-static case (——, *in grey*).

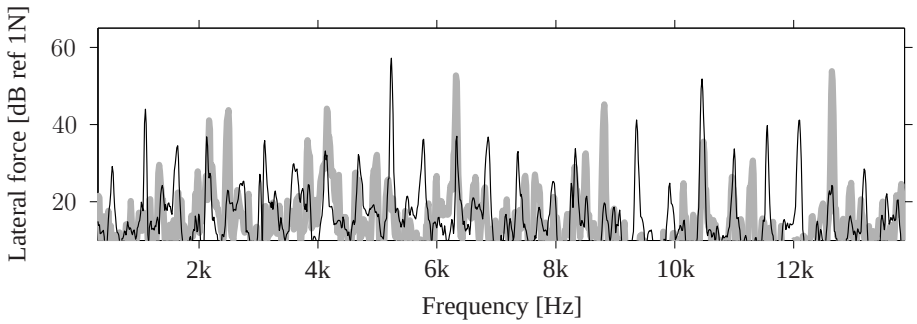

Figure 5.10: Power spectrum of the lateral contact force in the case of falling friction, $\eta = 0.5\%$, $v = 50\,\mathrm{km/h}$: dynamic wheel/rail interaction for the complete wheel receptance (——) in comparison to the case where the (7,0,a) mode has been removed from the wheel receptance (——, *in grey*).

Chapter 6
Conclusions and future work

6.1 Conclusions

In this thesis, a time-domain model for the combined vertical and tangential wheel/rail interaction has been presented, which accounts for the non-linear processes in the contact zone.

An important feature of the model is the representation of wheel and track by Green's functions, which allows inclusion of any linear wheel and track model. A discretely supported rail, for instance, can easily be considered. As the Green's functions are pre-calculated before starting the dynamic simulations, the modelling approach leads to high computational efficiency. Consequently, detailed contact models can be included. Two such contact models have been introduced in this thesis. The first contact model is a 2D model for vertical contact only, which consists of a bedding of independent springs. The second contact model is a 3D model consisting of a vertical and a tangential part. This model is an implementation of Kalker's 'exact' theory [43], which is based on an influence-function method for the elastic half-space. Both vertical contact models take account of non-Hertzian effects. The 2D model uses a simplified wheel and rail geometry and includes one line of wheel/rail roughness in the rolling direction. The 3D model considers the real three-dimensional wheel and rail geometry and takes into account the roughness in several parallel lines. Both vertical contact models include the contact filter effect dynamically and do not require the calculation of an equivalent roughness as pre-processing step. Moreover, discrete irregularities such as wheel flats and rail joints can readily be included by updating the wheel or rail profile in the contact zone in each time step. The tangential contact model – like the vertical contact model – is fully non-linear and transient. To the knowledge of the author, it is the first time that such a model is used online in a model for wheel/rail interaction, at least in the context of noise prediction. The reason why such a model has not been used previously in this context is that the calculation effort was considered too high.

As mentioned above, the wheel/rail interaction model presented in this thesis is computationally efficient due to the chosen approach based on Green's functions.

When only vertical contact is considered in the wheel/rail interaction model, typical calculation times (e.g. for the simulations in *Paper III*) on a standard PC are a few minutes in the case of the 2D contact model and a few tens of minutes in the case of the 3D contact model. When the tangential contact is included, the calculation times increase considerably, but are still manageable. A typical simulation from *Section 5.3* takes a few days on a standard PC.

In the thesis and the appended papers, the wheel/rail interaction model has been applied for different excitation cases. Cases considered are excitation by idealised sinusoidal roughness and by measured roughness of the wheel and rail running surfaces, by different types of wheel flats, and by frictional instability during curve negotiation for both a constant and a velocity-dependent friction coefficient.

In the case of roughness excitation, the vertical interaction model has been validated against existing established interaction models. A Hertzian spring has been used as contact model in this validation. The 3D contact model has been verified separately against Kalker's program CONTACT, and the vertical 2D contact model has previously been verified in [72]. In *Paper I* and *Paper III*, the vertical interaction model has been applied to investigate the contact filter effect for passing over a rail with idealised sinusoidal corrugation and excitation by detailed measured roughness data, respectively. Simulations with the 2D and 3D vertical contact models have been compared with simulations using a non-linear Hertzian spring as contact model applied in combination with an equivalent roughness calculated in a pre-processing step. The contact filter effect was clearly visible for roughness wavelengths that were up to three to four times the nominal contact patch length. As a general tendency, the different models performing roughness filtering on one line – either dynamically (2D model) or quasi-statically (Hertzian spring with pre-calculated equivalent roughness) – gave similar results. An exception is the Hertzian spring with roughness pre-filtering by averaging over the nominal contact patch length, which gave significantly different results at higher frequencies (above 2 kHz for the chosen model parameters) in the case of real measured roughness. The main findings from the investigation of the contact filter effect concern the differences between the 2D and 3D contact models obtained for real measured roughness. The 3D contact model gives, as a general tendency, a contact force level several dB lower than the 2D model. The differences between the 2D and 3D models increase with a decrease in roughness correlation across the width of the contact. A parameter based on the coherence of several parallel roughness lines has been proposed in *Paper III* to assess the correlation across the width of the contact patch. The differences in contact force level obtained with the 2D and 3D models vary also significantly with the roughness line chosen in the 2D model. Using an average of several roughness lines as input in the 2D model instead of only one line cannot generally be expected to result in sufficient accuracy. The simulations indicated, too, that a lateral roughness resolution of at least $4\,\mathrm{mm}$

should be used in the 3D model, which corresponds to measuring the roughness on at least five parallel lines. The primary conclusion from the study of the contact filter effect is thus that the common practice, of measuring only one longitudinal roughness line that is taken as typical of the running band, is generally not sufficient, since significant errors may occur when the 3D roughness distribution is represented by only one roughness line.

In *Paper II*, the interaction model together with the 2D contact model has been applied to calculate impact forces caused by wheel flats. Simulation results have been compared to field measurements in terms of the maximum impact forces during wheel-flat passage. The agreement found between simulations and measurements was fairly good throughout the investigated range of train speeds from $30\,\mathrm{km/h}$ to $100\,\mathrm{km/h}$. The short parameter study presented in *Paper II* showed that train speed, wheel-flat depth and wheel-flat type are important parameters for the magnitude of the impact force. Especially for higher train speeds, the impact position of the wheel on the rail in relation to the sleeper location has a significant influence, too. A minor disadvantage of the 2D contact model in the context of wheel flats (or other wheel irregularities) is that this contact model requires a reduced wheel radius in order to model Hertzian contact for smooth surfaces. Consequently, the wheel flat has to be mapped onto the reduced wheel, implying that it is not possible to represent correctly both wheel-flat depth and length. Using the 3D contact model would make it possible to keep the original wheel radius and to include the complete three-dimensional geometry of the wheel flat.

In *Paper IV* and *Section 5.3.2*, the combined vertical/tangential interaction model has been applied for excitation by frictional instability in the case of a falling friction curve. In the dynamic simulations, stick/slip oscillations developed, which had a main frequency component corresponding to an axial mode of the wheel with zero nodal circles. The 3D contact model in combination with a slip-velocity dependent friction coefficient, however, is not yet considered completely reliable. In the quasi-static case, when wheel and rail dynamics are not included, grid-size dependent high-frequency oscillations were observed. It is to be assumed that the results from the dynamic simulations are equally grid-size dependent. Furthermore, it cannot be excluded that the possible existence of multiple solutions in the contact model has an influence on the outcome of the dynamic simulations. Further research is needed on the handling of the described phenomena in the dynamic algorithm and their implications. The interaction model in combination with a velocity-dependent friction coefficient should however be fully applicable, if a simpler tangential contact model is used.

Excitation by frictional instability in the case of a constant friction coefficient has been investigated in *Paper V*. Simulations have been carried out with the combined vertical/tangential interaction model for a range of input parameters. An important result from the parameter study is that a falling friction curve is not a precondition

for stick/slip oscillations to occur during curve negotiation. Stick/slip is also possible in the case of constant friction – as suggested by previous publications. The imposed lateral creepage, the friction coefficient and the lateral contact position were found to be key parameters for the occurrence of stick/slip – and consequently squeal. In particular, the conditions prevailing at the leading inner wheel of the bogie during curving (i.e. underradial position and contact towards the field side of the tread) were found to promote squeal. In all cases where stick/slip oscillations developed, the main frequency component was close to wheel resonances corresponding to axial modes of the wheel, with zero nodal circles. These results are in good qualitative agreement with previously published findings about curve squeal.

Summing up, the functioning of the developed wheel/rail interaction model has been demonstrated for a variety of excitation cases. The model allows consideration of the three-dimensional roughness distribution throughout the contact patch, the real non-Hertzian wheel/rail geometry, arbitrarily large creepages, frictional excitation, and comprehensive wheel and track models. The simulation results give detailed information about the dynamic processes in the contact zone. The applicability of the interaction model for practical cases depends, however, on the availability and accuracy of input data. Critical are, for instance, the parameters of the track model characterising railpads and ballast and the wheel/rail roughness distribution. Especially difficult to measure are also the actual friction conditions prevailing in wheel/rail contact.

6.2 Future work

The wheel/rail interaction model presented in this thesis has been developed with the long-term goal of providing a model for the prediction of rolling noise, impact noise and squeal noise. To make the model complete, a radiation model will be implemented. The detailed wheel and rail models used in this thesis allow calculating the normal surface velocities of wheel and rail occurring due to the time-history of the dynamic contact forces. These data can be used as input to radiation models, which are readily available in the literature. One possibility is to apply simplified approaches based on the radiation efficiency to calculate the radiated sound power, as e.g. implemented in the model TWINS [97]. An alternative approach is to use more detailed boundary element models; see e.g. [66].

An important aspect of future work is to seek additional validation of the proposed interaction model against field measurements. In *Paper II*, it has been shown that the simulation results from the model agree well with one set of measured impact forces caused by wheel flats. The results for frictional instability from *Paper V* agree qualitatively very well with published results about curve squeal, obtained from simulations and measurements. To gain further confidence that the developed model is quantitatively reliable, a more extensive comparison to field measure-

ments should be carried out. The author is grateful for having access to the results of a field measurement campaign on impact noise caused by wheel flats and rail joints, which was carried out in the context of Virginie Delavaud's thesis work [17] at SNCF / ENSTA ParisTech. On the basis of these data, the vertical wheel/rail interaction model will be further evaluated for excitation by discrete irregularities. Also in the context of curve squeal, experimental validation is needed. In the field, however, it is difficult to gain control over important model parameters such as the wheel/rail contact position and the prevailing friction conditions. The latter are influenced by e.g. humidity, temperature and the track condition. Consequently, it would be preferable to use a test rig, where good control of essential parameters can be achieved.

The problems occurring when combining the tangential contact model with a slip-velocity dependent friction coefficient should be investigated further. It should be considered to extend the quasi-static tangential contact model and include the contact dynamics. This might solve the problem with the grid-size dependent high-frequency oscillations. Additionally, a way must be found to correctly handle the problem of multiple solutions before the algorithm can be used with confidence. An alternative approach is to introduce a simpler tangential contact model, which can easily be combined with a falling friction curve.

Moreover, the wheel/rail interaction model presented in this thesis opens up a lot of possibilities for further investigations. Three examples are given in the following:

- In the literature review about tangential contact models in *Section 2.8*, it has been pointed out that so far only models for steady-state rolling contact had been used in squeal models. The interaction model presented in this thesis with its transient rolling contact model could be used to assess the errors introduced by using simpler contact models, at least in the context of a constant friction coefficient. The results of such an investigation could also be used to derive a computationally efficient engineering model for curve squeal. Although the modelling approach proposed in this thesis is considered numerically efficient, the resulting calculation times of typically a few days when including tangential contact are considered too long in engineering applications. As comparisons can be made with the detailed transient contact model, a simpler tangential contact model could be introduced having control over the simplifications made and keeping the dependence on essential model parameters.

- In the context of curve squeal, the model could be used to carry out a more detailed parameter study in order to enhance the understanding of squeal generation. Beside the lateral creepage, the friction coefficient and the lateral contact position, parameters of interest are for example the train speed, the normal load, and the roughness of the wheel and rail running surfaces. It

would also be worthwhile to investigate the influence of longitudinal creepage on the occurrence of squeal. By this means, Rudd's assumption [81] that longitudinal creepage is not a significant source of curve squeal could be tested.

- The vertical interaction model could be used for a more detailed study on the impact forces caused by wheel flats or other discrete irregularities. In this context, it seems promising to apply the 3D contact model, which makes it possible to include the complete 3D geometry of the discrete irregularity.

The three examples mentioned are just a selection of possible applications of the model, which covers the complete area of high-frequency wheel/rail interaction. Although the model has been developed in the context of noise prediction, it is not limited to this area. It can for example also be applied in connection with the modelling of corrugation growth or other types of wheel and track deterioration, or provide input for models predicting ground vibrations.

Appendix A
Overview of the appended papers

In the appended papers, the wheel/rail interaction model is used with different submodels for wheel, track and contact, which are specified in Table A.1. A detailed description of these submodels is given in *Chapter 3*. The different excitation mechanisms and applications treated in *Paper I* to *Paper V* are listed in Table A.2. Additionally, it is indicated which models have been validated against existing models and field measurements.

Table A.1: Implemented submodels in the wheel/rail interaction models presented in *Papers I-V*.

	Wheel model	Track model	Contact model	Directions
Paper I	1-dof	DIFF [64]	2D Winkler	vertical interaction
Paper II	2-dof	DIFF [64]	2D Winkler	vertical interaction
Paper III	2-dof	DIFF [64]	(1) 3D half-space (2) 2D Winkler (3) Hertz contact	vertical interaction
Paper IV	FE	WFE [66]	3D half-space	vertical/tangential interaction
Paper V	FE	WFE [66]	3D half-space	vertical/tangential interaction

Table A.2: Application areas and validation of the wheel/rail interaction models presented in *Papers I-V*.

	Excitation mechanism	Application	Validation against
Paper I	(1) roughness excitation (2) parametric excitation	contact filter effect	existing interaction model
Paper II	excitation by discrete irregularities	impact forces due to wheel flats	field measurements
Paper III	roughness excitation	contact filter effect	—
Paper IV	frictional instability in the case of falling friction	stick/slip	—
Paper V	frictional instability in the case of constant friction	stick/slip	existing contact model

Appendix B
Influence coefficients for the elastic half-space

The normal contact model described in *Section 3.4.2* and the tangential contact model described in *Section 3.6* are based on influence coefficients for the elastic half-space. These coefficients are given in Kalker's book [43] and are listed here for convenience in the form needed in this work.

The coefficients are valid for the case where the potential contact area between wheel and rail is divided into N_p rectangular elements with side lengths Δx and Δy, see Fig. B.1, and the traction is taken as piecewise constant over the mesh of rectangles. Kalker gave the coefficients for the case where the two contacting bodies are made of different materials. Here it is additionally assumed that the two bodies, i.e. wheel and rail, are made of the same material, which has a modulus of rigidity G and a Poisson's ratio ν.

The influence coefficient A_{IiJj} gives the displacement in i-direction at the centre of element I due to a unit traction in j-direction in element J. The coefficients are obtained as

$$A_{I1J1} = \frac{1}{\pi G}\left[J_3 - \nu J_2\right] \tag{B.1}$$

$$A_{I2J2} = \frac{1}{\pi G}\left[J_3 - \nu J_1\right] \tag{B.2}$$

$$A_{I3J3} = \frac{1-\nu}{\pi G} J_3 \tag{B.3}$$

$$A_{I1J2} = A_{I2J1} = \frac{\nu}{\pi G} J_4\,. \tag{B.4}$$

The remaining coefficients A_{I1J3}, A_{I3J1}, A_{I2J3} and A_{I3J2}, which would be responsible for the coupling between the normal and tangential directions, are zero for identical materials of the two bodies.

The functions J_1 to J_4 depend on the variables a, b, c and d giving the distances in x'- and y'-directions between the centre of element I and the corners of element J

$$\begin{aligned} a &= \Delta x_{IJ} - \tfrac{\Delta x}{2}\,, \quad b = \Delta x_{IJ} + \tfrac{\Delta x}{2}\,, \\ c &= \Delta y_{IJ} - \tfrac{\Delta y}{2}\,, \quad d = \Delta y_{IJ} + \tfrac{\Delta y}{2}\,, \end{aligned} \tag{B.5}$$

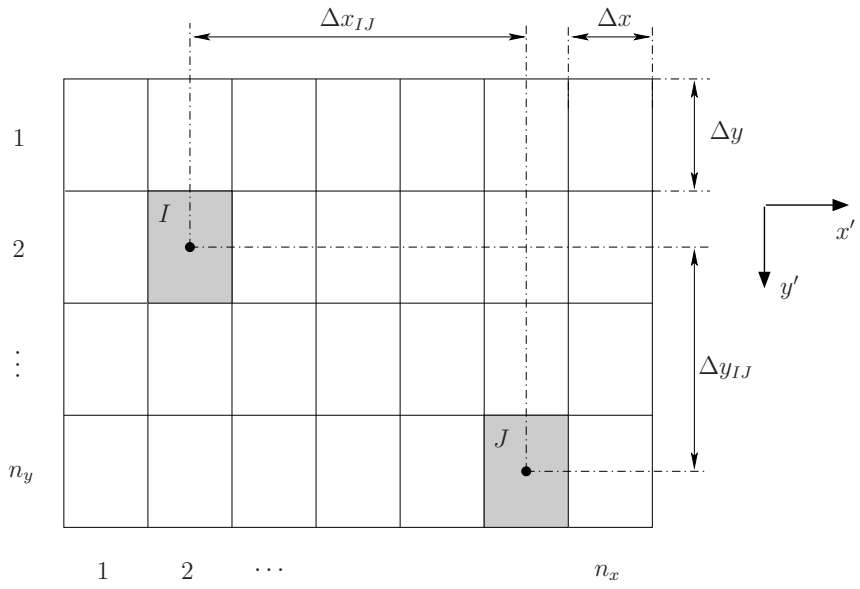

Figure B.1: Potential contact area divided into $N_\mathrm{p} = n_x n_y$ rectangular elements with side lengths Δx and Δy.

where

$$\begin{aligned} \Delta x_{IJ} &= x'_J - x'_I \\ \Delta y_{IJ} &= y'_J - y'_I \,, \end{aligned} \tag{B.6}$$

and (x'_I, y'_I) and (x'_J, y'_J) are the locations of the centres of elements I and J, respectively.

The functions J_1 to J_4 are given by

$$J_1(a,b,c,d) = g(d,b) - g(d,a) - g(c,b) + g(c,a) \tag{B.7}$$
$$J_2(a,b,c,d) = g(b,d) - g(a,d) - g(b,c) + g(a,c) \tag{B.8}$$
$$J_3(a,b,c,d) = J_1(a,b,c,d) + J_2(a,b,c,d) \tag{B.9}$$
$$J_4(a,b,c,d) = -h(b,d) + h(a,d) + h(b,c) - h(a,c)\,, \tag{B.10}$$

where the functions g and h are defined as

$$g(x,y) = x \,\ln\left(y + h(x,y)\right) \tag{B.11}$$
$$h(x,y) = \sqrt{x^2 + y^2}\,, \tag{B.12}$$

and $\ln$ denotes the natural logarithm.

Bibliography

[1] A. Alonso and J.G. Giménez. Non-steady state modelling of wheel-rail contact problem for the dynamic simulation of railway vehicles. *Vehicle System Dynamics*, 46(3):179–196, 2008.

[2] A. Alonso and J.G. Giménez. Wheel-rail contact: Roughness, heat generation and conforming contact influence. *Tribology International*, 41:755–768, 2008.

[3] J.-B. Ayasse and H. Chollet. Determination of the wheel rail contact patch in semi-Hertzian conditions. *Vehicle System Dynamics*, 43(3):161–172, 2005.

[4] J.-B. Ayasse and H. Chollet. Wheel-rail contact. In S. Iwnicki, editor, *Handbook of Railway Vehicle Dynamics*, chapter 4. CRC Press, Taylor and Francis Group, Boca Raton, FL, 2006.

[5] L. Baeza, A. Roda, J. Carballeira, and E. Giner. Railway train-track dynamics for wheelflats with improved contact models. *Nonlinear Dynamics*, 45:385–397, 2006.

[6] Y. Ben Othman. *Kurvenquietschen: Untersuchung des Quietschvorgangs und Wege der Minderung*. PhD thesis, Fakultät für Verkehrs- und Maschinensysteme, Technische Universität Berlin, 2009.

[7] J. Boussinesq. *Application des Potentiels à l'Étude de l'Équilibre et du Mouvement des Solides Élastiques.* Gauthier-Villars, Paris, 1885.

[8] J.F. Brunel, P. Dufrénoy, M. Naït, J.L. Muñoz, and F. Demilly. Transient model for curve squeal noise. *Journal of Sound and Vibration*, 293:758–765, 2006.

[9] F. Bucher, K. Knothe, and A. Theiler. Normal and tangential contact problem of surfaces with measured roughness. *Wear*, 253:204–218, 2002.

[10] F.W. Carter. On the action of a locomotive driving wheel. *Proceedings of the Royal Society of London, Series A*, 112(760):151–157, 1926.

[11] V. Cerruti. *Mem. fis. mat.* Accademia dei Lincei, Roma, 1882.

[12] O. Chiello, J.-B. Ayasse, N. Vincent, and J.-R. Koch. Curve squeal of urban rolling stock - Part 3: Theoretical model. *Journal of Sound and Vibration*, 293:710–727, 2006.

[13] B.E. Croft. *The Development of Rail-head Acoustic Roughness*. PhD Thesis, Institute of Sound and Vibration Research, University of Southampton, 2009.

[14] B.E. Croft, E.A.H. Vollebregt, and D.J. Thompson. An investigation of velocity-dependent friction in wheel-rail rolling contact. In *Proceedings of the 10th International Workshop on Railway Noise (IWRN10)*, pages 35–42, Nagahama, Japan, 2010.

[15] S. Damme, U. Nackenhorst, A. Wetzel, and B.W. Zastrau. On the numerical analysis of the wheel-rail system in rolling contact. In K. Popp and W. Schiehlen, editors, *System Dynamics and Long-Term Behaviour of Railway Vehicle, Track and Subgrade*, volume 6 of *Lecture Notes in Applied Mechanics*. Springer-Verlag, Berlin Heidelberg, 2003.

[16] F.G. de Beer, M.H.A. Janssens, and P.P. Kooijman. Squeal noise of rail-bound vehicles influenced by lateral contact position. *Journal of Sound and Vibration*, 267:497–507, 2003.

[17] V. Delavaud. *Modélisation Temporelle de l'Interaction Roue/Rail, pour une Application au Bruit de Roulement Ferroviaire*. PhD Thesis, ENSTA ParisTech, Paris, France, 2011.

[18] DEsolver. *GENSYS users manual*, 2009.

[19] M.G. Dittrich and X. Zhang. The Harmonoise/IMAGINE model for traction noise of powered railway vehicles. *Journal of Sound and Vibration*, 293:986–994, 2006.

[20] J.A. Elkins. Prediction of wheel/rail interaction: The state-of-the-art. *Vehicle System Dynamics*, 20(Issue S1):1–27, 1992.

[21] J.M. Fields and J.G. Walker. Comparing the relationships between noise level and annoyance in different surveys: A railway noise vs. aircraft and road traffic comparison. *Journal of Sound and Vibration*, 81(1):51–80, 1982.

[22] U. Fingberg. A model for wheel-rail squealing noise. *Journal of Sound and Vibration*, 143:365–377, 1990.

[23] R.A.J. Ford and D.J. Thompson. Simplified contact filters in wheel/rail noise prediction. *Journal of Sound and Vibration*, 293:807–818, 2006.

[24] P.-E. Gautier, C. Talotte, and P. Fodiman. La recherche à la SNCF pour la réduction du bruit des trains. *Revue générale des chemins de fer*, 6:9–19, 1999.

[25] Ch. Glocker, E. Cataldi-Spinola, and R.I. Leine. Curve squealing of trains: Measurement, modelling and simulation. *Journal of Sound and Vibration*, 324:365–386, 2009.

[26] S.L. Grassie, R.W. Gregory, D. Harrison, and K.L. Johnson. The dynamic response of railway track to high frequency vertical excitation. *Journal of Mechanical Engineering Science*, 24(2):77–90, 1982.

[27] J.A. Greenwood and J.H. Tripp. The elastic contact of rough spheres. *ASME Journal of Applied Mechanics*, 34:153–159, 1967.

[28] J.A. Greenwood and J.B.P. Williamson. Contact of nominally flat surfaces. *Proceedings of the Royal Society of London. Series A, Mathematical and Physical Sciences*, 295(1442):300–319, 1966.

[29] A. Groß-Thebing. Frequency-dependent creep coefficients for three-dimensional rolling contact problems. *Vehicle System Dynamics*, 18:359–374, 1989.

[30] L. Gry. Dynamic modelling of railway track based on wave propagation. *Journal of Sound and Vibration*, 195(3):477–505, 1996.

[31] M. Heckl. Proposal for a railway simulation program. In *A Workshop on Rolling Noise Generation*, pages 128–148. Institut für Technische Akustik, Technische Universität Berlin, October 1989.

[32] M.A. Heckl. Curve squeal of train wheels, Part 2: Which wheel modes are prone to squeal? *Journal of Sound and Vibration*, 229(3):695–707, 2000.

[33] M.A. Heckl and I.D. Abrahams. Curve squeal of train wheels, Part 1: Mathematical model for its generation. *Journal of Sound and Vibration*, 229(3):669–693, 2000.

[34] K. Hempelmann, F. Hiss, K. Knothe, and B. Ripke. The formation of wear patterns on rail tread. *Wear*, 144(1-2):179–195, 1991.

[35] H. Hertz. Ueber die Berührung fester elastischer Körper. *Journal für reine und angewandte Mathematik*, 92:156–171, 1882.

[36] N. Hoffmann, M. Fischer, R. Allgaier, and L. Gaul. A minimal model for studying properties of the mode-coupling type instability in friction induced oscillations. *Mechanics Research Communications*, 29:197–205, 2002.

[37] Z.Y. Huang, D.J. Thompson, and C.J.C. Jones. Squeal prediction for a bogied vehicle in a curve. In *Proceedings of the Ninth International Workshop on Railway Noise (9thIWRN)*, Munich, September 2007.

[38] J. Jergéus. *Railway Wheel Flats - Martensite Formation, Residual Stresses, and Crack Propagation*. PhD Thesis, Division of Solid Mechanics, Chalmers University of Technology, Göteborg, Sweden, 1998.

[39] J. Jiang, R. Dwight, and D. Anderson. Field verification of curving noise mechanism. In *Proceedings of the 10th International Workshop on Railway Noise (IWRN10)*, pages 349–360, Nagahama, Japan, 2010.

[40] A. Johansson and J.C.O. Nielsen. Out-of-round railway wheels - wheel-rail contact forces and track response derived from field tests and numerical simulations. *Proc IMechE, Part F: Journal of Rail and Rapid Transport*, 217:135–146, 2003.

[41] K.L. Johnson. *Contact Mechanics*. Cambridge University Press, 1987.

[42] J.J. Kalker. A fast algorithm for the simplified theory of rolling contact. *Vehicle System Dynamics*, 11:1–13, 1982.

[43] J.J. Kalker. *Three-Dimensional Elastic Bodies in Rolling Contact*. Kluwer Academic Publishers, Dordrecht, Boston, London, 1990.

[44] J.J. Kalker. Wheel-rail rolling contact theory. *Wear*, 144:243–261, 1991.

[45] C.T. Kelley. *Solving nonlinear equations with Newton's method (Fundamentals of algorithms)*. SIAM, Philadelphia, USA, 2003.

[46] K. Knothe and A. Groß-Thebing. Derivation of frequency dependent creep coefficients based on an elastic half-space model. *Vehicle System Dynamics*, 15:133–153, 1986.

[47] K. Knothe and A. Groß-Thebing. Short wavelength rail corrugation and non-steady-state contact mechanics. *Vehicle System Dynamics*, 46(1-2):49–66, 2008.

[48] K. Knothe and S. Stichel. *Schienenfahrzeugdynamik*. Springer-Verlag, Berlin Heidelberg, 2003.

[49] K. Knothe, R. Wille, and W. Zastrau. Advanced contact mechanics - road and rail. *Vehicle System Dynamics*, 35(4-5):361–407, 2001.

[50] KL. Knothe and S.L. Grassie. Modelling of railway track and vehicle/track interaction at high frequencies. *Vehicle System Dynamics*, 22:209–262, 1993.

[51] J.R. Koch, N. Vincent, H. Chollet, and O. Chiello. Curve squeal of urban rolling stock - Part 2: Parametric study on a 1/4 scale test rig. *Journal of Sound and Vibration*, 293:701–709, 2006.

[52] K. Kraft. Der Einfluß der Fahrgeschwindigkeit auf den Haftwert zwischen Rad und Schiene. *Archiv für Eisenbahntechnik*, 22:58–78, 1967.

[53] H. Le-The. *Normal- und Tangentialspannungsberechnung beim rollenden Kontakt für Rotationskörper mit nichtelliptischen Kontaktflächen*. Fortschrittberichte VDI, Reihe 12: Verkehrstechnik/Fahrzeugtechnik, Nr.87. VDI-Verlag GmbH, Düsseldorf, 1987.

[54] Ch. Linder. *Verschleiss von Eisenbahnrädern mit Unrundheiten.* PhD thesis, Dissertation ETH, Nr.12342, 1997.

[55] G. Lundberg and H. Sjövall. *Stress and Deformation in Elastic Contacts*. Publikation nr 4, The Institution of Theory of Elasticity and Strength of Materials, Chalmers University of Technology, Gothenburg, Sweden, 1958.

[56] K. Magnus and K. Popp. *Schwingungen*. B. G. Teubner, Stuttgart, Germany, 5th edition edition, 1997.

[57] T. Mazilu. Green's functions for analysis of dynamic response of wheel/rail to vertical excitation. *Journal of Sound and Vibration*, 306:31–58, 2007.

[58] U. Moehler. Community response to railway noise: A review of social surveys. *Journal of Sound and Vibration*, 120(2):321–332, 1988.

[59] L. Nayak and K.L. Johnson. Pressure between elastic bodies having a slender area of contact and arbitrary profiles. *International Journal of Mechanical Sciences*, 21(4):237–247, 1979.

[60] S.G. Newton and R.A. Clark. An investigation into the dynamic effects on the track of wheelflats on railway vehicles. *Journal of Mechanical Engineering Science*, 21(4):287–297, 1979.

[61] J.C.O. Nielsen. Dynamic interaction between wheel and track - a parametric search towards an optimal design of rail structures. *Vehicle System Dynamics*, 23(2):115 – 132, 1994.

[62] J.C.O Nielsen. High-frequency vertical wheel-rail contact forces - validation of a prediction model by field testing. In *Proceedings of the 7th International Conference on Contact Mechanics and Wear of Rail/Wheel Systems*, Brisbane, Australia, September 2006.

[63] J.C.O. Nielsen. High-frequency vertical wheel-rail contact forces - validation of a prediction model by field testing. *Wear*, 265:1465–1471, 2008.

[64] J.C.O Nielsen and A. Igeland. Vertical dynamic interaction between train and track - influence of wheel and track imperfections. *Journal of Sound and Vibration*, 187(5):825–839, 1995.

[65] J.C.O. Nielsen, J.W. Ringsberg, and L. Baeza. Influence of railway wheel flat impact on crack growth in rails. In *Proceedings of the 8th International Heavy Haul Conference*, pages 789–797, Rio de Janeiro, Brazil, 14-16 June 2005.

[66] C.-M. Nilsson, C.J.C. Jones, D.J. Thompson, and J. Ryue. A waveguide finite element and boundary element approach to calculating the sound radiated by railway and tram rails. *Journal of Sound and Vibration*, 321:813–836, 2009.

[67] A. Nordborg. Wheel/rail noise generation due to nonlinear effects and parametric excitation. *Journal of the Acoustical Society of America*, 111(4):1772–1781, April 2002.

[68] J.T. Oden and J.A.C. Martins. Models and computational methods for dynamic friction phenomena. *Computer Methods in Applied Mechanics and Engineering*, 52:527–634, 1985.

[69] J.P. Pascal and G. Sauvage. The available methods to calculate the wheel/rail forces in non Hertzian contact patches and rail damaging. *Vehicle System Dynamics*, 22:263–275, 1993.

[70] B. Paul and J. Hashemi. Contact pressures on closely conforming elastic bodies. *Journal of Applied Mechanics*, 48(3):543–548, 1981.

[71] F. J. Périard. *Wheel-Rail Noise Generation: Curve Squealing by Trams*. PhD thesis, Technische Universiteit Delft, 1998.

[72] A. Pieringer. *Modelling of Wheel/Rail Interaction Considering Roughness and Discrete Irregularities*. Licentiate thesis, Chalmers University of Technology, Applied Acoustics, Gothenburg, Sweden, December 2008.

[73] J. Piotrowski and H. Chollet. Wheel-rail contact models for vehicle system dynamics including multi-point contact. *Vehicle System Dynamics*, 43(6-7):455–483, 2005.

[74] J. Piotrowski and W. Kik. A simplified model of wheel/rail contact mechanics for non-Hertzian problems and its application in rail vehicle dynamics. *Vehicle System Dynamics*, 46(1-2):27–48, 2008.

[75] P. Remington and J. Webb. Estimation of wheel/rail interaction forces in the contact area due to roughness. *Journal of Sound and Vibration*, 193(1):83–102, 1996.

[76] P.J. Remington. Wheel/rail noise - Part I: Characterization of the wheel/rail dynamic system. *Journal of Sound and Vibration*, 46(3):359–379, 1976.

[77] P.J. Remington. Wheel/rail noise - Part IV: Rolling noise. *Journal of Sound and Vibration*, 46(3):419–436, 1976.

[78] P.J. Remington. Wheel/rail rolling noise, I: Theoretical analysis. *Journal of the Acoustical Society of America*, 81(6):1824–1832, 1987.

[79] P.J. Remington. Wheel/rail rolling noise, II: Validation of the theory. *Journal of the Acoustical Society of America*, 81(6):1824–1832, 1987.

[80] H. Reusner. *Druckflächenbelastung und Oberflächenverschiebung im Wälzkontakt von Rotationskörpern*. PhD Thesis. TU Karlsruhe, 1977.

[81] M.J. Rudd. Wheel/rail noise - Part II: Wheel squeal. *Journal of Sound and Vibration*, 46(3):381–394, 1976.

[82] W. Scholl. Schwingungsuntersuchungen an Eisenbahnschienen. *Acustica*, 52(1):10–15, 1982.

[83] Z.Y. Shen, J.K. Hedrick, and J.A. Elkins. A comparison of alternative creep force models for rail vehicle dynamic analysis. In *Proceedings of the 8th IAVSD Symposium*, pages 591–605, Cambridge, MA, 1983. Swets and Zeitlinger, Lisse.

[84] A. Sladkowski and M. Sitarz. Analysis of wheel/rail interaction using FE software. *Wear*, 258:1217–1223, 2005.

[85] H. Stappenbeck. Das Kurvengeräusch der Straßenbahn - Möglichkeiten zu seiner Unterdrückung. *VDI Zeitschrift*, 96(6):171–175, 1954.

[86] E. Tassilly and N. Vincent. A linear model for the corrugation of rails. *Journal of Sound and Vibration*, 150(1):25–45, 1991.

[87] T. Telliskivi and U. Olofsson. Contact mechanics analysis of measured wheel-rail profiles using the finite element method. *Proc IMechE, Part F: Journal of Rail and Rapid Transport*, 215:65–72, 2001.

[88] D. Thompson. *Railway Noise and Vibration: Mechanisms, Modelling and Means of Control*. Elsevier, Oxford, UK, 2009.

[89] D.J. Thompson. Wheel-rail noise generation, Part I: Introduction and interaction model. *Journal of Sound and Vibration*, 161(3):387–400, 1993.

[90] D.J. Thompson. Wheel-rail noise generation, Part II: Wheel vibration. *Journal of Sound and Vibration*, 161(3):401–419, 1993.

[91] D.J. Thompson. Wheel-rail noise generation, Part III: Rail vibration. *Journal of Sound and Vibration*, 161(3):421–446, 1993.

[92] D.J. Thompson. Wheel-rail noise generation, Part IV: Contact zone and results. *Journal of Sound and Vibration*, 161(3):447–466, 1993.

[93] D.J. Thompson. Wheel-rail noise generation, Part V: Inclusion of wheel rotation. *Journal of Sound and Vibration*, 161(3):467–482, 1993.

[94] D.J. Thompson. On the relationship between wheel and rail surface roughness and rolling noise. *Journal of Sound and Vibration*, 193(1):149–160, 1996.

[95] D.J. Thompson. The influence of the contact zone on the excitation of wheel/rail noise. *Journal of Sound and Vibration*, 267:523–535, 2003.

[96] D.J. Thompson and P.-E. Gautier. Review of research into wheel/rail rolling noise reduction. *Proc IMechE, Part F: Journal of Rail and Rapid Transport*, 220(4):385–408, 2006.

[97] D.J. Thompson, B. Hemsworth, and N. Vincent. Experimental validation of the TWINS prediction program for rolling noise, Part 1: Description of the model and method. *Journal of Sound and Vibration*, 193(1):123–135, 1996.

[98] D.J. Thompson and C.J.C. Jones. A review of the modelling of wheel/rail noise generation. *Journal of Sound and Vibration*, 231(3):519–536, 2000.

[99] D.J. Thompson and P.J. Remington. The effects of transverse profile on the excitation of wheel/rail noise. *Journal of Sound and Vibration*, 231(3):537–548, 2000.

[100] D.J. Thompson and N. Vincent. Track dynamic behaviour at high frequencies. Part 1: Theoretical models and laboratory measurements. *Vehicle System Dynamics*, Supplement 24:86–99, 1995.

[101] P.T. Torstensson and J.C.O. Nielsen. Monitoring of rail corrugation growth due to irregular wear on a railway metro curve. *Wear*, 267(556-561), 2009.

[102] P.J. Vermeulen and K.L. Johnson. Contact of nonspherical elastic bodies transmitting tangential forces. *Trans. ASME, Series E, Journal of Applied Mechanics*, 31:338–340, 1964.

[103] N. Vincent and D.J. Thompson. Track dynamic behaviour at high frequencies. Part 2: Experimental results and comparisons with theory. *Vehicle System Dynamics*, Supplement 24:100–114, 1995.

[104] E.A.H. Vollebregt. A Gauss-Seidel type solver for special convex programs, with application to frictional contact mechanics. *Journal for Optimization Theory and Applications*, 87(1):47–67, 1995.

[105] E.A.H. Vollebregt. *User's Guide for CONTACT, J.J. Kalker's variational contact model*. Technical Report, TR09_03, version 0.9, VORtech Computing, Delft, The Netherlands, 2009.

[106] E.A.H. Vollebregt, J.J. Kalker, and H.X. Lin. A fast solver for normal and tangential contact mechanics in the half-space. *Transactions on Engineering Sciences*, 1:235–242, 1993.

[107] H. Wu and J.M. Wang. Non-Hertzian conformal contact at wheel/rail interface. In *Proceedings of the 1995 IEEE/ASME Joint Railroad Conference, April 4-6, 1995, Baltimore, Maryland*, pages 137–144. Institute of Electrical and Electronics Engineering, 1995.

[108] T.X. Wu and D.J. Thompson. Theoretical investigation of wheel/rail nonlinear interaction due to roughness excitation. *Vehicle System Dynamics*, 34:261–282, 2000.

[109] T.X. Wu and D.J. Thompson. A hybrid model for the noise generation due to railway wheel flats. *Journal of Sound and Vibration*, 251(1):115–139, 2002.

[110] T.X. Wu and D.J. Thompson. On the impact noise generation due to a wheel passing over rail joints. *Journal of Sound and Vibration*, 267:485–496, 2003.

[111] G. Xie, P.D. Allen, S.D. Iwnicki, A. Alonso, D.J. Thompson, C.J.C. Jones, and Z.Y. Huang. Introduction of falling friction coefficients into curving calculations for studying curve squeal noise. *Vehicle System Dynamics*, 44, Supplement:261–271, 2006.

[112] W. Yan and D. Fischer. Applicability of the Hertz contact theory to rail-wheel contact problems. *Archive of Applied Mechanics*, 255-268(70):255–268, 2000.